Non-Equilibrium Evaporation and Condensation

Modeled with Irreversible Thermodynamics, Kinetic Theory, and Statistical Rate Theory

by

Maurice Bond
B.Eng., University of Victoria (2000)

A Thesis Submitted in Partial Fulfillment of the
Requirements for the Degree of

MASTER OF APPLIED SCIENCE

in the Department of Mechanical Engineering

We accept this thesis as conforming
to the required standard

Dr. H. Struchtrup, Supervisor (Department of Mechanical Engineering)

Dr. S. Dost, Department Member (Department of Mechanical Engineering)

Dr. A. Rowe, Department Member (Department of Mechanical Engineering)

Dr. D. Harrington, External Examiner (Department of Chemistry)

Supervisor: Dr. H. Struchtrup

Abstract

The purpose of this work is to demonstrate the usability of irreversible thermodynamics and kinetic theory in describing slow steady state evaporation and condensation, analyze the statistical rate theory (SRT) approach, and investigate the physical phenomena involved.

Recently large interface temperature jumps have been observed during steady state evaporation and condensation experiments; the vapor interface temperature was greater than the liquid interface temperature for condensation and evaporation. To predict the temperature jump, the SRT mass flux was introduced as an alternative to the established approaches of irreversible thermodynamics and kinetic theory of gases.

Simple one dimensional planar and spherical models were developed for slow evaporation and condensation based on the experiments. We considered pure liquid water evaporation and condensation to, and from its own vapor. Expressions for the mass and energy fluxes across the interface were found using irreversible thermodynamics, kinetic theory, and SRT. The SRT theory does not have an energy flux expression, as a substitute we use the irreversible thermodynamics energy flux in the SRT model. The equations were then solved to yield the mass and energy fluxes, and the liquid and vapor temperature profiles.

We find the interface temperature jump is dependant on the energy flux expression. The irreversible thermodynamics energy flux closely predicts the measured temperature jump and direction. Kinetic theory models do not predict the jump, however with incorporation of a velocity dependant condensation coefficient, kinetic theory can predict the correct temperature jump direction, and vapor interface temperature. All the models predict mass fluxes that agree with the measured data.

We suggest the temperature jump direction is established based on the direction of the vapor conductive energy flux, and not the direction of the mass flux (condensation or evaporation).

We conclude that irreversible thermodynamics, kinetic theory, and SRT can all be used to model steady state evaporation and condensation.

Examiners:

Dr. H. Struchtrup, Supervisor (Department of Mechanical Engineering)

Dr. S. Dost, Department Member (Department of Mechanical Engineering)

Dr. A. Rowe, Department Member (Department of Mechanical Engineering)

Dr. D. Harrington, External Examiner (Department of Chemistry)

Table of Contents

List of Tables

List of Figures

Nomenclature

$\underline{c}$, c_k	Molecular velocity vector	$\frac{\mathrm{m}}{\mathrm{s}}$
$\underline{C}$, C_k	Peculiar velocity, $c_i - v_i$	$\frac{\mathrm{m}}{\mathrm{s}}$
c_l	Liquid specific heat	$\frac{\mathrm{J}}{\mathrm{kg\,K}}$
c_p	Vapor constant pressure specific heat	$\frac{\mathrm{J}}{\mathrm{kg\,K}}$
f	Velocity distribution function	$\frac{\mathrm{s}^3}{\mathrm{m}^3\,\mathrm{m}^3}$
f_{ce}	Chapman-Enskog distribution	$\frac{\mathrm{s}^3}{\mathrm{m}^3\,\mathrm{m}^3}$
f_{ce-v}	Chapman-Enskog distribution, with net vapor velocity	$\frac{\mathrm{s}^3}{\mathrm{m}^3\,\mathrm{m}^3}$
f_l	Evaporating molecule distribution	$\frac{\mathrm{s}^3}{\mathrm{m}^3\,\mathrm{m}^3}$
f_m	Maxwellian velocity distribution	$\frac{\mathrm{s}^3}{\mathrm{m}^3\,\mathrm{m}^3}$
f_{m-v}	Maxwellian distribution with net vapor velocity	$\frac{\mathrm{s}^3}{\mathrm{m}^3\,\mathrm{m}^3}$
f_v	Bulk vapor distribution	$\frac{\mathrm{s}^3}{\mathrm{m}^3\,\mathrm{m}^3}$
g	Gibbs free energy	$\frac{\mathrm{J}}{\mathrm{kg}}$
h	Enthalpy	$\frac{\mathrm{J}}{\mathrm{kg}}$
Δh	Enthalpy of vaporization	$\frac{\mathrm{J}}{\mathrm{kg}}$
j	Mass flux	$\frac{\mathrm{kg}}{\mathrm{m}^2\,\mathrm{s}}$
j_i	Radial mass flux at interface	$\frac{\mathrm{kg}}{\mathrm{m}^2\,\mathrm{s}}$
$j\,(r)$	Radial mass flux	$\frac{\mathrm{kg}}{\mathrm{m}^2\,\mathrm{s}}$
k	Boltzmann constant	$\frac{\mathrm{J}}{\mathrm{K}}$
k_s	Statistical Rate Theory Coefficient	$\frac{1}{\mathrm{m}^2\,\mathrm{s}}$ or $\frac{\mathrm{kg}}{\mathrm{m}^2\,\mathrm{s}}$
L_l, L_v	Liquid and vapor depths	m
m	Molecular mass	kg
M	Momentum flux	Pa
p_{evap}	Pressure of evaporating molecules	Pa
p^*	Pressure of reflected vapor molecules	Pa
p_l, p_v	Liquid and vapor pressures	Pa
$p_{sat}\,(T)$	Saturation pressure of temperature T	Pa

Q	Energy flux	$\frac{\mathrm{W}}{\mathrm{m}^2}$
Q_i	Radial energy flux at interface	$\frac{\mathrm{W}}{\mathrm{m}^2}$
$Q\left(r\right)$	Radial energy flux	$\frac{\mathrm{W}}{\mathrm{m}^2}$
q_l, q_v	Liquid and vapor conductive energy fluxes	$\frac{\mathrm{W}}{\mathrm{m}^2}$
R	Water vapor ideal gas constant	$\frac{\mathrm{J}}{\mathrm{kg\,K}}$
R_o, r_c	Radius of curvature	m
$\underline{\mathrm{r}}= \{x, y, z\}$	Position vector	m
r_f	Kinetic theory energy reference correction	$\frac{\mathrm{W}}{\mathrm{m}^2}$
r_i	Interface radius	m
r_l	Liquid boundary radius	m
r_v	Vapor boundary radius	m
s	Entropy	$\frac{\mathrm{J}}{\mathrm{kg\,K}}$
T_{bl}, T_{bv}	Liquid and vapor boundary temperatures	K
$T_l(z)$, $T_v\left(z\right)$	Liquid and vapor temperatures	K
$T_{sat}\left(p\right)$	Saturation temperature of pressure p	K
u	Internal energy	$\frac{\mathrm{J}}{\mathrm{kg}}$
$\underline{\mathrm{v}}$, v_k	Mean vapor velocity	$\frac{\mathrm{m}}{\mathrm{s}}$
z	Vertical position	m

Greek

α	Energy flux phenomenological coefficient	$\frac{\mathrm{W\,K}}{\mathrm{m^2}}$
β	Mass flux phenomenological coefficient	$\frac{\mathrm{kg}}{\mathrm{m^2\,s}}\frac{\mathrm{kg\,K}}{\mathrm{J}}$
γ	Accommodation coefficient	-
$\eta\left(T_l, T\right)$	Kinetic theory mass flux coefficient	-
θ_c, θ_e	Condensation and evaporation coefficients	-
κ_l, κ_v	Liquid and vapor thermal conductivities	$\frac{\mathrm{W}}{\mathrm{m\,K}}$
μ_l, μ_v	Liquid and vapor chemical potentials	$\frac{\mathrm{J}}{\mathrm{kg}}$
ρ_l, ρ_v	Liquid and vapor densities	$\frac{\mathrm{kg}}{\mathrm{m^3}}$
σ	Interface entropy production	$\frac{\mathrm{W}}{\mathrm{m^2\,K}}$
υ_l, υ_v	Liquid and vapor specific volumes	$\frac{\mathrm{m^3}}{\mathrm{kg}}$
$\varphi\left(T_l, T\right)$	Kinetic theory specular and diffuse reflection energy flux coefficient	-
$\varphi_d\left(T_l, T\right)$	Kinetic theory diffuse reflection energy flux coefficient	-
$\varphi_s\left(T_l, T\right)$	Kinetic theory specular reflection energy flux coefficient	-
ψ	Velocity dependant condensation coefficient parameter	-
ω	Velocity dependant condensation coefficient parameter	-

Subscripts and Superscripts

$bulk$	Bulk vapor
e	Equilibrium condition
int	Interface
l	Liquid property
o	Reference Condition
ref	Describes reflected molecules
v	Vapor property
z	Vertical direction

Acronyms

CE	Chapman-Enskog
CEVEL	Chapman-Enskog model with velocity dependant condensation coefficient
DSMC	Direct simulation Monte Carlo
Kn	Knudsen number
HK	Hertz-Knudsen
HKVEL	Hertz-Knudsen model with velocity dependant condensation coefficient
IT	Irreversible thermodynamics
MD	Molecular dynamics
SRT	Statistical rate theory

Chapter 1

Introduction

Evaporation and condensation phenomena have been a subject of research and debate for over one hundred years. The mechanism of transfer across a phase boundary was not a great focus of research because it was considered adequate to assume that the liquid vapor interface is nearly at complete equilibrium. This led to assumptions such as constant temperature across the interface, even outside of equilibrium. Schrage [1] provides a good overview of the history. Ward, Fang, and Stanga's [2], [3], [4] recent steady state evaporation and condensation experiments show large temperature jumps across the interface, something not previously observed.

Interface conditions have been modelled using the kinetic theory of gases, and irreversible thermodynamics to develop expressions for the energy, and mass fluxes across the interface. Ward and Stanga [5] introduced an alternative approach, statistical rate theory (SRT), which they suggest accurately models their observed interface temperature jump. Still other approaches such as the non-equilibrium van der Waals square gradient model, and mesoscopic non-equilibrium thermodynamics have been employed. Modeling has also been done with computationally expensive molecular dynamics (MD) simulations. Most research has focussed on theoretical aspects of evaporation and condensation; little focus has been directed to using these theories to reproduce or predict measured results.

1.1 Purpose and Scope

The purpose of this work is to demonstrate the usability of irreversible thermodynamics and kinetic theory in describing the steady state evaporation and condensation of pure fluids, to analyze the statistical rate theory approach, and to investigate the physical phenomena involved in phase change.

One-dimensional models are developed based on the Ward, Fang, and Stanga [2], [3], [4] experiments. In particular we consider pure liquid water evaporation and condensation to, and from its own vapor. Outside of equilibrium, the temperature is not assumed to be continuous across the interface. Liquid and vapor boundary temperatures, and vapor pressure are prescribed. The balances of mass, and energy are solved for the liquid and vapor temperature profiles. The complete solution requires expressions for mass and energy flux across the interface, which are developed from kinetic theory, irreversible thermodynamics, and SRT. The analysis is performed for relatively slow evaporation and condensation, that is we assume the system is close to equilibrium, which facilitates the use of certain equilibrium expressions, even though the system is outside equilibrium. The equations are solved to yield the mass and energy fluxes per unit area, and the liquid and vapor temperature profiles.

The results due to irreversible thermodynamics, kinetic theory, and SRT are presented and compared. Model result variation with prescribed parameters is investigated, and additional factors that may affect the results are considered. Moreover, model predictions are compared with the Ward and Stanga [4] measured data .

We find good agreement between irreversible thermodynamics, SRT, kinetic theory, and the experimental results [4]. The models are able to predict the measured interface temperature jump magnitude and direction. Our observations indicate that much of the heat transfer involved in the phase change process is conducted through the liquid, but that the temperature jump is directly related to the conductive heat flux through the vapor.

1.2 Ward Group's Experiments

Our model simulations are one-dimensional approximations of the experiments by Ward, Fang, and Stanga [2], [3], [4], who investigated steady state evaporation and condensation of water, octane, and methylcyclohexane.

1.2.1 Apparatus and Procedure

Ward, Fang, and Stanga [2], [3], [4] considered liquid evaporating from, or condensing to, its own vapor. Figure 1.1 shows their apparatus [4].

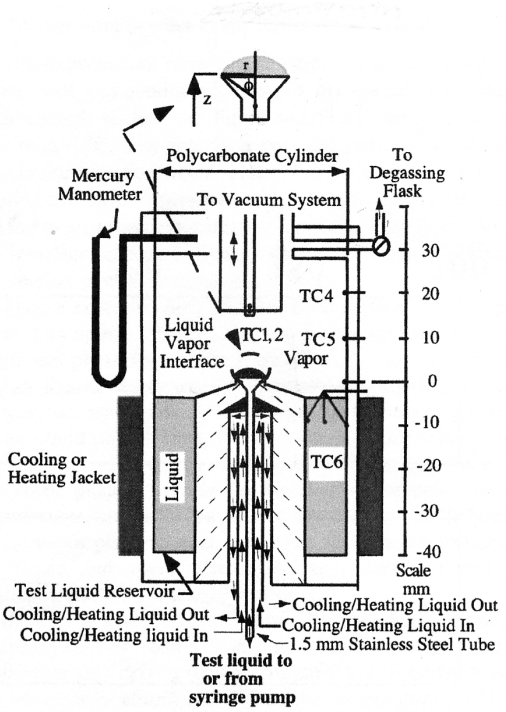

Figure 1.1: Ward et al. steady state evaporation condensation apparatus

Water was supplied through the bottom of the funnel by a syringe pump, and withdrawn as vapor from the top of the chamber. Steady state evaporation was achieved by adjusting the rate of liquid water entry at the inlet, and regulating the vapor pressure by opening and closing a vacuum valve in line with a vacuum pump.

For condensation, the syringe pump withdrew water at a constant rate, and the water exiting the funnel was cooled by a cooling jacket causing the water vapor in the chamber to condense. Steady state was maintained by allowing water to evaporate from the test liquid reservoir to replace the water condensing into the funnel.

The evaporation and condensation rates were measured based on the syringe pump rate. The vapor pressure was measured with a mercury manometer. Temperatures in the liquid and vapor were measured along the centre line with thermocouples, which were located using a positioning micrometer. The liquid vapor interface position and radius of curvature were established by observation using a cathetometer. Temperatures were measured in the vapor within 1 to 5 mean free paths of the interface. Temperatures in the liquid were measured within 0.25 mm of the interface.

The apparatus was radially symmetric. The liquid vapor interface at the top of the funnel was assumed to be hemispherical. Ward, Fang, and Stanga suggest there is very little heat transfer with, or through the walls of the funnel.

1.2.2 Observations and Results

For evaporation Fang and Ward [2], [3] observed that the interface vapor temperature T_v was as much as 7.8 °C higher than the liquid interface temperature T_l. Their evaporation experiments all involve vapor temperature gradients sloping down towards the interface. They later observed that $T_v > T_l$ is also true for condensation, but with smaller jumps. They observed the same vapor temperature gradient direction in condensation as for evaporation [4]. Figure 1.2 gives the typical characteristics of their measured temperature profiles and jumps [4].

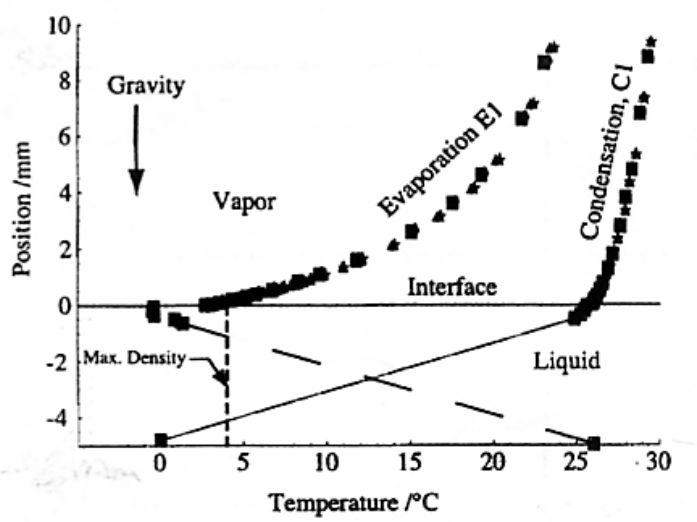

Figure 1.2: Ward et al. experimental evaporation and condensation temperature profiles

1.3 One-dimensional Planar Interface Geometry

The fluxes and gradients are assumed uniform, one-dimensional, and perpendicular to the liquid vapor interface everywhere along the interface. A spherical coordinate system with one-dimensional radial fluxes and gradients should be a good approximation of their experimental system. The geometry is further simplified by approximating the interface as planar. The interface curvature would only affect the saturation pressure, and as we shall see, only if the radius of curvature is much smaller than that observed in the experiments. Figure 1.3 describes the planar geometry.

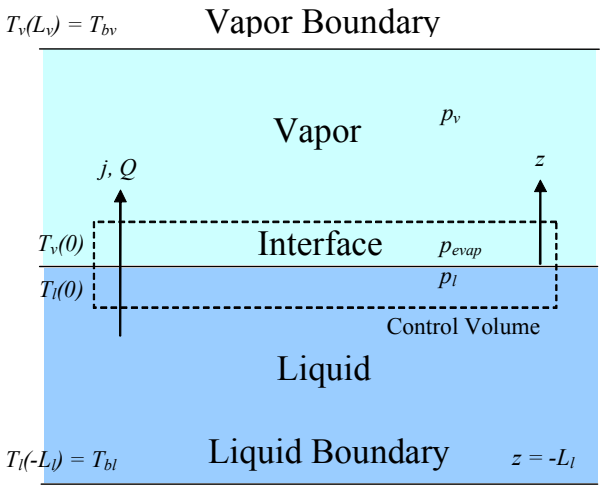

Figure 1.3: One dimensional planar geometry

The one-dimensional mass flux per unit area j, and energy flux per unit area Q, are defined as positive in the positive z direction, the direction of evaporation. All fluxes mentioned in this work are fluxes per unit area; for ease of writing they will simply be referred to as fluxes, and the 'per unit area' will be inferred. At the interface $z = 0$, the liquid temperature is $T_l\,(0)$, and the vapor temperature is $T_v\,(0)$. Often we shall refer to the interface temperatures as T_l, and T_v. The liquid and vapor temperatures are not constrained to be equal. The liquid and vapor boundary temperatures are specified at specific distances away from the interface, such that at the liquid boundary $z = -L_l$, the liquid boundary temperature is $T_l\,(-L_l) = T_{bl}$, and at the vapor boundary $z = L_v$,the temperature is $T_v\,(L_v) = T_{bv}$. The vapor pressure p_v is assume to be uniform. The liquid pressure is p_l. The equivalent pressure of the evaporating molecules is given by p_{evap}. The pressure in the bulk liquid does not play a large role in the analysis, its only requirement is that it must be equal to the vapor pressure next to the interface, otherwise the interface would not be stationary. To avoid confusion we emphasize that p_{evap} is not the pressure in the liquid, but instead is the pressure of the molecules leaving the interface.

With our model we can force mass and energy fluxes by imposing a temperature gradient across the system using unequal boundary temperatures, $T_{bl} \neq T_{bv}$, or by perturbing the vapor

pressure p_v away from the equilibrium pressure We recall that the equilibrium pressure is the saturation pressure $p_{sat}(T)$, at the temperature of the system, T. For equal boundary temperatures $T_{bl} = T_{bv} = T$, a vapor pressure below the saturation pressure $p_v < p_{sat}(T)$ will cause a net evaporation, while $p_v > p_{sat}(T)$, will cause a net condensation.

1.4 Range of Study

We consider slow evaporation and condensation of the order of $10^{-3}\frac{\mathrm{kg}}{\mathrm{m^2\,s}}$ and lower, corresponding to liquid speeds of $10^{-6}\frac{\mathrm{m}}{\mathrm{s}}$, and vapor speeds of $10^{-1}\frac{\mathrm{m}}{\mathrm{s}}$ for the liquid and vapor densities of $10^{3}\frac{\mathrm{kg}}{\mathrm{m^3}}$ and $10^{-2}\frac{\mathrm{kg}}{\mathrm{m^3}}$ respectively. This is partially dictated by the mass flux range of the Ward, Fang, and Stanga experiments [2], [3], [4], but also it is small enough to facilitate the assumption that the system is not far from equilibrium.

Only small pressures of $0.6-5.0\,\mathrm{kPa}$ near the triple point ($0.6\,\mathrm{kPa}$) are considered, which permit the vapor to be described as an ideal gas. This vapor pressure range also corresponds to the experimental parameters.

A small temperature range is used to facilitate the assumption of constant specific heats, and thermal conductivities. We are studying phase change; the range must include the saturation temperature of the chosen vapor pressure. The corresponding temperature range is $0-25\,^{\circ}\mathrm{C}$.

1.5 Overview of Kinetic Theory

Kinetic theory of gases averages the properties of individual molecules to obtain macroscopic properties of the system of molecules, such as pressure, temperature, and density. Harris [6], Riedi [7], Cercignani [8], and Sears and Salinger [9] provide good overviews.

1.5.1 Range of Validity

Simple kinetic theory is derived for monatomic molecules with only translational degrees of freedom. Most kinetic theory research focuses on monatomic molecules, however there are

extensions which incorporate additional degrees of freedom that deal with polyatomic molecules. Cercignani et al. [10], [11], [8], and Soga [12] discuss this further. These theories are more complex, and beyond the scope of this work. Water molecules are polyatomic, however as do other researchers, we approximate them as monatomic.

Kinetic theory was developed for binary collisions, it is valid for any case where only binary collisions take place, such as dilute vapors. This discounts solids, liquids, and dense vapors, where intermolecular collisions often involve more than two molecules. Dilute vapors are ideal gases. Near the triple point, vapor close to the saturation dome can be described as an ideal gas. At higher pressures the ideal gas assumption is no longer valid next to the saturation region. Thus for liquid vapor phase changes, kinetic theory is best suited at low pressures near the triple point.

1.5.2 Velocity Distribution Function

The behavior of a monatomic molecule for any time can be described by its position vector $\underline{\mathrm{r}}$, and velocity vector $\underline{\mathrm{c}}$,

$$\underline{\mathrm{r}} = (x, y, z), \text{ and } \underline{\mathrm{c}} = (c_x, c_y, c_z). \tag{1.1}$$

The statistical behavior of a system of molecules is described by the generalized single molecule distribution function $f\left(\underline{\mathrm{c}}, \underline{\mathrm{r}}, t\right)$, which is defined such that $f\left(\underline{\mathrm{c}}, \underline{\mathrm{r}}, t\right) d\underline{\mathrm{c}} d\underline{\mathrm{r}}$ is the average number of molecules with velocity in the range of $\{\underline{\mathrm{c}},\ \underline{\mathrm{c}} + d\underline{\mathrm{c}}\}$, at position $\{\underline{\mathrm{r}}, \underline{\mathrm{r}} + d\underline{\mathrm{r}}\}$, at time t. Knowledge of the distribution function facilitates the calculation of bulk properties such as:
mass density

$$\rho = m \iiint_{-\infty}^{\infty} f d\underline{\mathrm{c}}, \tag{1.2}$$

pressure

$$p = \iiint_{-\infty}^{\infty} \frac{m}{3} C^2 f d\underline{\mathrm{c}}, \tag{1.3}$$

and internal energy

$$\rho u = \iiint_{-\infty}^{\infty} \frac{m}{2} C^2 f d\underline{\mathrm{c}} = \frac{3}{2} p. \tag{1.4}$$

We use m for the molecular mass, k is the Boltzmann constant, $\underline{C}$ is the peculiar velocity vector, defined as $\underline{C}=\underline{c}-\underline{v}$, and $\underline{v}$ is the mean velocity vector of the vapor. Overall fluxes can also be found, e.g.

the one-dimensional mass flux is

$$j = \int_{-\infty}^{\infty}\!\!\int\!\!\int mc_z f d\underline{c}, \tag{1.5}$$

the one-dimensional momentum flux is

$$M = \int_{-\infty}^{\infty}\!\!\int\!\!\int mc_z^2 f d\underline{c}, \tag{1.6}$$

and the one-dimensional energy flux reads

$$Q = \int_{-\infty}^{\infty}\!\!\int\!\!\int \frac{m}{2} c_z c^2 f d\underline{c}. \tag{1.7}$$

The velocity distribution is a solution of the Boltzmann equation,

$$\frac{\partial f}{\partial t} + c_i \frac{\partial f}{\partial r_i} + F_i \frac{\partial f}{\partial c_i} = \mathcal{S}(f). \tag{1.8}$$

The Boltzmann equation the evolution of f through free flight, binary collisions between molecules, taking into account the interaction potential between the molecules, and the effects of external forces F_i. r_i, and c_i are the molecule position, and velocity vectors in tensor notation. The right hand side of the equation is the collision term, which describes the change of the velocity distributions of the two molecules which collide. From the Boltzmann equation the balances of mass, momentum, energy, and entropy can be derived [8], [6].

In equilibrium, the velocity distribution function does not change with time or location, and there are no external forces acting on the system. The left hand side of the Boltzmann equation is zero. This implies the right hand side is also zero. The solution to this is the Maxwellian distribution,

$$f_m = \frac{p}{kT}\left(\frac{m}{2\pi kT}\right)^{\frac{3}{2}} \exp\left(-\frac{m}{2kT}C^2\right). \tag{1.9}$$

Introduction of the Maxwellian for a gas at rest, $\underline{v}= 0$, into Eqns. (1.2), (1.3), and (1.4) yields the ideal gas law,

$$p = \rho\frac{k}{m}T, \tag{1.10}$$

and the kinetic theory definition of internal energy

$$u = \frac{3}{2}\frac{k}{m}T. \tag{1.11}$$

Non-equilibrium solutions of the Boltzmann equation are considerably more complex. The Boltzmann equation can be solved by computer either directly, or by Direct Simulation Monte Carlo (DSMC), both of which are computationally expensive. For this reason, and because the necessary computational power was not always available, simplifications were devised. A widely used simplification which replaces the collision term with a simpler expression is the Bhatnagar, Gross, Krook, and Welander (BGKW) model.

An alternate method is the Chapman-Enskog (CE) method which expands the distribution function about the Knudsen number Kn. The Knudsen number is the ratio of the mean distance a molecule travels between collisions (mean free path), to a macroscopic length associated with the vapor. The first order CE expansion of the Boltzmann equation yields the first order CE distribution, a first approximation of the non-equilibrium velocity distribution,

$$f_{ce} = f_m\left(1 - \frac{2}{5}\frac{\kappa}{p}\frac{m}{k}C_k\left(\frac{mC^2}{2kT^2} - \frac{5}{2T}\right)\frac{\partial T}{\partial x_k} + \frac{2}{5}\frac{\kappa}{p}\frac{m}{k}C_{\langle k}C_{i\rangle}\frac{m}{kT}\frac{\partial v_{\langle i}}{\partial x_{k\rangle}}\right). \tag{1.12}$$

Here κ is the thermal conductivity. From Navier Stokes,

$$\frac{\partial v_{\langle i}}{\partial x_{k\rangle}} = \frac{-p_{\langle ik\rangle}}{\mu}, \tag{1.13}$$

where μ is the viscosity, and the trace-free pressure tensor is given by

$$p_{\langle ik\rangle} = p_{ik} - \frac{1}{3}p_{nn}\delta_{ik.} \tag{1.14}$$

If we assume the istropic pressure, and neglect shear stresses, Eqn. (1.14) reduces to

$$p_{\langle ik \rangle} = 0 \tag{1.15}$$

If follows then from Eqn. (1.13) that the CE distribution for isotropic pressure without shear stress is

$$f_{ce} = f_m \left(1 - \frac{2}{5} \frac{\kappa}{p} \frac{m}{k} C_k \left(\frac{mC^2}{2kT^2} - \frac{5}{2T} \right) \frac{\partial T}{\partial x_k} \right). \tag{1.16}$$

For equilibrium conditions, zero mean vapor velocity $v_z = 0$, and zero temperature gradient $\frac{\partial T}{\partial x_k} = 0$, the CE distribution reduces to the equilibrium Maxwellian.

Another popular method of approximating the Boltzmann equation is Grad's moment method which is beyond our scope and will not be discussed, e.g. see [6].

1.5.3 Hertz-Knudsen Mass Flux

Kinetic theory represents the liquid-vapor-interface as a wall which emits molecules into the vapor, and with which incident vapor molecules collide, and are sorbed, or reflected. The evaporating molecules leave the surface with the temperature and pressure p_{evap} of the surface[1]. The condensing molecules hit the surface with the temperature and pressure of the vapor at the surface. The velocity distributions of condensing and evaporating molecules are not necessarily the same. This can lead to temperature jumps across the interface. Schrage [1] gives a good discussion on temperature jumps. Figure 1.4 represents the condensing molecules with the distribution $f_v\left(p_v, T_v\right)$, where p_v and T_v are the vapor pressure, and temperature at the interface. The evaporating molecules are represented by the distribution $f_l\left(p_{evap}, T_l\right)$, a function of the pressure of the evaporating molecules, and the liquid interface temperature.

[1] Recall that p_{evap} is defined as the pressure of the molecules that evaporate.

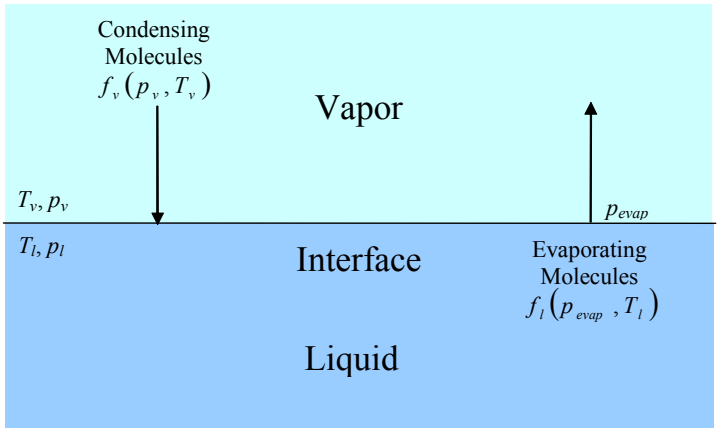

Figure 1.4: Evaporation and condensation velocity distributions

The Hertz-Knudsen (HK) mass flux is a simple one-dimensional kinetic theory expression describing condensation and evaporation. Hertz and Knudsen [13], [14] assume that the vapor is sufficiently close to equilibrium to model the condensing and evaporating molecules using Maxwellians with zero mean vapor velocity. Eqn. (1.5) is split into half-space integrals to accommodate the different condensation and evaporation distributions,

$$j = \iiint\limits_{c_z>0} mc_z f_l\left(p_{evap}, T_l\right) d\underline{c} + \iiint\limits_{c_z<0} mc_z f_v\left(p_v, T_v\right) d\underline{c}. \tag{1.17}$$

The integrated result is the HK mass flux,

$$j = \left(\frac{m}{2\pi k}\right)^{\frac{1}{2}} \left(\frac{p_{evap}}{\sqrt{T_l}} - \frac{p_v}{\sqrt{T_v}}\right). \tag{1.18}$$

The first term represents the molecules evaporating at liquid interface properties T_l and p_{evap}, and the second term gives the flux of molecules condensing with the vapor interface properties T_v and p_v. In equilibrium the mass flux is zero, the temperature T across the interface is constant, and the vapor pressure is equal to the saturation pressure $p_{sat}(T)$. We then see from Eqn. (1.18) that in equilibrium

$$p_{evap} = p_{sat}(T). \tag{1.19}$$

This should still be true for small perturbations from equilibrium; we can then replace p_{evap}

with $p_{sat}(T_l)$ in Eqn. (1.18). It is standard practice to assume the liquid phase is never far from equilibrium; this allows the molecules leaving the interface to be described by the Maxwellian. This yields the HK mass flux as

$$j = \left(\frac{m}{2\pi k}\right)^{\frac{1}{2}} \left(\frac{p_{sat}(T_l)}{\sqrt{T_l}} - \frac{p_v}{\sqrt{T_v}}\right). \tag{1.20}$$

1.5.4 Condensation and Evaporation Coefficients

The HK mass flux assumes all molecules that hit the liquid vapor interface condense instead of bouncing back into the vapor, and all molecules that evaporate stay in the vapor. The condensation coefficient θ_c, and the evaporation coefficient θ_e remove this limitation. θ_c is defined as the ratio of incident molecules sorbed by the surface to those which hit the surface. Molecules which do not stay in the liquid are bounced back into the vapor. Accordingly, $\theta_c = 1$ if all incident molecules condense, and $\theta_c = 0$ if all molecules are bounced back into the vapor.

The evaporation coefficient θ_e is not as easily defined. It is a measure of how many molecules escape from the surface into the vapor. Unlike condensation, there is no surface in the vapor to bounce off of to return to the liquid. This results in multiple definitions for θ_e. Two popular definitions are, the ratio of the number of molecules that enter the vapor phase divided by the number of molecules that leave the liquid phase, and the ratio of the measured evaporation rate to the HK evaporation rate. Figure 1.5 demonstrates the use of the evaporation and condensation coefficients. Note that the reflected particle distributions are not forced to be the same as the incident distributions.

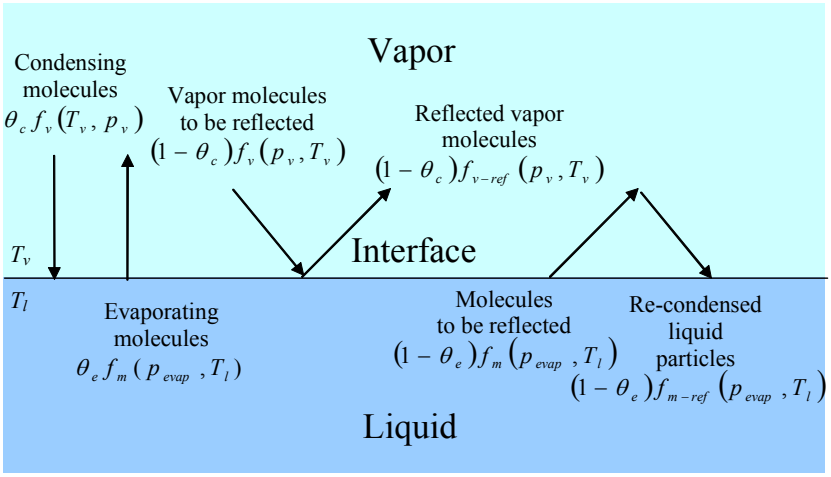

Figure 1.5: Evaporation and condensation with reflection

The HK mass flux with condensation, and evaporation coefficients is

$$j = \left(\frac{m}{2\pi k}\right)^{\frac{1}{2}} \left(\frac{\theta_e p_{sat}(T_v)}{\sqrt{T_l}} - \frac{\theta_c p_v}{\sqrt{T_v}}\right). \tag{1.21}$$

There is much debate regarding the values, and dependencies of θ_c and θ_e. Eames et al. [15], and Marek and Straub [16] reviewed the water condensation and evaporation coefficient literature, and found that published values for each vary between 0.01 to 1. It is agreed upon that θ_c and θ_e are equal in equilibrium. The classic opinion is that they are constants [15] [16]. If this is the case, then they must also be equal outside equilibrium to satisfy equilibrium conditions. We see this from Eqn. (1.21): $j = 0$ for the equilibrium conditions $T_l = T_v = T$ and $p_v = p_{sat}(T)$ only if $\theta_e = \theta_c$.

Schrage [1] devised a correction factor for the HK mass flux to account for a small non-zero net vapor velocity v_z. Barret and Clement [17] present Schrage's equation in the form

$$j = \left(\frac{2}{2-\theta_c}\right)\left(\frac{m}{2\pi k}\right)^{\frac{1}{2}} \left(\frac{\theta_e p_{sat}(T_l)}{\sqrt{T_l}} - \frac{\theta_c p_v}{\sqrt{T_v}}\right), \tag{1.22}$$

which assumes $v_z^2 = 0$. Eqn. (1.22) incorporates the evaporation and condensation coefficients.

For $\theta_e = \theta_c = 1$, the Schrage equation reduces to exactly twice the HK result. Ytrehus [18] through comparison with the BGKW equation, and DSMC simulations finds HK underestimates the mass flux by an approximate order of two. He also observes that the Schrage expression leads to a slightly overestimated mass flux, likely due to neglect of collisional effects in the Knudsen layer. The Knudsen layer, which we discuss at the end of this section, is a transitional layer between the bulk vapor and the interface. Labuntsov [19] revised the Schrage equation to consider non-equilibrium effects in the Knudsen layer,

$$j = \left(\frac{2}{2 - 0.798\theta_c}\right)\left(\frac{m}{2\pi k}\right)^{\frac{1}{2}}\left(\frac{\theta_e p_{sat}\left(T_l\right)}{\sqrt{T_l}} - \frac{\theta_c p_v}{\sqrt{T_v}}\right). \tag{1.23}$$

Barret and Clement [17] suggest that the Schrage velocity distribution violates the conservation of energy and momentum. Their conclusion is drawn from comparison of interface expressions to bulk flux expressions. The equations we present later incorporate the Schrage correction, without violation of the conservation laws. This will be discussed further then.

1.5.5 Accommodation Coefficient

The concept of molecules reflecting off the interface and bouncing back into the vapor has been discussed. The distribution of the rebounding molecules must now be mentioned. Molecules can interact with the interface with two limiting conditions: specular, or diffuse reflection. Specular reflection describes molecules that maintain their energy, and do not react thermally with the surface.

The specularly reflected molecules are considered to maintain the temperature and pressure of the incident molecules. They also maintain the distribution of the incident molecules, except with mirrored velocities. Diffuse reflection describes molecules which do not conserve their energy, and undergo a complete thermal interaction with the surface.

Diffusely reflected molecules take on the temperature of the surface, and the Maxwell distribution of the evaporating molecules. Of course, diffusely reflected molecules must still satisfy the conservation of mass. This is done by introducing an equivalent pressure p^* which is established based on the conservation of mass. To distinguish between specular and diffuse reflection an

accommodation coefficient γ is employed, where $\gamma = 1$ for specular reflection, and $\gamma = 0$ for diffuse reflection. The accommodation coefficient plays an important role in the afore mentioned temperature jump. Figure 1.6 shows the specularly, and diffusely reflected distributions.

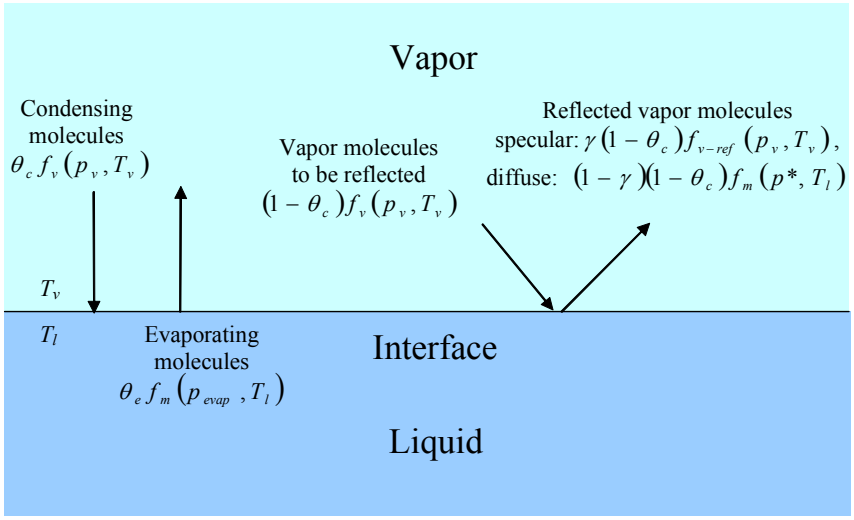

Figure 1.6: Specular and diffuse reflection distributions

The concept of diffuse and specular reflection was introduced by Maxwell, to obtain a useful analytical model for the complicated interaction processes taking place.

1.5.6 Knudsen Layer

We have already mentioned that vapor molecules striking a wall are assumed to have the bulk vapor distribution, and those leaving a wall have a distribution associated with the wall. Close to the wall these two different molecular streams collide with each other, altering the distributions of each. The collisions cause the distribution of the escaping molecules to approach that of the bulk vapor. The region where this equilibration occurs is referred to as the Knudsen layer, see Figure 1.7. Typically it extends approximately one mean free path from the wall. In Figure 1.7 the bulk vapor is described by the distribution f_{bulk}, and the molecules leaving the wall by distribution f_{wall}.

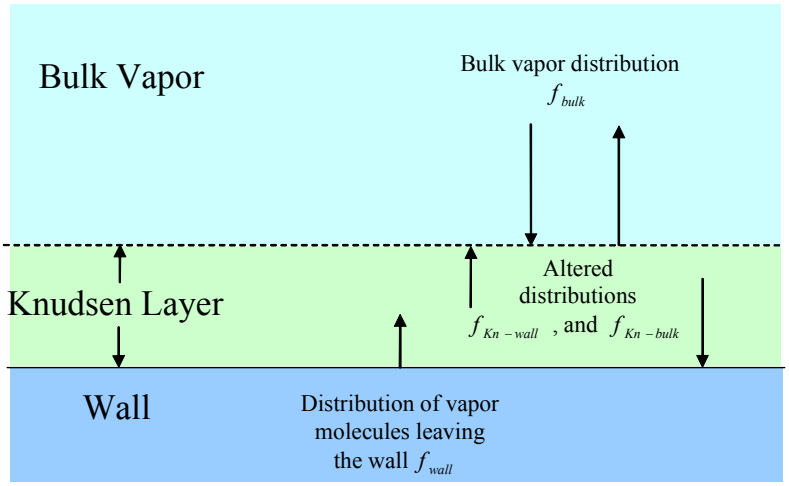

Figure 1.7: Vapor molecule velocity distrubution showing the Knudsen layer

Within the Knudsen layer, the velocity distributions of both molecule streams can no longer be described by the bulk vapor, or wall distributions. In Figure 1.7 the altered distribution of the molecules approaching the wall is $f_{Kn-bulk}$, and the altered distribution of the molecules leaving the wall is $f_{Kn-wall}$. The altered distributions change with location, making them very difficult to resolve. Since the incident vapor molecules no longer have the bulk vapor distribution, the bulk characteristics of the vapor near the wall will be altered. However, the effects are usually small, for small to intermediate Kn. Because of this, and the complexity of the altered distribution functions, the Knudsen layer is usually neglected, or set to zero thickness, and incident molecules are assumed to posses the bulk vapor distribution up to the wall. Sone [20], Cercignani [8], Rebrov [21], and Meland et al. [22] provide a more detailed analysis of the Knudsen layer. In our work Knudsen layer effects are neglected.

1.6 Overview of Irreversible Thermodynamics

Irreversible thermodynamics facilitates the macroscopic description of irreversible processes. Unlike kinetic theory it is not limited to dilute monatomic fluids; its range of application is significantly more broad. Some of its applications include: heat conduction, viscous flow,

chemical reactions, various thermoelectric phenomena, and phase change. De Groot and Mazur [23], and Bedeaux [24] provide an overview of non-equilibrium thermodynamics, which we refer to as irreversible thermodynamics.

An irreversible process is characterized by a positive rate of entropy production, $\sigma > 0$. This implies the system is out of equilibrium. Conversely an equilibrium or quasi equilibrium process is considered to be reversible, with $\sigma = 0$. The conservation laws for mass, energy, and entropy and the relations between properties (i.e. the Gibbs equation) can be used to write the entropy production as the sum of thermodynamic forces multiplied by thermodynamic fluxes,

$$\sigma = \sum_i J_i X_i. \tag{1.24}$$

Here, J_i are the fluxes, while X_i are the accompanying forces. In equilibrium, the entropy production, the fluxes, and the forces are all zero. Irreversible thermodynamics assumes a process is near enough to equilibrium to employ a linear phenomenological law to describe the fluxes as linear functions of their forces,

$$J_i = \sum_k L_{ik} X_k. \tag{1.25}$$

L_{ik} are the phenomenological coefficients. Their values are found experimentally, or theoretically from kinetic theory, or molecular dynamic simulations. Indeed it is known empirically that a wide range of non-equilibrium processes can be described using linear phenomenological laws [23].

An example of a pair of forces and fluxes is Fourier's law of heat conduction, the conductive heat flux with the temperature gradient force, and conductivity coefficient.

The terms in Eqn. (1.25) where $i \neq k$ are considered as cross over terms. They give the dependency of a flux on the other forces with which it is not directly associated in the entropy production. De Groot and Mazur [23] demonstrate the Onsager reciprocal relations [25], [26] which state the phenomenological coefficient matrix must be symmetric, $L_{ik} = L_{ki}$.

The second law of thermodynamics tells us the entropy production can not be negative. This

implies from Eqns. (1.24), and (1.25), that the phenomenological matrix must be positive definite. We find for a 2×2 matrix that

$$L_{ii} > 0,\ L_{kk} > 0, \text{ and } L_{ii}L_{kk} - L_{ik}^2 > 0 \tag{1.26}$$

to ensure a non-negative entropy production.

Bedeaux et al. [27] introduce an interface surface phase at temperature T_s. They find the entropy production across the interface for one-dimensional steady state flow to be

$$\sigma = q_l \left(\frac{1}{T_s} - \frac{1}{T_l} \right) + q_v \left(\frac{1}{T_v} - \frac{1}{T_s} \right) - j_m \left(\frac{\mu_v - \mu_l}{T_s} \right). \tag{1.27}$$

It is in the form of force-flux products. Here, q_l is the conductive flux from the liquid into the surface, q_v is the conductive flux from the surface into the vapor, j_m is the molar flux, and μ_v and μ_l are the vapor and liquid chemical potentials evaluated at T_s. If we apply the same assumption here as in kinetic theory, that the surface temperature is the same as the adjacent liquid temperature, $T_s = T_l$, the entropy production reduces to

$$\sigma = q_v \left(\frac{1}{T_v} - \frac{1}{T_l} \right) - j_m \left(\frac{\mu_v - \mu_l}{T_l} \right). \tag{1.28}$$

Bedeaux [27] points out that this assumption is crucial to make irreversible thermodynamics compatible with kinetic theory. Bedeaux and Kjelstrup arrive at the same expression in a later paper [28]. Using the Onsager reciprocal relations the phenomenological interface molar and conductive heat fluxes are

$$q_v = L_{qq} \left(\frac{1}{T_v} - \frac{1}{T_l} \right) - L_{qj} \left(\frac{\mu_v - \mu_l}{T_l} \right), \tag{1.29}$$

and,

$$j_m = L_{jq} \left(\frac{1}{T_v} - \frac{1}{T_l} \right) - L_{jj} \left(\frac{\mu_v - \mu_l}{T_l} \right). \tag{1.30}$$

The Onsager symmetry relation requires $L_{jq} = L_{qj}$. This stipulates that there are only three independent coefficients describing steady state evaporation, and condensation.

1.7 Relevant Research

1.7.1 Statistical Rate Theory

Ward and Fang [5] suggested statistical rate theory (SRT) as an alternative to kinetic theory and irreversible thermodynamics. The approach is based on the quantum mechanics concept of transition probability, and the Boltzmann definition of entropy. They derive a non linear expression for the steady state molecular flux,

$$j_m = 2k_s \sinh\left[\frac{\mu_l}{kT_l} - \frac{\mu_v}{kT_v} + \frac{h_v}{k}\left(\frac{1}{T_v} - \frac{1}{T_l}\right)\right] \tag{1.31}$$

where

$$k_s = \frac{\vartheta p_{sat}\left(T_l\right)}{\sqrt{2\pi m k T_l}}, \text{ and } \vartheta = \exp\left(\frac{\upsilon_l\left(T_l\right)}{kT_l}\left(p_l^e - p_{sat}\left(T_l\right)\right)\right). \tag{1.32}$$

h_v is the vapor enthalpy at the interface. They point out that SRT is free of fitting parameters, unlike kinetic theory and irreversible thermodynamics. On closer observation the exponential term is, as we will show later, exactly the dimensionless form of the mass-force term of irreversible thermodynamics. The coefficient k_s is a per unit molecule version of the first term of the HK mass flux (1.20) which describes the evaporative flux of the molecules where all molecules evaporate and condense $\theta_c = \theta_e = 1$; this implies SRT assumes $\theta_c = \theta_e = 1$, which Ward partially points out by stating the SRT expression assumes all molecules hitting the interface condense [29]. Ward and Fang [5] compare SRT to their experimental results and conclude that SRT correctly predicts the temperature jump across the interface. Unlike kinetic theory, and irreversible thermodynamics, SRT does not provide an energy flux expression. Ward demonstrates this by not including the energy flux in his SRT entropy production [29], however this omission is not discussed.

1.7.2 Phenomenological Coefficients

Cippolla et al. [30] give kinetic theory values for the phenomenological coefficients, L_{qq}, L_{jj}, and L_{qj}. They note that interface pressure and temperature jump are the respective forces for mass and energy flux. They use their kinetic theory temperature and pressure jump results to derive kinetic theory expressions for the phenomenological coefficients, where the condensation

coefficient is the only free choice in their expressions. Sone and Onishi [31] derive similar kinetic theory phenomenological coefficient values.

Bedeaux and Kjelstrup [28] compare the Cippolla et al. [30] coefficient values to values obtained from Fang and Ward 's [2] experimental data. They find that the kinetic theory values are 30 to 100 times greater than the experimental values, and that adjustment of the condensation coefficient is not sufficient to improve the fit. They hypothesize that multiparticle events play an important role in evaporation. Since kinetic theory only deals with single particle events, it is not sufficient to describe the evaporation process. Bedeaux and Kjelstrup go on to say that irreversible thermodynamics can agree with Fang and Ward 's measurements, and SRT, if the appropriate phenomenological coefficients are used, but the coefficients do not agree with those from kinetic theory. Because kinetic theory coefficients are in such disagreement to experimental values, they conclude, as Fang and Ward do, that kinetic theory is inadequate in this case [28] [2].

1.7.3 Interface Temperature Jump

We have already mentioned that the liquid and vapor interface temperatures are not constrained to be equal outside of equilibrium. We have seen that differences in velocity distributions can lead to temperature jumps in kinetic theory. Sone and Onishi [32], and Young [33] find that kinetic theory predicts $T_v > T_l$ for condensation, and $T_v < T_l$ for evaporation. Kjelstrup et al. [34] find the same using irreversible thermodynamics.

Wylie and Brodkey [35] find a similar result experimentally. They measure a temperature jump of up to 5 °C with $T_v > T_l$ during the condensation of mercury. The condensation temperature jump direction is in agreement with that found by Ward, Fang, and Stanga. However, for evaporation the direction of the temperature jump is opposite to that of Ward, Fang, and Stanga [2], [3], [4].

1.7.4 Parallel Surface Geometry

A popular configuration for studying one-dimensional evaporation and condensation phenomena is the parallel surface geometry. It consists of a vapor surrounded on both sides by its condensed phase. Only the surfaces of the condensed phases are considered in the analysis, reducing the problem to two parallel surfaces, separated by vapor. The temperature of one surface is held higher than the other, forcing mass and heat flux from one side to the other. At the hot surface there is a net evaporation into the vapor, while at the cold surface the vapor condenses.
Pao [36], [37] investigated parallel surfaces using the BGKW model. He found that the vapor temperature gradient could be made to oppose the applied temperature difference between the two interfaces for

$$\Delta h > \frac{9}{2} k T^{avg}.$$

Here Δh is the latent heat of vaporization, and T^{avg} is the mean temperature between the two surfaces. This phenomenon has come to be known as an inverted vapor temperature profile. Pao's expression says nothing about the amplitude of the temperature difference between the two plates, which must be overcome to achieve the temperature gradient. The inverted temperature profile has been a subject of much speculation and discussion in many papers. Koffman et al. [38] even question the validity of a theory that yields an inverted temperature profile.

The inverted profile is due to interface temperature jumps. The afore mentioned kinetic theory temperature jump directions tell us that for condensation $T_v > T_l$, and for evaporation $T_v < T_l$. This is illustrated in Figure 1.8. As the temperature jumps increase, the vapor temperature gradient approaches inversion.

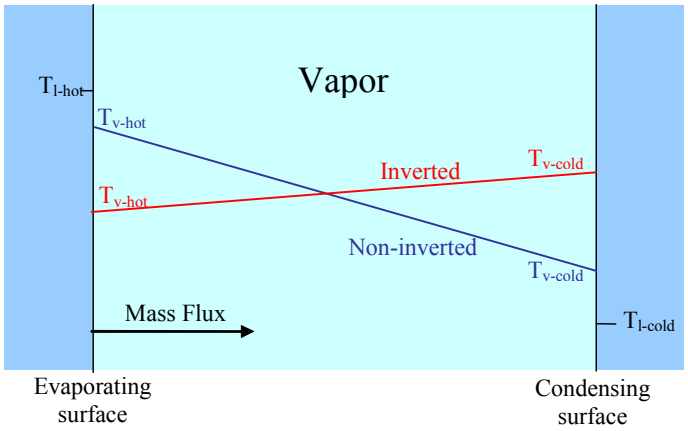

Figure 1.8: Parallel surface non-inverted, and inverted temperature profiles

Meland and Ytrehus [39] using the moment method investigated the dependence of the inverted temperature gradient on the condensation coefficient. They find that if

$$\frac{\Delta h}{RT_{l-cold}} > 4.8 + 8\left(\frac{1-\theta_c}{\theta_c}\right) \tag{1.33}$$

the vapor temperature profile will be inverted. T_{l-cold} is the temperature of the cold surface. Cipolla et al. [30] evaluate the BGKW model to obtain the pressure and temperature jumps at the interface. They find the interface temperature jump arising from the conductive heat flux, and mass flux is independent of the condensation coefficient. Since the existence of the inverted temperature profile is directly related to interface temperature jump, the findings of Cipolla are contradictory to those of Meland and Ytrehus.

Kjelstrup et al. [34] discuss the inverted temperature profile from an irreversible thermodynamics point of view. They consider only the cold surface where condensation takes place, the right hand side of Figure 1.8. They define the positive direction as from the vapor toward the surface (opposite to our definition), and find that the sign of the interface temperature jump $T_v - T_l$ is the same as that of the vapor temperature gradient in an inverted profile, and the opposite for a non-inverted profile. This implies that the temperature jump does not flip with the vapor temperature gradient.

We recall that Bedeaux [27] defined the conductive energy flux q_v travelling in the vapor away from the surface as positive. Figure 1.9 shows the directions of the positive conductive energy flux at each surface. For a non-inverted profile $q_v > 0$ at the evaporating surface, and $q_v < 0$ at the condensing surface. The opposite is true for the inverted profile, $q_v < 0$ for evaporation, and $q_v > 0$ for condensation.

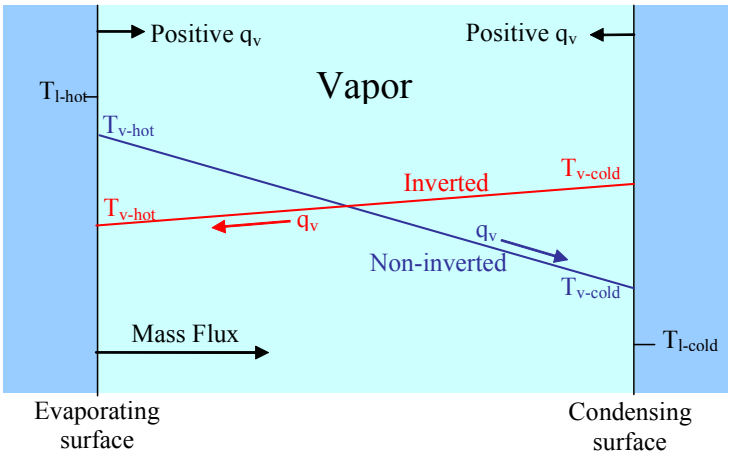

Figure 1.9: Conductive energy flux directions

Fourier's law shows that

$$q_v \sim -\frac{dT_v}{dz}. \tag{1.34}$$

We first consider the non-inverted profile, where from Figure 1.9 at the evaporating surface, $T_v < T_l$ and $\frac{dT}{dz} < 0$, and at the condensing surface $T_v > T_l$ and $\frac{dT}{dz} > 0$. For the inverted case the jumps are the same, but the gradient direction changes, that is at the evaporating surface, $T_v < T_l$ and $\frac{dT}{dz} > 0$, and at the condensing surface $T_v > T_l$ and $\frac{dT}{dz} < 0$. Keeping in mind that the positive direction here is away from the surface, this agrees with Kjelstrup et al.'s [34] stipulation relating the temperature jump and gradient signs to the inverted profile and non-inverted profile, mentioned earlier.

We apply Fourier's law to Eqn. (1.29), and write the first term to show the temperature jump,

$$\frac{dT}{dz} \sim L_{qq}\frac{1}{T_l T_v}\left(T_v - T_l\right) + L_{qj}\left(\mu_v - \mu_l\right). \tag{1.35}$$

This shows that the sign of the cross over term, $L_{qj}\,(\mu_v - \mu_l)$, must be opposite to that of the temperature difference for the signs of the temperature difference and gradient to oppose each other. Kjelstrup et al. [34] conclude $L_{qj} < 0$ for an inverted temperature profile to be possible, recall that $L_{qq} > 0$ in any case.

Shankar and Deshpande [40] investigate the parallel surface problem experimentally. They observe nearly inverted temperature profiles. Figure 1.10 is an excerpt from their results. The jump directions are as predicted by kinetic theory.

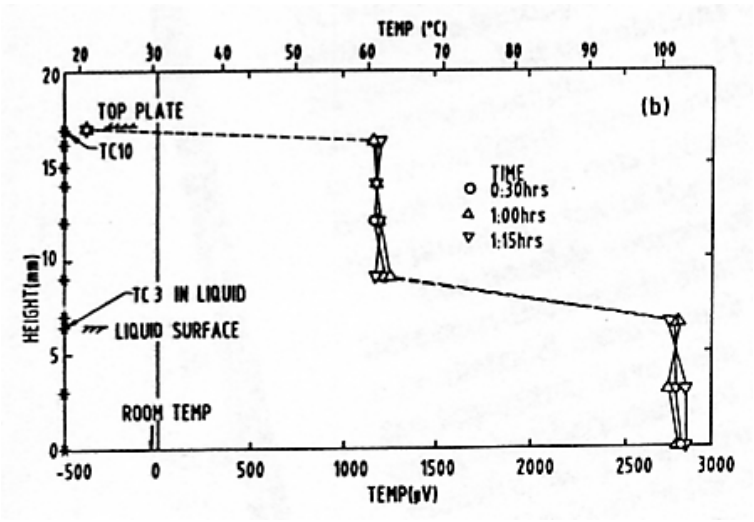

Figure 1.10: Parallel surface temperature measurements

1.7.5 Molecular Dynamics Simulations

MD simulations provide the possibility to study liquid vapor interface characteristics in detail. In MD simulations the translational motion of molecules in a simulation box is calculated according to Newton's second law, $F = ma$. The force is often approximated as a sum of pair interactions between molecules. Meland et al. [41] give a good overview.

Yasuoka and Matsumoto [42] perform MD simulations of argon (monatomic gas). They conclude that for temperatures of 80 K, and 100 K, the condensation coefficient is close to unity and nearly independent of temperature. Matsumoto [43] also conducted MD simulations for argon,

water, methanol, and acetic acid. He observed for argon that the condensation coefficient is constant until approximately 100 K. This agrees with the findings of Yasuoka and Matsumoto [42].

Matsumoto [43] found for argon at higher temperatures, water, and acetic acid, that the condensation coefficient is strongly dependant on the surface temperature; it decreases as the surface temperature is increased. It is suggested that this is due to molecular exchange, which takes place when an incident vapor molecule hits the surface and stays, but displaces another molecule from the surface back into the vapor. Higher surface temperatures mean that the surface molecules have greater energy, and are more likely to be bounced off the surface into the vapor. Matsumoto [43] reports molecular exchange causes associating fluids such as water, and alcohols, and fluids at high temperatures to have low condensation coefficients.

Tsuruta et al. [44] use MD simulations for argon to study the effects of translational motion on the condensation and evaporation coefficients. They observe that higher energy vapor molecules are more likely to condense, since they can penetrate more deeply into the surface, thus increasing the number of collisions with liquid molecules. It was also found that surfaces with higher energy (high temperature) reflect molecules more easily. They developed a condensation coefficient expression to reflect these observations,

$$\theta_c = \psi \left[1 - \omega \exp\left(\frac{-E_{mol}}{kT_l} \right) \right]. \tag{1.36}$$

Here, E_{mol} is the translational molecular energy in the direction normal to the surface, and ψ and ω are constants. Tsuruta et al. [44] report they vary from $0.971 - 0.685$, and $0.086 - 0.554$ respectively. Tsuruta et al. [44] also observe that most molecules reflect diffusely, meaning an accommodation coefficient of near zero. Recall that these are values for argon.

Meland and Ytrehus [45] also find the condensation probability is velocity dependant. Tsuruta and Gyoko [46] perform direct simulation Monte Carlo (DSMC) using the velocity dependant condensation coefficient (1.36). Nagayama and Tsuruta [47] derive the condensation coefficient (1.36) for monatomic and polyatomic molecules based on transition state theory, which they use to develop expressions for ψ and ω. They find that the characteristic length ratio

between liquid and vapor plays an important role in evaluating the condensation coefficient, as translational motion dominates rotational motion during the condensation process. They find good agreement with their results when compared to MD simulations for Argon and Water. Meland et al. [41] from their MD simulations conclude that a constant condensation coefficient is inadequate, and agree with the approach taken by Tsuruta et al. [44].

Rosjorde et al. [48] perform equilibrium, and non-equilibrium MD simulations for argon, with which they verify the Maxwellian equilibrium velocity distribution. They point out that even for large temperature gradients the liquid and vapor are each in local equilibrium. They also verify that the surface temperature is approximately the adjacent liquid temperature $T_s \approx T_l$ likely because of the large thermal conductivity of the liquid. Rosjorde et al. [49] find that the mass and energy force-flux relations are linear, even for large temperature gradients. Meland and Ytrehus [45] use MD simulations to determine the velocity distributions of evaporating and reflecting molecules. They find they both resemble drifting Maxwellians. This verifies the necessity to include the net vapor velocity in the analysis.

Frezzotti et al. [50] perform MD simulations for the parallel surface geometry. They find evidence of the onset of the inverted temperature gradient. They report that their results agree with kinetic theory.

1.7.6 Van der Waals Square Gradient model, and Mesoscopic Non-equilibrium Thermodynamics

Bedeaux et al. [51], [52], [53] use a van der Waals square gradient model to describe the non-equilibrium conditions across the liquid vapor interface. The van der Waals equation of state treats the transition between the liquid and vapor phases as continuous. Unlike kinetic theory and irreversible thermodynamics, the interface is modelled as a continuous transition zone. The transition zone between phases is described by adding a term proportional to the square of the density gradient to the Helmholtz free energy. The square gradient term filters down through the balance equations, and entropy production, into the thermal resistivity of the conductive heat flux. This gives rise to significant temperature jumps across the interfacial zone.

Bedeaux et al. [54] also analyze the transition zone from a mesoscopic non-equilibrium thermodynamic point of view. They derive an expression for condensation flux, and an expression for the condensation coefficient found from MD simulations.

1.7.7 Conclusions

In conclusion, standard kinetic theory predicts $T_l > T_v$ for evaporation, and $T_v > T_l$ for condensation. Irreversible thermodynamics predicts $T_v > T_l$ for condensation. For evaporation, irreversible thermodynamics can predict either sign depending on the choice of phenomenological coefficients. Experimental results all agree that $T_v > T_l$ for condensation, but find jumps in both directions for evaporation. Kinetic theory phenomenological coefficient predictions do not agree with experimental results. MD simulations have shown that the condensation coefficient is temperature and molecular velocity dependant, the condensation and evaporation mass and energy fluxes can be modelled using a linear law, the equilibrium velocity distribution is a Maxwellian, $T_s \approx T_l$ is true, and the possible existence of the inverted temperature profile.

Chapter 2

Supporting Equations

The supporting equations provide the framework of our model. This is where many of the necessary assumptions are applied. These are the equations which are solved in conjunction with the interface mass and energy fluxes that will be discussed in the following chapter.

2.1 Balance Laws

General balances of mass, momentum, energy, and entropy are presented. They are simplified for one-dimensional steady state flow in the vapor, liquid, and across the liquid vapor interface. For this, we assume the interface to be a discontinuity of zero thickness.

2.1.1 Balance of Mass

We first consider the bulk fluids away from the interface. The general differential form of the balance of mass in tensor form is [55]

$$\frac{\partial \rho}{\partial t} + \frac{\partial \rho v_i}{\partial x_i} = 0, \tag{2.1}$$

where i is the Cartesian coordinate index. For one-dimensional steady state this reduces to

$$\frac{\partial \left(\rho v_z\right)}{\partial z} = 0 \tag{2.2}$$

where z represents the vertical direction, see Figure 1.3. Eqn. (2.2) implies the mass flux $j = \rho v_z$ is constant with position, and in the bulk liquid

$$j_l = \rho_l v_l = const; \tag{2.3}$$

in the bulk vapor

$$j_v = \rho_v v_v = const. \tag{2.4}$$

The subscripts l, and v represent the liquid and vapor respectively. The signs are chosen such that positive velocity and mass flux are in the positive z direction, which implies for evaporation $j > 0$, and for condensation $j < 0$, see Figure 1.3.

Eqn. (2.2) requires only the steady state, and one-dimensional assumptions which should be valid everywhere including across the interface. We should then expect $j_l = j_v$. This is seen more clearly by considering the control volume surrounding the interface, using the integral version of the mass balance. The integral form of the balance of mass is

$$\int_V \left(\frac{\partial \rho}{\partial t} + \frac{\partial \left(\rho v_i \right)}{\partial x_i} \right) dV = 0, \tag{2.5}$$

where V is the volume of the control volume. Applying Gauss's law, at steady state Eqn. (2.5) reduces to

$$\oint \left(\rho v_i n_i \right) dA = 0, \tag{2.6}$$

the closed surface integral around the surface of the control volume. n_i is the unit normal to the surface, and is positive outwards. We shrink the control volume such that its height above and below the interface approaches zero. For one-dimensional flow in the z direction we then find

$$\left(\rho_v v_v - \rho_l v_l \right) A = 0, \tag{2.7}$$

where A is the interface surface area. Since $A \neq 0$ this reduces to

$$\rho_v v_v = \rho_l v_l. \tag{2.8}$$

We conclude the mass flux is constant through the interface control volume, and in the bulk phases,

$$j = \rho_l v_l = \rho_v v_v = const. \tag{2.9}$$

2.1.2 Balance of Momentum

The conservation of momentum is applied to establish the pressure gradients in the bulk fluids, and the difference across the interface. The general momentum balance in differential form is [55]

$$\frac{\partial \rho v_i}{\partial t} + \frac{\partial \left(\rho v_i v_k + p_{ik}\right)}{\partial x_k} = \rho F_i. \tag{2.10}$$

There are two coordinate indices i, and k. We expand Eqn. (2.10) for steady state,

$$v_i \frac{\partial \rho v_k}{\partial x_k} + \rho v_k \frac{\partial v_i}{\partial x_k} + \frac{\partial p_{ik}}{\partial x_k} = \rho F_i. \tag{2.11}$$

The mass balance, Eqn. (2.2), shows the first term is zero. If we assume isotropic pressure and neglect shear forces, the pressure tensor p_{ik} reduces to $p\delta_{ik}$, where p is the pressure and δ_{ik} is the unit matrix. The only external force present is gravity, so that the force term reduces to $\rho F_i = (0, 0, \rho g)$. With these simplifications the one-dimensional momentum balance reads

$$\rho v_z \frac{\partial v_z}{\partial z} + \frac{\partial p}{\partial z} = \rho g. \tag{2.12}$$

We assume that the product of the vapor velocity, and velocity gradient is small, allowing it to be neglected. If the gravitational force is also neglected, Eqn. (2.12) also shows us the pressure in the vapor is constant,

$$\frac{\partial p_v}{\partial z} = 0, \tag{2.13}$$

a conclusion which we confirm later. Eqn. (2.13) does not apply across the interface; the velocity gradient there will not be zero from Eqn. (2.9) because of the difference in liquid and vapor densities.

We now examine the momentum balance across the interface control volume, Figure 1.3. The integral version of the balance of momentum is

$$\int_V \left(\frac{\partial \rho v_i}{\partial t} + \frac{\partial \left(\rho v_i v_k + p_{ik}\right)}{\partial x_k} \right) dV = \int_V \rho F_i dV. \tag{2.14}$$

With Gauss's law for steady state, and assuming isotropic pressure with no shear forces, this reduces to

$$\oint \left(\rho v_k v_i n_k + p\delta_{ik} n_k\right) dA = \int_V \rho F_i dV. \tag{2.15}$$

The control volume can now be shrunk to zero height, such that it exactly surrounds the liquid vapor interface. This causes $dV \to 0$. For one-dimensional flow the momentum balance becomes

$$p_v - p_l = \rho_l v_l^2 - \rho_v v_v^2. \tag{2.16}$$

We insert the mass balance, Eqn. (2.9), and find the pressure difference across the interface to be

$$p_v - p_l = j^2 \left(\frac{1}{\rho_l} - \frac{1}{\rho_v}\right). \tag{2.17}$$

Since ρ_v is small relative to ρ_l, we find

$$p_v - p_l \approx \frac{-j^2}{\rho_v}, \tag{2.18}$$

which for $\rho_v \approx 10^{-2} \frac{\text{kg}}{\text{m}^3}$ and $j = 10^{-3} \frac{\text{kg}}{\text{m}^2\,\text{s}}$, yields $p_v - p_l \approx -10^{-4}\,\text{Pa}$. This indicates that the liquid interface pressure p_l is very close to the vapor pressure p_v.

If the system was in equilibrium, the mass flux, velocities, and gradients would all be zero. Eqn. (2.17) yields, $p_l = p_v$.

2.1.3 Balance of Energy

The conservation of energy in differential form is [55]

$$\frac{\partial}{\partial t}\left(u + \frac{v^2}{2}\right) + \frac{\partial}{\partial x_i}\left[\rho\left(u + \frac{v^2}{2}\right) v_i + p_{ik} v_k + q_i\right] = \rho F_i v_i. \tag{2.19}$$

u is the internal energy, and q_i is the conductive heat flux. We neglect the kinetic energy term, $\frac{v^2}{2}$, since it will be insignificant relative to the internal energy. If we neglect gravity, and assume isotropic pressure and no shear forces, the one-dimensional steady state energy balance is

$$\frac{\partial}{\partial z}\left[\rho\left(u+\frac{p}{\rho}\right)v_z+q_z\right]=0. \tag{2.20}$$

Like the balance of mass this reduces to constant liquid and vapor total energy fluxes,

$$Q_l = jh_l + q_l = const, \tag{2.21}$$

and

$$Q_v = jh_v + q_v = const. \tag{2.22}$$

The mass balance is invoked for ρv_z. h is enthalpy, $h = u + \frac{p}{\rho}$. The total energy flux is composed of the convective flux jh and the conductive flux q.

As with the mass flux the assumptions required for Eqns. (2.21), and (2.22) are still valid at the interface; we expect to find that Q is constant. To confirm this the integral energy balance is presented,

$$\int_V \left\{\frac{\partial}{\partial t}\left(u+\frac{v^2}{2}\right)+\frac{\partial}{\partial x_i}\left[\rho\left(u+\frac{v^2}{2}\right)v_i+p_{ik}v_k+q_i\right]\right\}dV=\int_V \rho F_i v_i dV. \tag{2.23}$$

We neglect kinetic energy and the gravitational force, and assume isotropic pressure without shear forces. The one-dimensional steady state integral balance across the interface control volume becomes

$$Q = jh_l + q_l = jh_v + q_v = const. \tag{2.24}$$

2.1.4 Balance of Entropy

For irreversible thermodynamics, an expression for the entropy production σ at the interface is required. This is equal to the entropy production of the control volume for zero height. The integral form of the entropy balance is [55]

$$\sigma=\int_V\left[\frac{\partial \rho s}{\partial t}+\frac{\partial}{\partial x_i}\left(\rho s v_i+\frac{q_i}{T}\right)\right]dV\geq 0. \tag{2.25}$$

For steady state one-dimensional flow across the control volume this reduces to

$$\sigma = j\left(s_v - s_l\right) + \frac{q_v}{T_v} - \frac{q_l}{T_l} \geq 0, \tag{2.26}$$

where s_l and s_v are the liquid and vapor entropies evaluated at the liquid and vapor interface properties. The energy flux, Eqn. (2.24) is employed to eliminate the liquid conductive energy flux from the entropy production

$$\sigma = j\left(\frac{g_l}{T_l} - \frac{g_v}{T_v} + h_v\left(\frac{1}{T_v} - \frac{1}{T_l}\right)\right) + q_v\left(\frac{1}{T_v} - \frac{1}{T_l}\right) \geq 0. \tag{2.27}$$

Here g_l, and g_v are the liquid and vapor Gibbs free energies, $g = h - Ts$. The Gibbs free energies and the vapor enthalpy are evaluated at the respective liquid and vapor interface temperatures and pressures. We can again employ the energy flux expression to eliminate the vapor convective energy flux, and express the entropy production in terms of the total energy flux

$$\sigma = j\left(\frac{g_l}{T_l} - \frac{g_v}{T_v}\right) + Q\left(\frac{1}{T_v} - \frac{1}{T_l}\right) \geq 0. \tag{2.28}$$

Eqns. (2.27), and (2.28) are both in the flux-force form discussed in the introduction.

From the irreversible thermodynamics discussion the fluxes and forces are both zero in equilibrium. It follows from Eqn. (2.28) that in equilibrium $Q = 0$, $j = 0$,

$$\frac{1}{T_v} - \frac{1}{T_l} = 0, \tag{2.29}$$

and

$$\frac{g_l}{T_l} - \frac{g_v}{T_v} = 0 \tag{2.30}$$

This indicates that in equilibrium $T_v = T_l$, and $g_l = g_v$. These equilibrium conditions also fulfill Eqn. (2.27).

2.2 Constitutive Assumptions

To write the enthalpies and entropies in terms of temperature and pressure, we assume the liquid water is incompressible, the vapor is an ideal gas, and constant specific heats and thermal conductivities in the liquid and vapor.

2.2.1 Liquid Water as Incompressible

It is common to assume the density of liquid water to be constant. This can be checked approximately using the saturated liquid density. It varies from $1000\frac{\text{kg}}{\text{m}^3}$ to $995\frac{\text{kg}}{\text{m}^3}$ for a pressure range of $0.6 - 5\,\text{kPa}$ [56], a percent difference of 0.5%. This change incorporates changes with saturation temperature. The change in density due to pressure alone will be even smaller.

2.2.2 Water Vapor as an Ideal Gas

The ideal gas assumption assumes a compressibility factor of unity [56]. The dimensionless reduced pressure, $p_r = \frac{p_v}{p_{cr}}$ is an indicator of a vapor's compressibility. Here, p_v is the vapor pressure, and $p_{cr} = 2.209 \times 10^5\,\text{kPa}$ is the critical pressure [56]. Considering the pressure range in this study, the highest reduced pressure is of the order of 10^{-5}. It is sufficiently small that the compressibility is approximately unity [56], which makes the ideal gas assumption reasonable.

2.2.3 Constant Specific Heats

For liquid water as an incompressible liquid, and water vapor as an ideal gas, we now discuss the assumptions of constant specific heats.

The liquid specific heat varies from $c_l = 4.23\frac{\text{kJ}}{\text{kg K}}$ to $c_l = 4.18\frac{\text{kJ}}{\text{kg K}}$ a difference of 1.20% over the temperature range of $273 - 298\,\text{K}$ [56]. It follows that we can approximate the liquid specific heat as constant, and choose it to be $c_l = 4.18\frac{\text{kJ}}{\text{kg K}}$.

A polynomial fitting function for water vapor specific heat in $\frac{\text{kJ}}{\text{kg K}}$ is [56]

$$c_p(T) = \frac{1}{18.015}\left(32.24 + 0.1923 * 10^{-2}T + 1.055 * 10^{-5}T^2 + 3.595 * 10 - 9T^3\right). \tag{2.31}$$

The vapor specific heat changes by 0.5% over the temperature range of $273 - 298\,\mathrm{K}$. The average specific heat is $c_p = 1.865 \frac{\mathrm{kJ}}{\mathrm{kg\,K}}$.

The kinetic theory gives the specific heat for monatomic molecules as [9]

$$c_p = \frac{5}{2}\frac{k}{m}. \tag{2.32}$$

Here m is the molecular mass, and k is the Boltzmann constant . Inserting numeric values for m and k, the kinetic theory specific heat is $c_p = 1.15 \frac{\mathrm{kJ}}{\mathrm{kg\,K}}$. As discussed in the introduction our kinetic theory analyses is performed for monatomic molecules. Water is not monatomic but we approximate it as such. The kinetic theory expressions in the next chapter utilize the kinetic theory specific heat. To provide equality between kinetic theory, the supporting equations, and irreversible thermodynamics, the simulations employ the kinetic theory specific heat instead of the true value for water vapor. There is a 38.5% percent difference between them. We show later that this difference although significant, does not greatly modify the model results.

2.2.4 Liquid and Vapor Enthalpies

Enthalpies are expressed in terms of differences between the actual state and a reference state. Differentiating the definition of enthalpy $h = u + \frac{p}{\rho}$ yields

$$dh = du + \frac{1}{\rho}dp + pd\left(\frac{1}{\rho}\right). \tag{2.33}$$

The last term is zero because of our incompressible assumption. The liquid reference state is given by the liquid enthalpy h_l^o at temperature T_o, pressure p_o. Writing Eqn. (2.33) for the liquid temperature at location z with constant specific heats we find

$$h_l - h_l^o = c_l\left[T_l(z) - T_o\right] + \frac{1}{\rho_l}(p_l - p_o). \tag{2.34}$$

Usual practice is to incorporate the reference term and absolute term together, and neglect the pressure difference. The resulting constant specific heat liquid enthalpy is

$$h_l = c_l \left[T_l(z) - T_o \right]. \tag{2.35}$$

The vapor enthalpy is expressed assuming the vapor specific heat for constant pressure c_p is constant,

$$h_v - h_v^o = c_p \left[T_v(z) - T_o \right]. \tag{2.36}$$

The difference in liquid and vapor enthalpies at reference temperature T_o is constrained to be the enthalpy of vaporization Δh_o at the reference temperature. The enthalpy of vaporization could be included as an additional term in the liquid enthalpy, vapor enthalpy, or partially in both. We have expressed the liquid enthalpy without it, thus it must be included with the vapor enthalpy. Eqn. (2.36) becomes

$$h_v = c_p \left[T_v(z) - T_o \right] + \Delta h_o. \tag{2.37}$$

2.2.5 Liquid and Vapor Entropies

We start with the Gibbs equation in terms of internal energy,

$$Tds = du + pd\left(\frac{1}{\rho}\right). \tag{2.38}$$

For an incompressible liquid the last term is zero. Introducing constant specific heats for the internal energy and integrating yields the liquid entropy as

$$s_l = s_l^o + c_l \ln \frac{T_l(z)}{T_o}. \tag{2.39}$$

Here s_l^o is the liquid entropy at reference temperature T_o.

The vapor entropy is found from the Gibbs equation in terms of enthalpy,

$$Tds = dh - \frac{1}{\rho}dp. \tag{2.40}$$

We use the ideal gas law to express the density and temperature in terms of pressure, and introduce constant specific heats for the enthalpy. The resulting expression is

$$ds = c_p \frac{dT}{T} - \frac{R}{p}dp. \tag{2.41}$$

We integrate, and find the vapor entropy

$$s_v = s_v^o + c_p \ln \frac{T_v(z)}{T_o} - R \ln \frac{p_v}{p_o}. \tag{2.42}$$

s_v^o is the vapor entropy at reference temperature T_o and reference pressure p_o, and p_v is the vapor pressure.

At equilibrium the temperature and pressure are uniform throughout the system, including across the interface. Across an isothermal, and isobaric interface at reference temperature T_o Eqn. (2.40) becomes

$$T_o(s_v^o - s_l^o) = \Delta h_o. \tag{2.43}$$

It follows that the equilibrium entropy difference across the interface at T_o is

$$\Delta s_o = s_v^o - s_l^o = \frac{\Delta h_o}{T_o}. \tag{2.44}$$

2.3 Saturation Pressure

The saturation pressure $p_{sat}(T)$ is the equilibrium pressure of a fluid at temperature T that exists simultaneously in both liquid and vapor phases. We saw from the momentum balance that the pressure across the interface is constant at equilibrium. The entropy balance tells us the temperature and Gibbs free energies are also constant across the boundary. The equilibrium conditions are then

$$p = p_v = p_l = p_{sat}\left(T\right), \quad T = T_v = T_l, \quad g_l = g_v. \tag{2.45}$$

$p_{sat}\left(T\right)$ is the saturation pressure at temperature T. g_l and g_v are the liquid and vapor Gibbs free energies, $g = h - Ts$. Incorporating the constant specific heat enthalpies and entropies the Gibbs free energies become

$$g_l = c_l(T_l - T_o) - T_l\left(s_l^o + c_l \ln\left(\frac{T_l}{T_o}\right)\right), \tag{2.46}$$

and

$$g_v = c_p(T_v - T_o) + \Delta h_o - T_v\left(s_v^o + c_p \ln\left(\frac{T_v}{T_o}\right) - R\ln\left(\frac{p_v}{p_o}\right)\right). \tag{2.47}$$

The liquid and vapor Gibbs free energies are equated at equilibrium,

$$c_l(T - T_o) - T\left(s_l^o + c_l \ln\left(\frac{T}{T_o}\right)\right) = c_p(T - T_o) + \Delta h_o - T\left(s_v^o + c_p \ln\left(\frac{T}{T_o}\right) - R\ln\left(\frac{p}{p_o}\right)\right). \tag{2.48}$$

Solving for $p = p_{sat}\left(T\right)$, using Eqn. (2.44) to replace Δs_o, we find

$$p_{sat}\left(T\right) = p_o \exp\left(\frac{c_l - c_p}{R}\left(1 - \frac{T_o}{T} - \ln\left(\frac{T}{T_o}\right)\right) + \frac{\Delta h_o}{R}\left(\frac{1}{T_o} - \frac{1}{T}\right)\right). \tag{2.49}$$

The results of Eqn. (2.49) calculated with reference temperature $T_o = 25\,^{\circ}\mathrm{C}$, reference pressure $p_o = p_{sat}\left(25\,^{\circ}\mathrm{C}\right) = 3.169\,\mathrm{kPa}$ [56], and the monatomic vapor molecule specific heat $c_p = \frac{5}{2}\frac{k}{m}$, are compared in Figure 2.1 to tabulated data from Cengel and Boles [56].

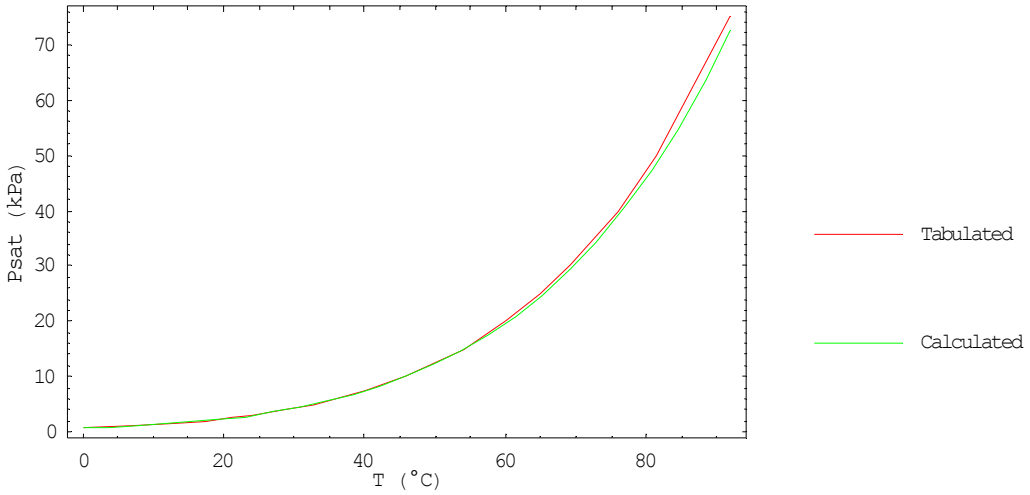

Figure 2.1: Tabulated and calculated saturation pressures versus temperatures

The tabulated and calculated results match very closely over a large temperature range. The percent difference at 0 °C is 0.45% and at 50 °C is 0.73%. Since we chose the reference conditions at 25 °C, the percent difference at this point is zero.

2.4 Fourier's Law of Heat Conduction

We assume the liquid and vapor heat conductivities κ_l, and κ_v are constant. The conductivity of water vapor varies between $1.56 \times 10^{-2} \frac{\mathrm{W}}{\mathrm{m\,K}}$ and $1.81 \times 10^{-2} \frac{\mathrm{W}}{\mathrm{m\,K}}$, a difference of 16% over a temperature range of $270 - 300\,\mathrm{K}$ [57]. The liquid water conductivity varies from $0.555 \frac{\mathrm{W}}{\mathrm{m\,K}}$ to $0.609 \frac{\mathrm{W}}{\mathrm{m\,K}}$, 11% over the same temperature range [57]. We present sensitivity tests in a later section to confirm these variations do not significantly alter the model results.

The one-dimensional Fourier's law for the liquid and vapor reads

$$q_l(z) = -\kappa_l \frac{dT_l}{dz}(z), \tag{2.50}$$

and

$$q_v(z) = -\kappa_v \frac{dT_v}{dz}(z). \tag{2.51}$$

2.5 Liquid and Vapor Temperature Profiles

After inserting the relations for enthalpy (2.35), (2.37), and conductive heat fluxes (2.50), (2.51), the energy balance, Eqn. (2.24), can be written as

$$jc_l\left[T_l(z)-T_o\right]-\kappa_l\frac{dT_l}{dz}=j\left\{c_p\left[T_v\left(z\right)-T_o\right]+\Delta h_o\right\}-\kappa_v\frac{dT_v}{dz}=Q. \tag{2.52}$$

Note that, by Eqns. (2.9), and (2.24) Q, and j, are constants. We group the constant terms together to define new constants

$$T_{cl}=\frac{Q}{jc_l}+T_o\quad,\quad a_l=\frac{\kappa_l}{jc_l}, \tag{2.53}$$

and

$$T_{cv}=\frac{Q}{jc_p}+T_o-\frac{\Delta h_o}{c_p}\quad,\quad a_v=\frac{\kappa_v}{jc_p}. \tag{2.54}$$

With these constants, the liquid and vapor differential equations read

$$T_l\left(z\right)-a_l\frac{dT_l}{dz}=T_{cl}\quad,\quad T_v\left(z\right)-a_v\frac{dT_v}{dz}=T_{cv}. \tag{2.55}$$

They are solved using the variation of parameters. The homogeneous solution is $T=A\exp\left(\frac{z}{a_i}\right)$, where A is a constant of integration. The non-homogeneous solution is found by inserting the homogeneous solution back into the original differential equation, and assuming A is a function of z. We find for the liquid

$$\frac{dA}{dz}(z)=\frac{-T_{cl}}{a_l}\exp\left(-\frac{z}{a_l}\right), \tag{2.56}$$

with the solution

$$A(z)=T_{cl}\exp\left(-\frac{z}{a_l}\right)+B. \tag{2.57}$$

Here, B is another constant of integration. Inserting the solution for A back into the homogeneous solution we find

$$T\left(z\right)=T_{cl}+B\exp\left(\frac{z}{a_l}\right). \tag{2.58}$$

Applying the liquid boundary condition $T_l\left(-L_l\right)=T_{bl}$ yields the liquid temperature profile,

$$T_l(z) = T_{cl} + (T_{bl} - T_{cl}) \exp\left(\frac{z + L_l}{a_l}\right). \tag{2.59}$$

The same procedure is followed for the vapor. Using the vapor boundary condition $T_v(L_v) = T_{bv}$ the vapor temperature profile is

$$T_v(z) = T_{cv} + (T_{bv} - T_{cv}) \exp\left(\frac{z - L_v}{a_v}\right). \tag{2.60}$$

Note that by Eqns. (2.53) and (2.54), the constants T_{cl} and T_{cv} depend on the values of the interface fluxes, j and Q, expressions for which will be discussed in the next two chapters.

Chapter 3

Macroscopic Energy and Mass Flux Expressions

We have now derived the liquid and vapor temperature profiles, and the liquid saturation pressure, all of which can be written in terms of the mass flux j, and the energy flux Q. In order to solve the problem, relations at the interface are needed between j and Q, and the properties of the liquid and vapor. In this section we employ irreversible thermodynamics, and SRT, to develop mass, and energy flux expressions at the liquid-vapor interface.

3.1 Irreversible Thermodynamics

Earlier we combined the entropy production (2.26) with the energy flux (2.24), to find two different force-flux expressions for interface entropy production,

$$\sigma = j\left(\frac{g_l}{T_l} - \frac{g_v}{T_v} + h_v\left(\frac{1}{T_v} - \frac{1}{T_l}\right)\right) + q_v\left(\frac{1}{T_v} - \frac{1}{T_l}\right) \geq 0, \tag{3.1}$$

and

$$\sigma = j\left(\frac{g_l}{T_l} - \frac{g_v}{T_v}\right) + Q\left(\frac{1}{T_v} - \frac{1}{T_l}\right) \geq 0. \tag{3.2}$$

The energy flux (2.24) can be used again to write the entropy production in terms of the conductive flux in the liquid q_l giving a third force-flux expression

$$\sigma = j\left(\frac{g_l}{T_l} - \frac{g_v}{T_v} + h_l\left(\frac{1}{T_v} - \frac{1}{T_l}\right)\right) + q_l\left(\frac{1}{T_v} - \frac{1}{T_l}\right) \geq 0. \tag{3.3}$$

Any one of these three entropy production force-flux combinations could be used to produce phenomenological expressions. The respective force-flux combinations are listed in Table 3.1.

Eqn.	Flux	Force	Flux	Force
3.1	j	$\frac{g_l}{T_l} - \frac{g_v}{T_v} + h_v\left(\frac{1}{T_v} - \frac{1}{T_l}\right)$	q_v	$\frac{1}{T_v} - \frac{1}{T_l}$
3.3	j	$\frac{g_l}{T_l} - \frac{g_v}{T_v} + h_l\left(\frac{1}{T_v} - \frac{1}{T_l}\right)$	q_l	$\frac{1}{T_v} - \frac{1}{T_l}$
3.2	j	$\frac{g_l}{T_l} - \frac{g_v}{T_v}$	Q	$\frac{1}{T_v} - \frac{1}{T_l}$

Table 3.1: Thermodynamic Forces and Fluxes

We see from Table 3.1 that there are three different mass flux forcing expressions. We write the Gibbs free energies in terms of enthalpy and entropy, and find

$$F_1 = \frac{h_l - h_v}{T_l} + s_v - s_l, \tag{3.4}$$

$$F_2 = \frac{h_l - h_v}{T_v} + s_v - s_l, \tag{3.5}$$

and

$$F_3 = \frac{h_l - h_v}{T_l} + h_v\left(\frac{1}{T_l} - \frac{1}{T_v}\right) + s_v - s_l, \tag{3.6}$$

where F_1 is the mass flux forcing from Eqn. (3.1), F_2 is the mass flux forcing from Eqn. (3.3), and F_3 is the mass flux forcing from Eqn. (3.2). We see that F_1 and F_2 are in terms of enthalpy and entropy differences, which are independent of the choice of enthalpy and entropy reference point, but F_3 is dependent on the enthalpy reference. Since the mass flux should not be dependent on the arbitrary choice of reference, we conclude that the F_3 mass forcing should not be considered.

Choosing between the remaining two force pairs in Table 3.1 is not as clearly defined. Both are different from those of Bedeaux and Kjelstrup [28], Eqns. (1.29), and (1.30), discussed in the introduction. However, Bedeaux and Kjelstrup do write their phenomenological expressions in terms of the vapor convective flux q_v, but they do not have the $h_v\left(\frac{1}{T_v} - \frac{1}{T_l}\right)$ term in their force for mass flux. Perhaps a more solid indicator is the mass flux forcing of the SRT expression (1.31), derived independently of irreversible thermodynamics using quantum mechanics and the Boltzmann entropy definition [5], which is the same as the mass forcing from Eqn. (3.1).

Thus we choose the forces and fluxes from Eqn. (3.1) for our irreversible thermodynamics (IT)

analysis. To simplify our analysis we neglect the cross-over terms, and find

$$j = \beta \left(\frac{g_l}{T_l} - \frac{g_v}{T_v} + h_v \left(\frac{1}{T_v} - \frac{1}{T_l} \right) \right), \tag{3.7}$$

and

$$q_v = \alpha \left(\frac{1}{T_v} - \frac{1}{T_l} \right). \tag{3.8}$$

For simplicity of notation we have inserted β, and α as the phenomenological coefficients. As discussed earlier, to ensure positive entropy production they must both be positive.

For equilibrium where $g_l = g_v$, and $T_l = T_v$, we see that Eqns. (3.7), and (3.8) reduce to $j = 0$, and $Q = 0$, satisfying the equilibrium conditions.

3.2 Statistical Rate Theory

As we mentioned earlier, Ward and Fang [5] suggested a SRT expression for the interface molecular flux,

$$j_m = k_s \left\{ \exp\left[\frac{\mu_l}{kT_l} - \frac{\mu_v}{kT_v} + \frac{h_v}{k} \left(\frac{1}{T_v} - \frac{1}{T_l} \right) \right] - \exp\left[\frac{-\mu_l}{kT_l} + \frac{\mu_v}{kT_v} - \frac{h_v}{k} \left(\frac{1}{T_v} - \frac{1}{T_l} \right) \right] \right\}, \tag{3.9}$$

where

$$k_s = \frac{\vartheta p_{sat}(T_l)}{\sqrt{2\pi m k T_l}}, \text{ and } \vartheta = \exp\left\{ \frac{\upsilon_l(T_l)}{kT_l} \left[p_l^e - p_{sat}(T_l) \right] \right\}. \tag{3.10}$$

The chemical potentials per molecule μ_l, and μ_v, as well as the temperatures are evaluated directly at the interface. υ_l is the liquid specific volume per particle, and p_l^e is the liquid equilibrium pressure (different from $p_{sat}(T)$ because of surface tension).

For water in our range of study, $T_l \approx 298\,\mathrm{K}$, and $\upsilon_l \approx 10^{-3}\frac{\mathrm{m}^3}{\mathrm{kg}}$; we estimate $\frac{\upsilon_l(T_l)}{kT_l} \approx 10^{-9}\frac{\mathrm{m}^2}{\mathrm{N}}$. As we shall see, the difference between p_l^e and $p_{sat}(T_l)$ is small, thus $\vartheta \approx 1$, and the factor in front of the exponential reduces to

$$k_s = \frac{p_{sat}(T_l)}{\sqrt{2\pi m k T_l}}. \tag{3.11}$$

This expression has units of molecules per unit area and time. To convert to units of mass which we use for our analysis, we multiply k_s by the molecular mass m to convert to units of mass per unit area and time. The resulting coefficient is

$$k_s = \frac{p_{sat}\left(T_l\right)}{\sqrt{2\pi R T_l}}, \tag{3.12}$$

where $R = \frac{k}{m}$ is the gas constant for water. Again we mention that k_s is exactly the first term of the HK mass flux (1.20) which represents the mass flux of the molecules evaporating from the interface, and that SRT assumes $\theta_c = \theta_e = 1$.

Like k_s the SRT exponents are written in terms of molecules, and not mass. We wish to use Gibbs free energies, and enthalpies per unit mass. To maintain proper unitless form, we must multiply each term by m. The resulting SRT mass flux is

$$j = k_s \left\{ \exp\left[\frac{g_l}{RT_l} - \frac{g_v}{RT_v} + \frac{h_v}{R}\left(\frac{1}{T_v} - \frac{1}{T_l}\right)\right] - \exp\left[\frac{-g_l}{RT_l} + \frac{g_v}{RT_v} - \frac{h_v}{R}\left(\frac{1}{T_v} - \frac{1}{T_l}\right)\right]\right\}, \tag{3.13}$$

with

$$k_s = \frac{p_{sat}\left(T_l\right)}{\sqrt{2\pi R T_l}}. \tag{3.14}$$

The first exponential of Eqn. (3.13) is the dimensionless form of the force for the IT mass flux (3.7). Since the IT expression was derived for positive mass flux in the evaporation direction, we can say that the first exponential term in the SRT expression (3.9) is the evaporation force. The second exponential in the SRT expression is the negative of the mass force; it must be the condensation force.

For equilibrium, where $g_l = g_v$, and $T_l = T_v$, we see Eqn. (3.13) reduces to the equilibrium condition $j = 0$.

3.2.1 Linearized Statistical Rate Theory Mass Flux

When we assume that the terms inside the SRT mass flux exponentials are small, the SRT mass flux can be linearized to give

$$j = 2k_s \left[\frac{g_l}{RT_l} - \frac{g_v}{RT_v} + \frac{h_v}{R} \left(\frac{1}{T_v} - \frac{1}{T_l} \right) \right]. \tag{3.15}$$

Eqn. (3.15) is identical to the IT mass flux expression (3.7), except, here the force is dimensionless, and the coefficient is explicitly defined. We rewrite Eqn. (3.15) in the same form as Eqn. (3.7),

$$j = \frac{p_{sat}\left(T_l\right)}{R^{\frac{3}{2}}} \sqrt{\frac{2}{\pi T_l}} \left(\frac{g_l}{T_l} - \frac{g_v}{T_v} + h_v \left(\frac{1}{T_v} - \frac{1}{T_l} \right) \right). \tag{3.16}$$

We see that the SRT definition of the phenomenological coefficient for mass flux is

$$\beta_{SRT} = \frac{p_{sat}\left(T_l\right)}{R^{\frac{3}{2}}} \sqrt{\frac{2}{\pi T_l}}. \tag{3.17}$$

This coefficient must be positive, since it depends on temperature and pressure, and thus agrees with the phenomenological coefficient non-negative restriction.

SRT does not have an accompanying energy flux expression as in irreversible thermodynamics or kinetic theory. As mentioned at the beginning of this chapter expressions for both j and Q are required to solve the problem. The above analysis shows the SRT mass flux is essentially a non-linear IT mass flux expression. We suggest then, that the IT energy flux (3.8) can be used as a substitute in the absence of an SRT energy flux expression. We further mention that it is important to develop an SRT energy flux expression, a fact which Ward and Fang [5] overlook.

Chapter 4

Kinetic Theory

We now derive mass and energy flux expressions from kinetic theory.

4.1 Mass and Energy Flux Integrals

We recall from the introduction that the one-dimensional mass and energy flux integrals are

$$j = \int_{-\infty}^{\infty}\iiint mc_z f d\underline{c}, \tag{4.1}$$

and

$$Q = \int_{-\infty}^{\infty}\iiint \frac{m}{2} c_z c^2 f d\underline{c}. \tag{4.2}$$

These can be split into half-space integrals

$$j = \iiint_{c_z>0} mc_z f_l\left(p_{evap}, T_l\right) d\underline{c} + \iiint_{c_z<0} mc_z f_v\left(p_v, T_v\right) d\underline{c}, \tag{4.3}$$

and

$$Q = \iiint_{c_z>0} \frac{m}{2} c_z c^2 f_l\left(p_{evap}, T_l\right) d\underline{c} + \iiint_{c_z<0} \frac{m}{2} c_z c^2 f_v\left(p_v, T_v\right) d\underline{c}, \tag{4.4}$$

where we used

$$f = \left\{ \begin{array}{cc} f_l\left(p_{evap}, T_l\right) & c_z > 0 \\ f_v\left(p_v, T_v\right) & c_z < 0 \end{array} \right\}. \tag{4.5}$$

Here $f_l\left(p_{evap}, T_l\right)$ represents molecules evaporating at the liquid interface properties p_{evap}, and T_l, and $f_v\left(p_v, T_v\right)$ describes the condensing molecules at the vapor interface conditions p_v, and

T_v.

4.2 Hertz-Knudsen Mass and Energy Fluxes

The HK flux expressions assume the equilibrium Maxwellian distribution

$$f_m = \frac{p}{kT}\left(\frac{m}{2\pi kT}\right)^{\frac{3}{2}} \exp\left(-\frac{m}{2kT}C^2\right) \tag{4.6}$$

for the evaporating, and condensing molecules, and that the vapor velocity is zero. We recall from our discussion in the Chapter 1 that near equilibrium $p_{evap} = p_{sat}(T)$. Integrating Eqns. (4.3), and (4.4) for

$$f = \left\{ \begin{array}{ll} f_m\left[p_{sat}\left(T_l\right), T_l\right] & c_z > 0 \\ f_m\left(p_v, T_v\right) & c_z < 0 \end{array}, \; v_z = 0 \right\}. \tag{4.7}$$

the resulting HK mass, and energy fluxes are

$$j = \left(\frac{m}{2\pi k}\right)^{\frac{1}{2}} \left(\frac{p_{sat}\left(T_l\right)}{\sqrt{T_l}} - \frac{p_v}{\sqrt{T_v}}\right), \tag{4.8}$$

and

$$Q = \left(\frac{2k}{m\pi}\right)^{\frac{1}{2}} \left(p_{sat}\left(T_l\right)\sqrt{T_l} - p_v\sqrt{T_v}\right). \tag{4.9}$$

In equilibrium we know that $p_v = p_{sat}(T)$, and $T_l = T_v = T$, under these conditions Eqns. (4.8), and (4.9) reduce to the equilibrium condition $j = 0$, and $Q = 0$.

4.3 Chapman-Enskog (first order) with Net Vapor Velocity

A small one-dimensional vapor velocity v_z is introduced into the Maxwellian to account for non-zero vapor velocity. The square of the peculiar velocity vector is

$$C^2 = c^2 - 2\underline{c}\underline{v} + v^2. \tag{4.10}$$

Since the mean vapor velocity is small, $v^2 \approx 0$. We substitute for the peculiar velocity into the Maxwellian (4.6),

$$f_{m-v} = \frac{p}{kT}\left(\frac{m}{2\pi kT}\right)^{\frac{3}{2}} \exp\left(-\frac{m}{2kT}c^2\right) \exp\left(\frac{m}{kT}c_z v_z\right). \tag{4.11}$$

We perform a first order Taylor expansion about zero for the second exponential. The Maxwellian with a small mean gas velocity becomes

$$f_{m-v} = \frac{p}{kT}\left(\frac{m}{2\pi kT}\right)^{\frac{3}{2}} \exp\left(-\frac{m}{2kT}c^2\right) \left(1 + \frac{m}{kT}c_z v_z\right). \tag{4.12}$$

Eqn. (4.12) is incorporated into the first order CE distribution Eqn. (1.16), which for one-dimension, and assuming small vapor temperature gradient and velocity reads

$$f_{ce-v} = f_{m-v}\left(1 - \frac{2}{5}\frac{\kappa}{p}\frac{m}{k}c_z\left(\frac{mc^2}{2kT^2} - \frac{5}{2T}\right)\frac{dT}{dz}\right). \tag{4.13}$$

The mass and energy fluxes are now calculated from Eqns. (4.3), and (4.4) for

$$f = \left\{ \begin{array}{cc} f_m\left[p_{sat}\left(T_l\right), T_l\right] & c_z > 0 \\ f_{ce-v}\left(p_v, T_v\right) & c_z < 0 \end{array} \right\}. \tag{4.14}$$

The CE distribution (4.13) is used to represent the bulk vapor, and the condensing particle velocity distribution. The evaporating molecules are represented by the equilibrium Maxwellian distribution, Eqn. (4.6). The mean velocity of the evaporating molecules is assumed to be equal to velocity of the liquid at the interface. By the balance of mass, Eqn. (2.9), $v_l\rho_l = v_v\rho_v = j$. The liquid density is much greater than the vapor density, $\rho_l >> \rho_v$, which implies $v_l << v_v$. Since the vapor velocity is small, the liquid velocity is therefore negligible. Then it is reasonable to assume that the liquid is close to mechanical and thermodynamic equilibrium. We have already stated that the evaporating molecules take on the liquid interface properties. It follows that the evaporating distribution can be approximated by the equilibrium Maxwellian (4.6), as in the HK expressions.

For the mass flux we obtain

$$j = \left(\frac{m}{2\pi k}\right)^{\frac{1}{2}} \left(\frac{p_{sat}\left(T_l\right)}{\sqrt{T_l}} - \frac{p_v}{\sqrt{T_v}}\right) + \frac{1}{2} v_z \rho_v, \tag{4.15}$$

which, since $j = v_z \rho_v$, simplifies to

$$j = 2\left(\frac{m}{2\pi k}\right)^{\frac{1}{2}} \left(\frac{p_{sat}\left(T_l\right)}{\sqrt{T_l}} - \frac{p_v}{\sqrt{T_v}}\right). \tag{4.16}$$

Thus, the CE mass flux is exactly twice the HK mass flux, Eqn. (4.8).

We find for the energy flux,

$$Q = \left(\frac{2k}{m\pi}\right)^{\frac{1}{2}} \left(p_{sat}\left(T_l\right)\sqrt{T_l} - p_v\sqrt{T_v}\right) - \frac{1}{2}\kappa_v \frac{dT_v}{dz} + \frac{5}{4} p_v v_z. \tag{4.17}$$

We recall the vapor far from the interface is described by $f_{ce-v}\left[p_v, T_v\left(z\right)\right]$, which is valid for molecules traveling towards and away from the surface. Integrating Eqn. (4.2) over full space yields

$$Q = -\kappa_v \frac{dT_v\left(z\right)}{dz} + \frac{5}{2} p_v v_z\left(z\right). \tag{4.18}$$

Evaluated at the interface for $z = 0$,

$$Q = -\kappa_v \frac{dT_v}{dz} + \frac{5}{2} p_v v_z. \tag{4.19}$$

Plugging this into Eqn. (4.17), the CE energy flux is

$$Q = 2\left(\frac{2k}{m\pi}\right)^{\frac{1}{2}} \left(p_{sat}\left(T_l\right)\sqrt{T_l} - p_v\sqrt{T_v}\right). \tag{4.20}$$

As we saw for the mass flux, this is twice the HK energy flux, Eqn. (4.9).

We check that equilibrium is satisfied: as with the HK expressions Eqns. (4.16), and (4.20) yield $j = 0$, and $Q = 0$ for $p_v = p_{sat}\left(T\right)$, and $T_l = T_v = T$.

4.4 Constant Condensation and Evaporation Coefficients-Specular Reflection

We now extend our discussion to include the condensation and evaporation coefficients, θ_c and θ_e. We begin our discussion of reflection with the simpler specular reflection case. We pointed out earlier that specularly reflected molecules maintain their energy, and do not interact thermally with the surface. The reflected molecules have exactly the same energy as they had before they were reflected. This causes the reflected velocity distribution to be identical to the incident distribution, except that the signs of the terms containing the molecular velocity c_z are reversed. As a result the specularly reflected streams do no contribute to the mass and energy fluxes.

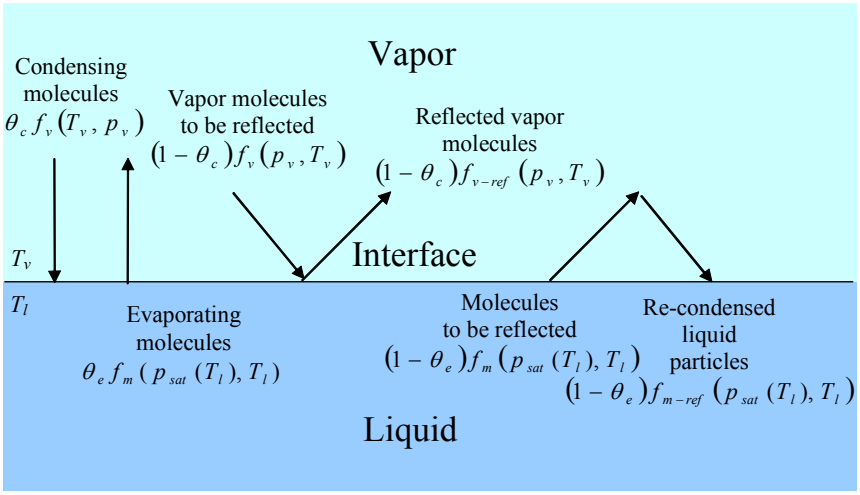

Figure 4.1: Distributions with evaporation and condensation coefficients

4.4.1 Hertz-Knudsen

We see from Figure 4.1, the incident molecules which condense are $\theta_c f_v\,[p_v, T_v]$, and those which evaporate are $\theta_e f_m\,[p_{sat}(T_l), T_l]$. Only those molecules which evaporate or condense will contribute to the mass flux, since the reflected molecules are bounced back to their original phases.

The HK velocity distributions with condensation and evaporation coefficients are then

$$f = \left\{ \begin{array}{ll} \theta_e f_m \left[p_{sat}\left(T_l\right), T_l \right] & c_z > 0 \\ \theta_c f_m \left(p_v, T_v \right) & c_z < 0 \end{array} , \; v_z = 0 \right\}. \tag{4.21}$$

From Eqn. (4.3), the mass flux is

$$j = \left(\frac{m}{2\pi k} \right)^{\frac{1}{2}} \left(\frac{\theta_e p_{sat}\left(T_l\right)}{\sqrt{T_l}} - \frac{\theta_c p_v}{\sqrt{T_v}} \right). \tag{4.22}$$

Since the specularly reflected molecules maintain their energy, the reflected streams will not contribute to the energy flux, similarly to what we saw with the mass flux. Integrating Eqn. (4.4) gives the energy flux as

$$Q = \left(\frac{2k}{m\pi} \right)^{\frac{1}{2}} \left(\theta_e p_{sat}\left(T_l\right) \sqrt{T_l} - \theta_c p_v \sqrt{T_v} \right). \tag{4.23}$$

As expected Eqns. (4.22), and (4.23) reduce to the HK fluxes Eqns. (4.8), and (4.9) for $\theta_e = \theta_c = 1$.

The equilibrium conditions of $p_v = p_{sat}\left(T\right)$, $T_l = T_v = T$, $j = 0$, and $Q = 0$ are only fulfilled by Eqns. (4.22), and (4.23) for $\theta_e = \theta_c$. This reiterates our earlier comments that, if θ_e and θ_c are constants, then they must be equal.

4.4.2 Chapman-Enskog with Net Vapor Velocity

Incorporating θ_e, and θ_c into with the CE velocity distribution we find

$$f = \left\{ \begin{array}{ll} \theta_e f_m \left[p_{sat}\left(T_l\right), T_l \right] & c_z > 0 \\ \theta_c f_{ce-v}\left(p_v, T_v \right) & c_z < 0 \end{array} \right\}. \tag{4.24}$$

Integrating Eqns. (4.3), and (4.4), and following the simplifications discussed for the earlier CE solution, the mass and energy fluxes become

$$j = \left(\frac{2}{2 - \theta_c} \right) \left(\frac{m}{2\pi k} \right)^{\frac{1}{2}} \left(\frac{\theta_e p_{sat}\left(T_l\right)}{\sqrt{T_l}} - \frac{\theta_c p_v}{\sqrt{T_v}} \right), \tag{4.25}$$

and

$$Q = \left(\frac{2}{2-\theta_c}\right)\left(\frac{2k}{m\pi}\right)^{\frac{1}{2}}\left(\theta_e p_{sat}\left(T_l\right)\sqrt{T_l} - \theta_c p_v\sqrt{T_v}\right). \tag{4.26}$$

As we observed with the HK expressions, Eqns. (4.25), and (4.26) reduce to the coefficientless CE equations (4.16), and (4.20) for $\theta_e = \theta_c = 1$.

We see Eqns. (4.25), and (4.26) fulfill the equilibrium conditions of $j = 0$, and $Q = 0$ for $p_v = p_{sat}\left(T\right)$, $T_l = T_v = T$, and $\theta_e = \theta_c$. Again we find that θ_e and θ_c can only be constants if they are equal.

4.4.3 Schrage Velocity Distribution

We see Eqn. (4.25) is the Schrage mass flux (1.22) mentioned in the introduction. Even though we derived it using the CE distribution (4.13), it did incorporate the Maxwellian with net vapor velocity f_{m-v}.(4.12), Schrage's distribution. We now address the claims of Barrett and Clement [17] that the Schrage velocity distribution (4.12) might violate the conservations laws for energy and momentum.

We start by looking at the energy flux expression. The Barrett and Clement [17] derivation assumes specular reflection, thus we use Eqn. (4.4) to derive the interface energy flux. Using the Schrage distribution, with the Maxwellian for evaporation,

$$f = \left\{ \begin{array}{cc} \theta_e f_m\left[p_{sat}\left(T_l\right), T_l\right] & c_z > 0 \\ \theta_c f_{m-v}\left(p_v, T_v\right) & c_z < 0 \end{array} \right\}, \tag{4.27}$$

we find

$$Q = \left(\frac{2k}{m\pi}\right)^{\frac{1}{2}}\left(\theta_e p_{sat}\left(T_l\right)\sqrt{T_l} - \theta_c p_v\sqrt{T_v}\right) + \theta_c\frac{5}{4}p_v v_z. \tag{4.28}$$

Integrating Eqn.(4.2) in the bulk vapor over full space with the Schrage distribution f_{m-v}.(4.12) yields the bulk energy flux,

$$Q = \frac{5}{2}p_v v_z\left(z\right). \tag{4.29}$$

Barrett and Clement [17] suggest the bulk and interface energy flux expressions do not agree. We point out that their equivalence is forced by evaluating Eqn. (4.29) at $z = 0$, substituting

it into Eqn. (4.28), and solving for Q. This yields the Schrage energy flux

$$Q = \left(\frac{2}{2-\theta_c}\right)\left(\frac{2k}{m\pi}\right)^{\frac{1}{2}}\left(\theta_e p_{sat}\left(T_l\right)\sqrt{T_l} - \theta_c p_v\sqrt{T_v}\right), \tag{4.30}$$

which is identical to the to the CE energy flux (4.26), and agrees with the form presented by Barrett and Clement [17].

We now consider the momentum flux. Barrett and Clement [17] claim that by definition the momentum flux must be constant, and equal to the pressure in the direction of the flux, i.e. the vapor pressure p_v. We see from the momentum balance, Eqn. (2.10), that they are correct in assuming that the momentum flux,

$$M = \rho v_i v_k + p_{ik} = const \tag{4.31}$$

for steady state without gravity effects. If we assume the isotropic vapor pressure, and neglect shear forces, as before $p_{ik} = p_v\delta_{ik}$. For one-dimensional flow the momentum flux reduces to

$$M = \rho v_z^2 + p_v = const, \tag{4.32}$$

which becomes p_v for small v_z, as Barrett and Clement point out [17]. We emphasize that the momentum flux is only equal to p_v under the assumptions of small v_z, and isotropic vapor pressure without shear forces, not in the general case as Barrett and Clement claim [17].

The one-dimensional momentum flux is given by

$$M = \iiint_{-\infty}^{\infty} mc_z^2 f d\underline{c}. \tag{4.33}$$

At the interface it must include the momentum flux due to the reflected molecule streams; for

specular reflection it is

$$\begin{aligned} M_{int} &= \iiint\limits_{c_z>0} mc_z^2 f_l\left(p_{sat}\left(T_l\right),T_l\right) d\underline{c} + \iiint\limits_{c_z<0} mc_z^2 f_v\left(p_v,T_v\right) d\underline{c} + \\ &\quad .(1-\theta_e)\iiint\limits_{c_z<0} mc_z^2 f_l\left(p_{sat}\left(T_l\right),T_l\right) d\underline{c} + (1-\theta_c)\iiint\limits_{c_z>0} mc_z^2 f_v\left(p_v,T_v\right) d\underline{c} \end{aligned} \quad (4.34)$$

We now calculate the momentum flux at the interface for specular reflection by integrating Eqn. (4.34),

$$M_{int} = p_{sat}\left(T_l\right)\left(1-\frac{\theta_e}{2}\right) + p_v\left(1-4v_z\sqrt{\frac{m}{2\pi kT_v}}\right)\left(1-\frac{\theta_c}{2}\right). \quad (4.35)$$

Substituting in the bulk energy flux (4.29), the interface momentum flux becomes

$$M_{int} = p_{sat}\left(T_l\right)\left(1-\frac{\theta_e}{2}\right) + \left(p_v-\frac{8}{5}Q\sqrt{\frac{m}{2\pi kT_v}}\right)\left(1-\frac{\theta_c}{2}\right). \quad (4.36)$$

From Eqn. (4.33) the momentum flux in the bulk vapor using the Schrage distribution (4.12) is

$$M_{bulk} = p_v. \quad (4.37)$$

We note that both the interface and bulk kinetic theory moment fluxes, Eqns. (4.36) and (4.37), assume small v_z. The bulk momentum flux (4.37) agrees with Eqn. (4.32) for small v_z, thus in the bulk vapor the pressure must be isotropic, and without shear forces. If this is also true at the interface, then $M_{int} = M_{bulk}$. However this would imply from Eqns. (4.36) and (4.37) that

$$p_v = p_{sat}\left(T_l\right)\left(1-\frac{\theta_e}{2}\right) + \left(p_v-\frac{8}{5}Q\sqrt{\frac{m}{2\pi kT_v}}\right)\left(1-\frac{\theta_c}{2}\right), \quad (4.38)$$

which does not agree with the energy flux expression (4.30), thus we conclude that the non-isotropic pressure, and shear forces make up the difference between M_{int} and M_{bulk}. This however does not imply that momentum is not conserved.

We conclude that the Schrage distribution (4.12) does not violate the conservation of momentum, nor the conservation of energy. Barrett and Clement [17] are correct in saying the bulk and interface energy and momentum flux expressions are not the same, however they miss the

substitution of the bulk energy flux into the interface flux, and the interface non-isotropic and shear force pressure effects.

4.5 Specular and Diffuse Reflection

In the previous section we made the assumption that all reflected vapor molecules are reflected specularly. We now allow for the possibility of diffuse reflection, that is the vapor molecules interact thermally with the interface, and leave with the interface distribution, and temperature. The accommodation coefficient γ differentiates between specular and diffuse reflection. γ is the ratio between the number of specularly reflected molecules, and the total number of reflected molecules. $\gamma = 1$ designates purely specular reflection, and $\gamma = 0$ purely diffuse reflection. Figure 4.2 shows the distributions with the accommodation coefficient. The diffusely reflected molecule distribution is the same as the surface distribution, namely the Maxwellian (4.6). It is a function of the liquid surface temperature T_l and equivalent pressure $p*$. This pressure is calculated based on the conservation of mass (4.1) to insure the number of molecules that hit the interface to be reflected is equal to the number reflected.

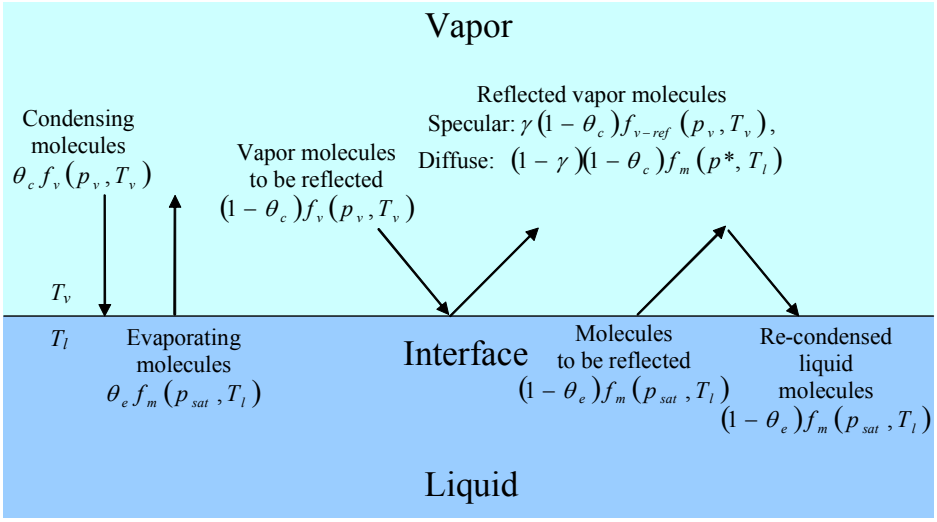

Figure 4.2: Specular and diffuse reflection distributions

The mass flux expressions, Eqns. (4.22) , and (4.25) which we developed for specular reflection

are still valid for diffuse reflection, since the reflected molecules do not contribute to the mass flux.

The energy flux expression must now account for the reflected molecules, since the net energy flux of the diffusely reflected molecules and their incident molecules is no longer zero, as was the case for purely specular reflection. We assume the molecules described by $(1-\theta_e)\, f_{m-ref}\left(p_{sat}\left(T_l\right), T_l\right)$ in Figure 4.2 which leave the liquid and bounce back, do so specularly, and thus do not contribute to the energy flux. They likely would not travel far from the surface, and not collide with many other molecules, thus allowing them to maintain their energy, and distribution. We sum each molecule stream's contribution to the energy flux

$$\begin{aligned} Q &= \theta_e \iiint\limits_{c_z>0} \frac{m}{2} c_z c^2 f_m\left(p_{sat}\left(T_l\right), T_l\right) d\underline{c} + \theta_c \iiint\limits_{c_z<0} \frac{m}{2} c_z c^2 f_v\left(p_v, T_v\right) d\underline{c} \\ &\quad + (1-\theta_c) \iiint\limits_{c_z<0} \frac{m}{2} c_z c^2 f_v\left(p_v, T_v\right) d\underline{c} + \gamma\,(1-\theta_c) \iiint\limits_{c_z>0} \frac{m}{2} c_z c^2 f_{v-ref}\left(p_v, T_v\right) d\underline{c} \\ &\quad + (1-\gamma)\,(1-\theta_c) \iiint\limits_{c_z>0} \frac{m}{2} c_z c^2 f_m\left(p*, T_l\right) d\underline{c}. \end{aligned} \tag{4.39}$$

Each integral in Eqn. (4.39) represents a molecule flow in Figure 4.2. The first term is due to evaporating molecules, the second is due to condensing molecules, the third is due to incident molecules that are reflected at the interface, the fourth is due to specularly reflected molecules, and the fifth is due to diffusely reflected molecules. The second and third terms can be combined,

$$\begin{aligned} Q &= \theta_e \iiint\limits_{c_z>0} \frac{m}{2} c_z c^2 f_m\left[p_{sat}\left(T_l\right), T_l\right] d\underline{c} + \iiint\limits_{c_z<0} \frac{m}{2} c_z c^2 f_v\left(p_v, T_v\right) d\underline{c} \\ &\quad + \gamma\,(1-\theta_c) \iiint\limits_{c_z>0} \frac{m}{2} c_z c^2 f_{v-ref}\left(p_v, T_v\right) d\underline{c} \\ &\quad + (1-\gamma)\,(1-\theta_c) \iiint\limits_{c_z>0} \frac{m}{2} c_z c^2 f_m\left(p*, T_l\right) d\underline{c}. \end{aligned} \tag{4.40}$$

We need to develop an expression for $p*$. Applying the conservation of mass (4.1) for the

reflected molecules yields

$$(1-\theta_c)\iiint\limits_{c_z<0} c_z f_v\left(p_v,T_v\right)d\underline{c} + \gamma\left(1-\theta_c\right)\iiint\limits_{c_z>0} c_z f_{v-ref}\left(p_v,T_v\right)d\underline{c}$$
$$+\left(1-\gamma\right)\left(1-\theta_c\right)\iiint\limits_{c_z>0} c_z f_m\left(p*,T_l\right)d\underline{c} = 0. \tag{4.41}$$

The first term represents all the incident vapor molecules that are reflected, the second those which are reflected specularly, and the third the diffusely reflected stream.

4.5.1 Maxwell Distribution, $v_z = 0$

As before we set $f_v = f_m$, and assume the net vapor velocity $v_z = 0$. As mentioned earlier, the distribution of the specularly reflected molecules is identical to the incident distribution, except that the signs of the terms containing c_z are reversed. Since the Maxwellian (4.6) has only a C^2 velocity term, reversing the sign of the velocity for the reflected distribution will have no effect, thus the specularly reflected distribution will be $f_{v-ref}\left(p_v,T_v\right) = f_m\left(p_v,T_v\right)$.

Eqn. (4.41) becomes

$$-p_v\sqrt{\frac{m}{2\pi kT_v}} + \gamma p_v\sqrt{\frac{m}{2\pi kT_v}} + \left(1-\gamma\right)p*\sqrt{\frac{m}{2\pi kT_l}} = 0. \tag{4.42}$$

We solve for $p*$ and find

$$p* = p_v\sqrt{\frac{T_l}{T_v}}. \tag{4.43}$$

Integrating Eqn. (4.40) and substituting in for $p*$, yields the energy flux for specular and diffuse reflection,

$$Q = \left(\frac{2k}{m\pi}\right)^{\frac{1}{2}}\left(\theta_e p_{sat}\left(T_l\right)\sqrt{T_l} - \theta_c p_v\frac{T_l}{\sqrt{T_v}} + \frac{p_v}{\sqrt{T_v}}\left(T_l-T_v\right)\left[1-\gamma\left(1-\theta_c\right)\right]\right), \tag{4.44}$$

and from Eqn. (4.22) the mass flux is still

$$j = \left(\frac{m}{2\pi k}\right)^{\frac{1}{2}}\left(\frac{\theta_e p_{sat}\left(T_l\right)}{\sqrt{T_l}} - \frac{\theta_c p_v}{\sqrt{T_v}}\right). \tag{4.45}$$

We see that Eqn. (4.44) reduces to Eqn. (4.23) for purely specular reflection, $\gamma = 1$. As well for $\theta_c = \theta_e = 1$, it reduces to the HK energy flux (4.9). Finally we see that it satisfies equilibrium for any values of γ, $j = 0$ and $Q = 0$, for $p_v = p_{sat}(T)$, $T_l = T_v = T$, and $\theta_e = \theta_c$.

4.5.2 Chapman-Enskog with Net Vapor Velocity

The reflected CE distribution with net vapor velocity is

$$f_{ce-v-ref} = f_{m-v-ref}\left(1 + \frac{2}{5}\frac{\kappa}{p}\frac{m}{k}c_z\left(\frac{mc^2}{2kT^2} - \frac{5}{2T}\right)\frac{dT}{dz}\right), \tag{4.46}$$

where

$$f_{m-v-ref} = \frac{p}{kT}\left(\frac{m}{2\pi kT}\right)^{\frac{3}{2}}\exp\left(-\frac{m}{2kT}c^2\right)\left(1 - \frac{m}{kT}c_z v_z\right). \tag{4.47}$$

Note the signs of the terms containing c_z have changed from the incident distributions Eqns. (4.12) and (4.13).

The conservation of mass (4.41) yields

$$p* = p_v\sqrt{\frac{T_l}{T_v}} - j\sqrt{\frac{\pi k T_l}{2m}}. \tag{4.48}$$

From Eqns. (4.40), and (4.48) the CE energy flux with specular and diffuse reflection reads

$$\begin{aligned} Q \;=\; & \frac{2}{1+\gamma(1-\theta_c)}\left(\frac{2k}{m\pi}\right)^{\frac{1}{2}} \\ & \left(\theta_e p_{sat}(T_l)\sqrt{T_l} - \theta_c p_v\frac{T_l}{\sqrt{T_v}} + [1-\gamma(1-\theta_c)]\frac{p_v}{\sqrt{T_v}}(T_l - T_v) - T_l(1-\gamma)(1-\theta_c)\,j\sqrt{\frac{\pi k}{2m}}\right). \end{aligned} \tag{4.49}$$

From Eqn. (4.25) the corresponding mass flux is

$$j = \left(\frac{2}{2-\theta_c}\right)\left(\frac{m}{2\pi k}\right)^{\frac{1}{2}}\left(\frac{\theta_e p_{sat}(T_l)}{\sqrt{T_l}} - \frac{\theta_c p_v}{\sqrt{T_v}}\right). \tag{4.50}$$

As expected Eqn. (4.49) reduces to Eqn. (4.26) for purely specular reflection, $\gamma = 1$, and Eqn. (4.20) for $\theta_c = \theta_e = 1$. Again we see the equilibrium conditions are satisfied for any value of γ, $Q = 0$ and $j = 0$, for $p_v = p_{sat}(T)$, $T_l = T_v = T$, and $\theta_e = \theta_c$.

4.6 Velocity and Temperature Dependant Condensation and Evaporation Coefficients

We mentioned in the introduction that MD simulations have suggested the condensation coefficient is dependant on the energy of the incident molecules, and the interface surface temperature [43], [44], [45], [46], [47]. An incident molecule with high energy can penetrate more deeply into the liquid phase, resulting in more collisions with liquid molecules increasing the likelihood of condensation [44]. Increased surface temperature increases the energy and velocities of the surface molecules, increasing the likelihood of incident molecules having collisions at the surface. This reduces incident molecule penetration, reducing the condensation coefficient. To accommodate this behavior, it is suggested that the condensation coefficient is of the form [44]

$$\theta_c = \psi \left[1 - \omega \exp\left(\frac{-mc^2}{2kT_l} \right) \right], \tag{4.51}$$

where ψ, and ω are constants.

Since we know the condensation coefficient must be between 0 and 1, this must also be true for Eqn. (4.51). If $\underline{c}^2 \to \infty$, $\theta_c = \psi$ indicating that $0 \leq \psi \leq 1$. For $\underline{c}^2 = 0$, $\theta_c = \psi\,(1-\omega)$; this forces $\omega \leq 1$, and also implies $\omega \geq 1 - \frac{1}{\psi}$. Thus ω is restricted to

$$1 - \frac{1}{\psi} \leq \omega \leq 1. \tag{4.52}$$

This suggests the possibility of a negative ω. We recall that the probability of a molecule condensing increases with its energy $m\underline{c}^2$, and decreases with higher surface temperature T_l. For θ_c (4.51) to follow this trend, ω must be positive, thus its range is

$$0 \leq \omega \leq 1. \tag{4.53}$$

Tsuruta et al. [44] report from MD simulations for argon that ψ, and ω vary from $0.971 - 0.685$, and $0.086 - 0.554$, respectively.

We know that $\theta_e = \theta_c$ must be true in equilibrium, and that the liquid is locally in equilibrium. If we assume that the individual vapor molecules hitting the interface, described by Eqn. (4.51),

are also locally in equilibrium, then we can set $\theta_e = \theta_c$. The velocity dependant condensation coefficient (4.51) is then inserted into the mass and energy flux integrals, Eqns. (4.3), and (4.4), yielding

$$\begin{aligned} j &= \iiint\limits_{c_z>0} \psi \left(1 - \omega \exp\left(\frac{-mc^2}{2kT_l}\right)\right) mc_z f_m \left[p_{sat}\left(T_l\right), T_l\right] d\underline{c} \\ &\quad + \iiint\limits_{c_z<0} \psi \left(1 - \omega \exp\left(\frac{-mc^2}{2kT_l}\right)\right) mc_z f_v \left(p_v, T_v\right) d\underline{c}, \end{aligned} \tag{4.54}$$

for purely specular reflection

$$\begin{aligned} Q &= \iiint\limits_{c_z>0} \psi \left(1 - \omega \exp\left(\frac{-mc^2}{2kT_l}\right)\right) \frac{m}{2} c_z c^2 f_m \left[p_{sat}\left(T_l\right), T_l\right] d\underline{c} \\ &\quad + \iiint\limits_{c_z<0} \psi \left(1 - \omega \exp\left(\frac{-mc^2}{2kT_l}\right)\right) \frac{m}{2} c_z c^2 f_v \left(p_v, T_v\right) d\underline{c}, \end{aligned} \tag{4.55}$$

and for specular and diffuse reflection

$$\begin{aligned} Q &= \iiint\limits_{c_z>0} \psi \left(1 - \omega \exp\left(\frac{-mc^2}{2kT_l}\right)\right) \frac{m}{2} c_z c^2 f_m \left[p_{sat}\left(T_l\right), T_l\right] d\underline{c} + \iiint\limits_{c_z<0} \frac{m}{2} c_z \underline{c}^2 f_v \left(p_v, T_v\right) d\underline{c} \\ &\quad + \gamma \iiint\limits_{c_z>0} \left(1 - \psi \left\{1 - \omega \exp\left(\frac{-mc^2}{2kT_l}\right)\right\}\right) \frac{m}{2} c_z c^2 f_{v-ref}\left(p_v, T_v\right) d\underline{c} \\ &\quad + (1-\gamma) \iiint\limits_{c_z>0} \left(1 - \psi \left\{1 - \omega \exp\left(\frac{-mc^2}{2kT_l}\right)\right\}\right) \frac{m}{2} c_z c^2 f_m \left(p*, T_l\right) d\underline{c}. \end{aligned} \tag{4.56}$$

The conservation of mass (4.1) for the reflected molecules becomes

$$\begin{aligned} &\iiint\limits_{c_z<0} \left(1 - \psi \left\{1 - \omega \exp\left(\frac{-mc^2}{2kT_l}\right)\right\}\right) c_z f_v \left(p_v, T_v\right) d\underline{c} \\ &+ \gamma \iiint\limits_{c_z>0} \left(1 - \psi \left\{1 - \omega \exp\left(\frac{-mc^2}{2kT_l}\right)\right\}\right) c_z f_{v-ref}\left(p_v, T_v\right) d\underline{c} \\ &+ (1-\gamma) \iiint\limits_{c_z>0} \left(1 - \psi \left\{1 - \omega \exp\left(\frac{-mc^2}{2kT_l}\right)\right\}\right) c_z f_m \left(p*, T_l\right) d\underline{c} = 0. \end{aligned} \tag{4.57}$$

4.6.1 Maxwell Distribution-Specular Reflection, $v_z = 0$

We integrate Eqn. (4.54) for $f_v = f_m$, $f_{v-ref}(p_v, T_v) = f_m(p_v, T_v)$, and $v_z = 0$, and find

$$j = \left(\frac{m}{2\pi k}\right)^{\frac{1}{2}} \left(\psi\left(1 - \frac{\omega}{2}\right)\frac{p_{sat}(T_l)}{\sqrt{T_l}} - \psi\left(1 - \frac{T_l\omega}{T_l + T_v}\right)\frac{p_v}{\sqrt{T_v}}\right). \tag{4.58}$$

Eqn. (4.58) differs from the HK mass flux (4.8) by a temperature and coefficient dependant factor of

$$\eta(T_l, T) = \psi\left(1 - \frac{T_l\omega}{T_l + T}\right). \tag{4.59}$$

We incorporate $\eta(T_l, T)$ into Eqn. (4.58),

$$j = \left(\frac{m}{2\pi k}\right)^{\frac{1}{2}} \left(\eta(T_l, T_l)\frac{p_{sat}(T_l)}{\sqrt{T_l}} - \eta(T_l, T_v)\frac{p_v}{\sqrt{T_v}}\right). \tag{4.60}$$

For $T = T_l$, Eqn. (4.59) reduces to

$$\eta(T_l, T_l) = \psi\left(1 - \frac{\omega}{2}\right), \tag{4.61}$$

which is the factor in front of the first term in Eqn. (4.58), and is exactly what Nagayama et al. [47] give as the condensation coefficient.

We recall from Eqn. (4.51), that $\theta_c = 1$, for $\psi = 1$, and $\omega = 0$. Since we have assumed that $\theta_e = \theta_c$, we see Eqn. (4.60) reduces to the HK mass flux (4.8) for $\psi = 1$, and $\omega = 0$.

If we compare Eqn. (4.60) to Eqn. (4.22), we see $\eta(T_l, T)$ is a temperature dependant condensation and evaporation coefficient.

Integrating Eqn. (4.55) yields the energy flux for purely specular reflection

$$Q = \left(\frac{2k}{m\pi}\right)^{\frac{1}{2}} \left(\psi\left(1 - \frac{3\omega}{8}\right)p_{sat}(T_l)\sqrt{T_l} - \psi\left(1 - \frac{T_l(2T_l + T_v)\omega}{2(T_l + T_v)^2}\right)p_v\sqrt{T_v}\right). \tag{4.62}$$

Comparing Eqn. (4.62) with the HK energy flux, Eqns. (4.9) and (4.23) gives another temper-

ature dependant condensation, and evaporation coefficient

$$\varphi_s\left(T_l,T\right)=\psi\left(1-\frac{T_l\left(2T_l+T\right)\omega}{2\left(T_l+T\right)^2}\right), \tag{4.63}$$

different from that of the mass flux (4.59). Eqn. (4.62) with $\varphi_s\left(T_l,T\right)$ reads

$$Q=\left(\frac{2k}{m\pi}\right)^{\frac{1}{2}}\left(\varphi_s\left(T_l,T_l\right)p_{sat}\left(T_l\right)\sqrt{T_l}-\varphi_s\left(T_l,T_v\right)p_v\sqrt{T_v}\right). \tag{4.64}$$

Again we see for $\psi=1$, and $\omega=0$, Eqn. (4.64) reduces to the HK energy flux (4.9).

Eqns. (4.60),and (4.64) satisfy the equilibrium conditions, $p_v=p_{sat}\left(T\right)$, $T_l=T_v=T$,since they reduce to $j=0$, and $Q=0$. We also note that $\eta\left(T_l,T\right)$ and $\varphi_s\left(T_l,T\right)$ satisfy the equilibrium condition of $\theta_e=\theta_c$.

4.6.2 Maxwell Distribution-Specular and Diffuse Reflection, $v_z=0$

The mass flux expression is the same as for purely specular reflection, Eqn. (4.60). For the energy flux we initially consider purely diffuse reflection. From Eqns. (4.56), and (4.57) with $\gamma=0$ we find a temperature dependant evaporation and condensation coefficient of

$$\varphi_d\left(T_l,T\right)=\left(\psi\left(1-\frac{3\omega}{8}\right)-1\right)\frac{T_l}{T}\frac{2\left(1-\psi+\psi\omega\frac{T_l}{T+T_l}\right)}{2+\psi\left(\omega-2\right)}+1. \tag{4.65}$$

We write a general energy flux evaporation and condensation coefficient for both specular, and diffuse reflection by combining Eqns. (4.63), and (4.65) using the accommodation coefficient,

$$\varphi\left(T_l,T\right)=\gamma\varphi_s\left(T_l,T\right)+\left(1-\gamma\right)\varphi_d\left(T_l,T\right). \tag{4.66}$$

The energy flux with $\varphi\left(T_l,T\right)$ reads

$$Q=\left(\frac{2k}{m\pi}\right)^{\frac{1}{2}}\left(\varphi\left(T_l,T_l\right)p_{sat}\left(T_l\right)\sqrt{T_l}-\varphi\left(T_l,T_v\right)p_v\sqrt{T_v}\right). \tag{4.67}$$

Again, Eqn. (4.67) satisfies the equilibrium conditions, $Q=0$, for $p_v=p_{sat}\left(T\right)$, and $T_l=T_v=$

T. For $\psi = 1$, and $\omega = 0$ it reduces to the HK energy flux Eqn. (4.9).

4.6.3 Chapman-Enskog with Net Vapor Velocity

For $f_v = f_{ce-v}$, and $f_{v-ref}\left(p_v, T_v\right) = f_{ce-ref}\left(p_v, T_v\right)$, the mass flux from Eqns. (4.54), and 4.59 reads

$$\begin{aligned} j &= \left(\frac{m}{2\pi k}\right)^{\frac{1}{2}} \left(\eta\left(T_l, T_l\right) \frac{p_{sat}\left(T_l\right)}{\sqrt{T_l}} - \eta\left(T_l, T_v\right) \frac{p_v}{\sqrt{T_v}}\right) \\ &\quad + \frac{m}{2T_v k} \kappa_v \frac{\partial T_v}{\partial z} \psi\omega \left(\frac{T_l}{T_l + T_v}\right)^{\frac{3}{2}} \left(\frac{T_l + \frac{2}{5}T_v}{T_l + T_v} - 1\right) \\ &\quad + \frac{j}{2}\psi \left(1 - \left(\frac{T_l}{T_l + T_v}\right)^{\frac{3}{2}} \omega\right). \end{aligned} \tag{4.68}$$

The energy flux for purely specular reflection from Eqns. (4.55), and (4.63) is

$$\begin{aligned} Q &= \left(\frac{2k}{m\pi}\right)^{\frac{1}{2}} \left(\varphi_s\left(T_l, T_l\right) p_{sat}\left(T_l\right) \sqrt{T_l} - \varphi_s\left(T_l, T_v\right) p_v \sqrt{T_v}\right) \\ &\quad - \kappa_v \frac{\partial T_v}{\partial z} \psi \left(\omega \frac{T_l^{\frac{3}{2}}}{\left(T_l + T_v\right)^{\frac{5}{2}}} \left(\frac{5}{4}\left(T_l + \frac{2}{5}T_v\right) - \frac{35T_l^2 + 28T_l T_v + 8T_v^2}{20\left(T_l + T_v\right)}\right) + \frac{1}{2}\right) \\ &\quad + \psi \left(1 - \frac{T_l^{\frac{3}{2}}}{\left(T_l + T_v\right)^{\frac{5}{2}}} \left(T_l + \frac{2}{5}T_v\right)\omega\right) \frac{j c_p T_v}{2}. \end{aligned} \tag{4.69}$$

We recall the definition of the energy flux (2.24), $Q = jh_v + q_v$. For kinetic theory the vapor enthalpy is $h_v = c_p T_v$, where $c_p = \frac{5}{2}\frac{k}{m}$. From Fourier's law (2.51), the conductive heat flux is $q_v = -\kappa_v \frac{\partial T_v}{\partial z}$. Solving the energy flux for the temperature gradient yields

$$\kappa_v \frac{\partial T_v}{\partial z} = j c_p T_v - Q. \tag{4.70}$$

With this definition of energy flux in mind, we see that the mass flux (4.68), and energy flux (4.69) are linked, since they each contain mass, and energy flux terms. We seek to present

them in a more explicit matrix form,

$$\begin{bmatrix} j \\ Q \end{bmatrix} = \Re^{-1} \cdot \aleph. \tag{4.71}$$

The matrix $\Re$ reads

$$\begin{aligned}
\Re_{11} &= 1 - \frac{5\psi\omega}{4}\left(\frac{T_l}{T_l+T_v}\right)^{\frac{3}{2}}\left(\frac{T_l+\frac{2}{5}T_v}{T_l+T_v}-1\right) - \frac{\psi}{2}\left(1-\left(\frac{T_l}{T_l+T_v}\right)^{\frac{3}{2}}\omega\right) \\
\Re_{12} &= \psi\omega\frac{m}{2T_vk}\left(\frac{T_l}{T_l+T_v}\right)^{\frac{3}{2}}\left(\frac{T_l+\frac{2}{5}T_v}{T_l+T_v}-1\right) \\
\Re_{21} &= \frac{c_pT_v\psi}{2}\omega\frac{T_l^{\frac{3}{2}}}{(T_l+T_v)^{\frac{5}{2}}}\left(\frac{7}{2}\left(T_l+\frac{2}{5}T_v\right)-\frac{35T_l^2+28T_lT_v+8T_v^2}{10\left(T_l+T_v\right)}\right) \\
\Re_{22} &= 1-\psi\left(\omega\frac{T_l^{\frac{3}{2}}}{(T_l+T_v)^{\frac{5}{2}}}\left(\frac{5}{4}\left(T_l+\frac{2}{5}T_v\right)-\frac{35T_l^2+28T_lT_v+8T_v^2}{20\left(T_l+T_v\right)}\right)+\frac{1}{2}\right),
\end{aligned} \tag{4.72}$$

and the vector $\aleph$ is given as

$$\begin{aligned}
\aleph_1 &= \left(\frac{m}{2\pi k}\right)^{\frac{1}{2}}\left(\eta\left(T_l,T_l\right)\frac{p_{sat}\left(T_l\right)}{\sqrt{T_l}}-\eta\left(T_l,T_v\right)\frac{p_v}{\sqrt{T_v}}\right) \\
\aleph_2 &= \left(\frac{2k}{m\pi}\right)^{\frac{1}{2}}\left(\varphi_s\left(T_l,T_l\right)p_{sat}\left(T_l\right)\sqrt{T_l}-\varphi_s\left(T_l,T_v\right)p_v\sqrt{T_v}\right).
\end{aligned} \tag{4.73}$$

We see that vector $\aleph$ (4.73) gives exactly the mass flux, and specular energy flux found with the Maxwellian, Eqns. (4.60), and (4.64). We conclude that for the Maxwellian, the matrix $\Re$ is just the unit matrix.

As we would expect, Eqn. (4.71) reduces to the CE relations, Eqns. (4.16), and (4.20) for $\psi = 1$, and $\omega = 0$. Also it yields $j = 0$, and $Q = 0$, for the equilibrium conditions $p_v = p_{sat}\left(T\right)$, and $T_l = T_v = T$.

We create the corresponding matrix, and vector for the more general specular, and diffuse

reflection case. Eqns. (4.54), (4.56), (4.57), (4.59), (4.63), (4.65), and (4.66) result in

$$\begin{aligned}
\Re_{11} &= 1-\frac{5\psi\omega}{4}\left(\frac{T_l}{T_l+T_v}\right)^{\frac{3}{2}}\left(\frac{T_l+\frac{2}{5}T_v}{T_l+T_v}-1\right)-\frac{\psi}{2}\left(1-\left(\frac{T_l}{T_l+T_v}\right)^{\frac{3}{2}}\omega\right)\\
\Re_{12} &= \psi\omega\frac{m}{2T_vk}\left(\frac{T_l}{T_l+T_v}\right)^{\frac{3}{2}}\left(\frac{T_l+\frac{2}{5}T_v}{T_l+T_v}-1\right)\\
\Re_{21} &= \frac{\gamma c_pT_v\psi}{2}\omega\frac{T_l^{\frac{3}{2}}}{(T_l+T_v)^{\frac{5}{2}}}\left\{\frac{7}{2}\left(T_l+\frac{2}{5}T_v\right)-\frac{35T_l^2+28T_lT_v+8T_v^2}{10\left(T_l+T_v\right)}\right\}\\
&\quad -(1-\gamma)\left\{1-\psi\left(1-\frac{3}{8}\omega\right)\right\}\frac{2k}{m}\left(\frac{1}{2+\psi\left(\omega-2\right)}\right)\\
&\quad \left(T_l\left(\psi-1\right)-\frac{T_l^{\frac{5}{2}}\psi\omega}{(T_l+T_v)^{\frac{3}{2}}}-\frac{\frac{3}{2}T_l^{\frac{5}{2}}T_v\psi\omega}{(T_l+T_v)^{\frac{5}{2}}}\right)\\
\Re_{22} &= \frac{1}{2}-\gamma\psi\left(\omega\frac{T_l^{\frac{3}{2}}}{(T_l+T_v)^{\frac{5}{2}}}\left\{\frac{5}{4}\left(T_l+\frac{2}{5}T_v\right)-\frac{35T_l^2+28T_lT_v+8T_v^2}{20\left(T_l+T_v\right)}\right\}+\frac{1}{2}\right)\\
&\quad +\frac{\gamma}{2}-(1-\gamma)\left\{1-\psi\left(1-\frac{3\omega}{8}\right)\right\}\frac{6}{5}\frac{T_l^{\frac{5}{2}}\psi\omega}{(T_l+T_v)^{\frac{5}{2}}\left(2+\psi\left(\omega-2\right)\right)}
\end{aligned}\tag{4.74}$$

and vector

$$\begin{aligned}
\aleph_1 &= \left(\frac{m}{2\pi k}\right)^{\frac{1}{2}}\left(\eta\left(T_l,T_l\right)\frac{p_{sat}\left(T_l\right)}{\sqrt{T_l}}-\eta\left(T_l,T_v\right)\frac{p_v}{\sqrt{T_v}}\right)\\
\aleph_2 &= \left(\frac{2k}{m\pi}\right)^{\frac{1}{2}}\left(\varphi\left(T_l,T_l\right)p_{sat}\left(T_l\right)\sqrt{T_l}-\varphi\left(T_l,T_v\right)p_v\sqrt{T_v}\right).
\end{aligned}\tag{4.75}$$

We see that vector $\aleph$ (4.75) gives exactly the mass flux, and specular and diffuse energy flux found with the Maxwellian, Eqns. (4.60), and (4.67). We again conclude that for the Maxwellian, the matrix $\Re$ is the unit matrix. As with the specular case, Eqns. (4.71), (4.74), and (4.75) can be considered to be in the same form as the phenomenological force-flux expressions (1.25).

Again we comment that for $\psi = 1$, and $\omega = 0$ Eqns. (4.71), (4.74), and (4.75) reduce to the CE relations, Eqns. (4.16), and (4.20). For equilibrium, $p_v = p_{sat}\left(T\right)$ and $T_l = T_v = T$, they reduce to $j = 0$ and $Q = 0$

4.7 Kinetic Theory Reference Adjustment

The kinetic theory vapor enthalpy used in Eqn. (4.70) is different from the constant specific heat vapor enthalpy (2.37), since both are not based on the same reference. To use the kinetic theory energy flux expression in conjunction with the temperature distribution, and entropy production expressions developed with the constant specific heat vapor enthalpy, it is necessary to adjust the kinetic theory reference point. A reference constant r_f is included with the molecule kinetic energy in the energy flux integral,

$$Q = \iiint_{-\infty}^{\infty} mc_z \left(\frac{c^2}{2} + r_f \right) f d\underline{c}. \tag{4.76}$$

Modelling the bulk vapor with the first order CE distribution (4.13), and integrating over full space, yields

$$Q = -\kappa_v \frac{dT_v}{dz} + j \left(\frac{5}{2} \frac{kT_v}{m} + r_f \right). \tag{4.77}$$

Using the monatomic gas specific heat, $c_p = \frac{5}{2}\frac{k}{m}$ the energy flux in the bulk vapor becomes

$$Q = -\kappa_v \frac{dT_v}{dz} + j \left(c_p T_v + r_f \right). \tag{4.78}$$

The first term in Eqn. (4.78) is the conductive energy flux, and the second term is the convective energy flux. From Eqns. (4.78), (2.24), and (2.51), it follows

$$j \left(c_p \left(T_v - T_o \right) + \Delta h_o \right) - \kappa_v \frac{dT_v}{dz} = -\kappa_v \frac{dT_v}{dz} + j \left(c_p + r_f \right), \tag{4.79}$$

which implies

$$r_f = \Delta h_o - c_p T_o. \tag{4.80}$$

Re-performing the energy flux integral, Eqn. (4.4), with the addition of r_f for the CE vapor distribution, the CE energy flux with the adjusted reference is

$$Q = 2 \left(\frac{2k}{m\pi} \right)^{\frac{1}{2}} \left(p_{sat} \left(T_l \right) \sqrt{T_l} - p_v \sqrt{T_v} \right) + j r_f. \tag{4.81}$$

Eqn. (4.81) compared with the CE energy flux without reference adjustment, Eqn. (4.20), gives the energy flux reference correction term jr_f. This correction can be applied to any of the kinetic theory energy flux expressions. A general from of the corrected kinetic theory energy flux is then

$$Q = Q_{kt} + jr_f, \tag{4.82}$$

where Q_{kt} is the kinetic theory energy flux before reference correction.

Chapter 5

Model Solution Generation Methodology

We now have expressions for the liquid and vapor temperature profiles, the surface pressure, and the interface mass and energy fluxes. We describe our procedure for solving this system of equations.

5.1 Constants, Prescribed Parameters, Equations to Solve

We choose a common thermodynamic reference temperature of $T_o = 25\,^{\circ}\mathrm{C}$. The reference pressure is chosen as the saturation pressure of T_o, $p_o = 3.169\,\mathrm{kPa}$ [56].

The material constants are then chosen relative to the reference point, see Table 5.1 [56]. They are all specific to water, except the vapor specific heat which is the general expression for a monatomic gas. The rationale for this has been discussed in Section 2.2. recall that $\frac{k}{m} = R$.

Enthalpy of Vaporization	Δh_o	$2.445 \times 10^6 \frac{\mathrm{J}}{\mathrm{kg}}$
Monatomic Gas Specific Heat	c_p	$\frac{5}{2}\frac{k}{m}$
Liquid Specific Heat	c_l	$4180 \frac{\mathrm{J}}{\mathrm{kg\,K}}$
Vapor Thermal Conductivity	κ_v	$1.4 \times 10^{-2} \frac{\mathrm{W}}{\mathrm{m\,K}}$
Liquid Thermal Conductivity	κ_l	$55 \times 10^{-2} \frac{\mathrm{W}}{\mathrm{m\,K}}$
Molecular Mass	m	$0.018 \frac{\mathrm{kg}}{\mathrm{mol}}$
Ideal Gas Constant for Water Vapor	R	$0.462 \frac{\mathrm{kJ}}{\mathrm{kg\,K}}$

Table 5.1: Material constants

We prescribe the temperature boundaries, and vapor pressure, see Table 5.2. These parameters describe the state of the system, see Figure 5.1.

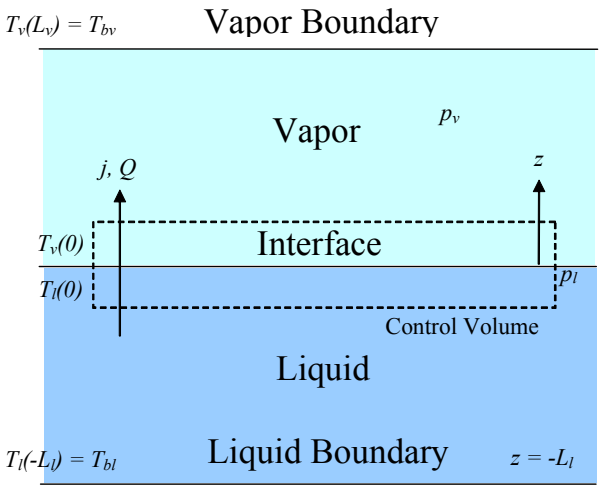

Figure 5.1: Model parameters

Their values can be found from the measurements of Ward, Fang, and Stanga [2], [3], [4], and then used in conjunction with the model to predict the interface conditions and temperature profiles.

Liquid boundary temperature	T_{bl}
Vapor boundary temperature	T_{bv}
Liquid depth	L_l
Vapor depth	L_v
Vapor pressure	p_v

Table 5.2: Prescribed parameters

We have expressions for the liquid and vapor interface temperatures T_l, and T_v, Eqns. (2.59), and (2.60) at $z = 0$, in terms of the mass and energy fluxes j, and Q. We have irreversible thermodynamics, SRT, and kinetic theory expressions for j and Q in terms of T_l and T_v, and the saturation pressure $p_{sat}(T_l)$ (2.49). This results in four equations, the two temperature profiles, and the mass and energy flux equations, with four unknowns, T_l, T_v, j, and Q.

5.2 Equation Solving Software and Functions

The four equations are solved simultaneously using the "FindRoot" function in Mathematica 4.1©. The function uses Newton's method with an initial guess to converge to an accuracy of six digits [58]. We make initial guesses for the two interface temperatures and fluxes, based on trial and error, and knowledge of the equilibrium position. If these guesses are sufficiently close to the solution, then Newton's method will converge to a solution. There is no guarantee that there is only one solution. It is possible with different initial guesses, that an alternate solution might be found. We discount the possibility of multiple solutions for our system of equations for two reasons: the solutions we find appear to be realistic agreeing with measured data, and variation of the initial guesses does not alter the converged solution. Should the initial guess be too far from the solution, and sufficient convergence is not achieved, an error message of non-convergence is displayed.

Chapter 6

Coefficient Study

In our kinetic theory, and irreversible thermodynamics derivations we saw that the flux expressions are dependant on coefficients. In irreversible thermodynamics we have the phenomenological coefficients, while in kinetic theory there are the evaporation, condensation, and accommodation coefficients. In this chapter we investigate the influence the coefficients have on the model results.

6.1 Irreversible Thermodynamics and Statistical Rate Theory

The irreversible thermodynamics simulations use the IT mass and conductive energy fluxes, Eqns. (3.7), and (3.8),

$$j = \beta \left(\frac{g_l}{T_l} - \frac{g_v}{T_v} + h_v \left(\frac{1}{T_v} - \frac{1}{T_l} \right) \right),$$

and

$$q_v = \alpha \left(\frac{1}{T_v} - \frac{1}{T_l} \right).$$

The statistical rate theory model uses the SRT exponential mass flux (3.13), or the linearized SRT mass flux (3.15),

$$j = k_s \left\{ \exp \left[\frac{g_l}{RT_l} - \frac{g_v}{RT_v} + \frac{h_v}{R} \left(\frac{1}{T_v} - \frac{1}{T_l} \right) \right] - \exp \left[\frac{-g_l}{RT_l} + \frac{g_v}{RT_v} - \frac{h_v}{R} \left(\frac{1}{T_v} - \frac{1}{T_l} \right) \right] \right\},$$

$$j = 2k_s \left[\frac{g_l}{RT_l} - \frac{g_v}{RT_v} + \frac{h_v}{R} \left(\frac{1}{T_v} - \frac{1}{T_l} \right) \right],$$

where

$$k_s = \frac{p_{sat}\left(T_l\right)}{\sqrt{2\pi RT_l}},$$

together with the IT energy flux.(3.8). The IT mass flux (3.7), is dependant on the mass flux phenomenological coefficient β, while the IT energy flux depends on the energy flux phenomenological coefficient α. We now investigate the effects of these coefficients on the model results.

6.1.1 Choosing the Phenomenological Coefficients

We have already seen that $\alpha \geq 0$, and $\beta \geq 0$ to ensure positive entropy production. To establish base values for each, from which we can study the results of their variation, we fit the model results to Ward and Stanga's data from their evaporation experiment E1 [4][59]. Table 6.1 gives Ward and Stanga 's measured data split into prescribed parameters, and results, as in our model.

Model Prescribed Parameters					Model Results			
p_v (Pa)	L_l (mm)	L_v (mm)	T_{bl} (°C)	T_{bv} (°C)	T_l (°C)	T_v (°C)	ΔT	j $\left(\frac{\text{kg}}{\text{m}^2\,\text{s}}\right)$
593	4.970	18.590	26.060	25.710	-0.4	2.6	3.0	1.017×10^{-3}

Table 6.1: Ward et al. evaporation experiment E1 data

We see the measured liquid interface temperature is slightly below zero, suggesting the liquid water is on the verge of the super cooled region. Later we comment on how the liquid properties change in the super cooled region.

IT Mass and Energy Flux

Using Eqns. (3.7), and (3.8), we find the best fitting to Table 6.1 for

$$\alpha = 1.55 \times 10^5 \frac{\text{W K}}{\text{m}^2}, \text{ and } \beta = 1 \times 10^{-3} \frac{\text{kg}}{\text{m}^2\,\text{s}} \frac{\text{kg K}}{\text{J}}.$$

The predicted interface temperatures and mass flux with these coefficient values are given in Table 6.2, they compare well with the measured data, Table 6.1.

$\alpha.\left(\frac{\mathrm{W\,K}}{\mathrm{m^2}}\right)$	$\beta\ \left(\frac{\mathrm{kg}}{\mathrm{m^2\,s}}\frac{\mathrm{kg\,K}}{\mathrm{J}}\right)$	T_l (°C)	T_v (°C)	$j\ \left(\frac{\mathrm{kg}}{\mathrm{m^2\,s}}\right)$	$Q\ \left(\frac{\mathrm{W}}{\mathrm{m^2}}\right)$
1.55×10^5	$\beta = 1 \times 10^{-3}$	-0.306	2.67	1.18×10^{-3}	2861

Table 6.2: Interface temperatures, and mass flux, using IT mass and energy flux model

Exponential and Linearized Statistical Rate Theory Mass Flux, with IT Energy Flux

The SRT mass flux expressions (3.13), (3.15) do not have unknown coefficients . We need only find a value for α from Eqn. (3.8). For both the exponential SRT and the linearized SRT, the best fit is for $\alpha = 1.535 \times 10^5 \frac{\mathrm{W\,K}}{\mathrm{m^2}}$. Table 6.3 gives the resulting interface temperatures and fluxes which are the same for both SRT expressions.

$\alpha.\left(\frac{\mathrm{W\,K}}{\mathrm{m^2}}\right)$	T_l (°C)	T_v (°C)	$j\ \left(\frac{\mathrm{kg}}{\mathrm{m^2\,s}}\right)$	$Q\ \left(\frac{\mathrm{W}}{\mathrm{m^2}}\right)$
1.535×10^5	-0.329	2.67	1.18×10^{-3}	2861

Table 6.3: SRT Interface Temperatures and Fluxes

We see the values of α do not change greatly for the three different mass flux expressions. Comparing Table 6.2 to the measured data, Table 6.3, the predicted interface temperatures and mass fluxes are again close to the measured values.

We recall that the linearized SRT expression (3.15) can be written in the same form as the IT mass flux (3.7), yielding the SRT value of β (3.17),

$$\beta_{SRT} = \frac{p_{sat}\left(T_l\right)}{R^{\frac{3}{2}}}\sqrt{\frac{2}{\pi T_l}}$$

We evaluate β_{SRT} for liquid interface temperature $T_l = -0.4\,°\mathrm{C}$, and find $\beta_{SRT}\left(-0.4\,°\mathrm{C}\right) = 2.88 \times 10^{-3} \frac{\mathrm{kg}}{\mathrm{m^2\,s}} \frac{\mathrm{kg\,K}}{\mathrm{J}}$, which is of the same order of magnitude as the value we found from irreversible thermodynamics.

6.1.2 Variation of Results with the Phenomenological Coefficients

In the previous section we established base values for the phenomenological coefficients, $\alpha = 1.5 \times 10^5 \frac{\mathrm{W\,K}}{\mathrm{m}^2}$, and $\beta = 1 \times 10^{-3} \frac{\mathrm{kg}}{\mathrm{m}^2\,\mathrm{s}} \frac{\mathrm{kg\,K}}{\mathrm{J}}$. We now vary both by an order of magnitude to establish their influence on the model results.

Simultaneous Variation of α, and β, IT Mass, and Energy Fluxes

We use the IT mass and energy fluxes, Eqns. (3.7), and (3.8), with the prescribed parameters from the measured data, Table 6.1.

Figure 6.1 shows the liquid interface temperature is nearly constant for most values of α and β, except for small β, where the gradient is steep. However for both, the liquid interface temperature changes less than a degree.

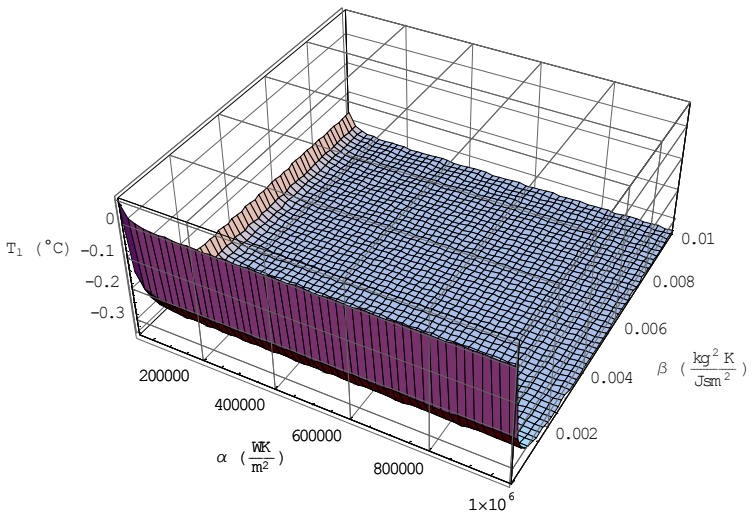

Figure 6.1: Liquid interface temperature versus α and β

Figure 6.2 shows the independence of vapor interface temperature from β. The temperature increases significantly as α is decreased.

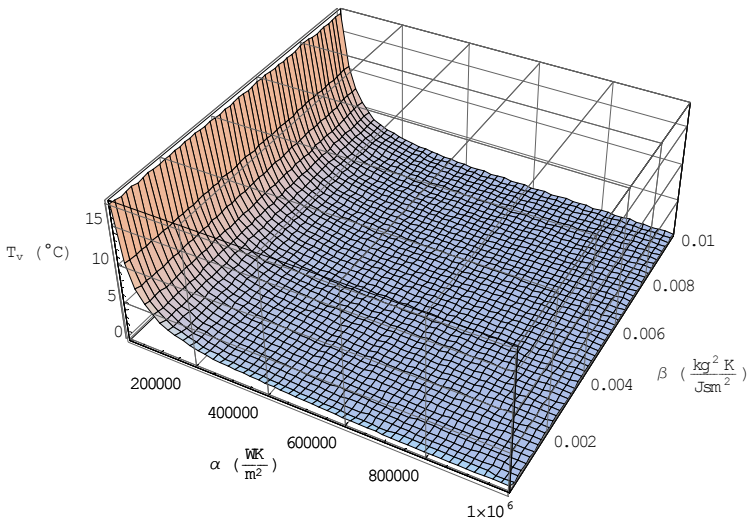

Figure 6.2: Vapor interface temperature versus α and β

Thus the temperature jump is strongly related to the choice of α, but is almost independent of β, see Figure 6.3. The vapor interface temperature change with α is one order of magnitude more significant than the liquid interface temperature change with β and α. It follows that the temperature jump increases as α is reduced.

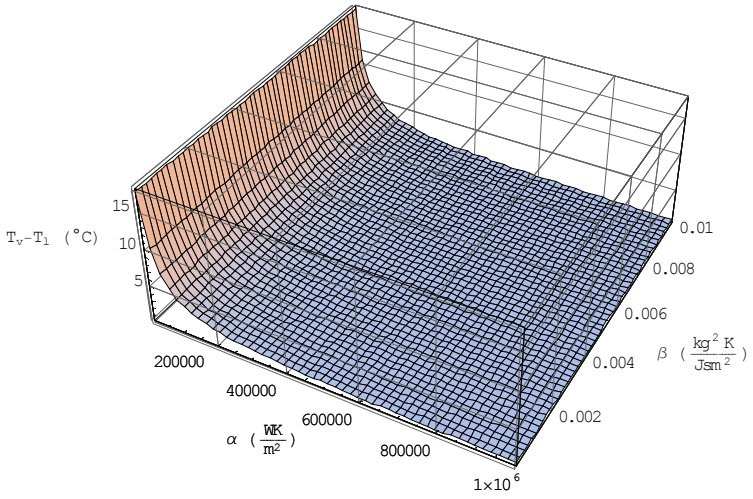

Figure 6.3: Interface temperature jump versus α and β

Figures 6.4, and 6.5 illustrate that the mass and energy fluxes are approximately constant with the variation of α, and β. Both fluxes vary more for small α, or β but the variation is less than 2%.

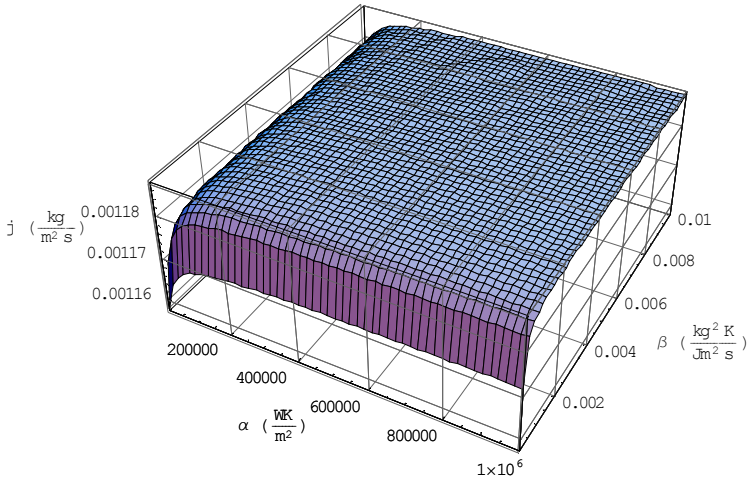

Figure 6.4: Mass flux versus α and β

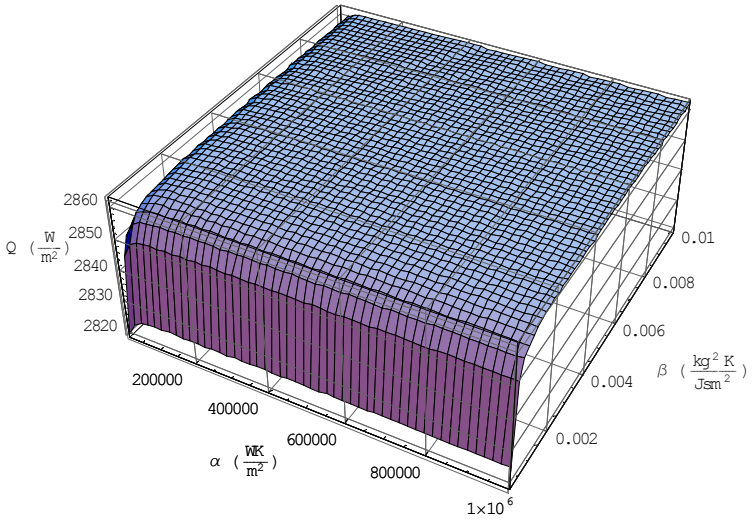

Figure 6.5: Energy flux versus α and β

We use Eqn. (2.27) to calculate the entropy production at the interface. Figure 6.6 gives the entropy production, we see it remains positive, as must be the case for positive α and β.

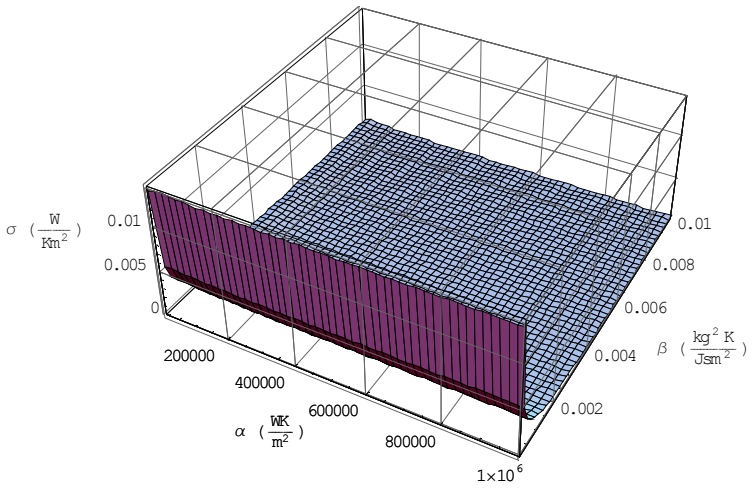

Figure 6.6: Entropy Production versus α and β

The value of the phenomenological conductive energy flux coefficient α strongly affects T_v, and the temperature jump across the interface. Reducing the energy force coefficient increases T_v, and the interface temperature jump, with little effect on T_l, j, and Q. A possible explanation is that T_l, j, and Q are unaffected by α because of the high liquid conductivity, which implies that the fluxes and T_l are more dependant on the liquid properties than those of the vapor.

The phenomenological conductive mass flux coefficient β does slightly affect T_l, j, and Q. It has a negligible effect on T_v and the interface temperature jump.

Variation of α, SRT Mass Flux and IT Energy Flux

The conductive energy flux phenomenological coefficient α in Eqn. (3.8) is varied as in the previous section, but in conjunction with the exponential, or linearized SRT mass fluxes (3.13), (3.15). Both cases yield the same results.

The results are similar to those we found with the linear force mass flux model. Variation of α strongly affects T_v and the temperature jump, but has only a small effect on T_l, j, and Q, see

Figures 6.7- 6.11.

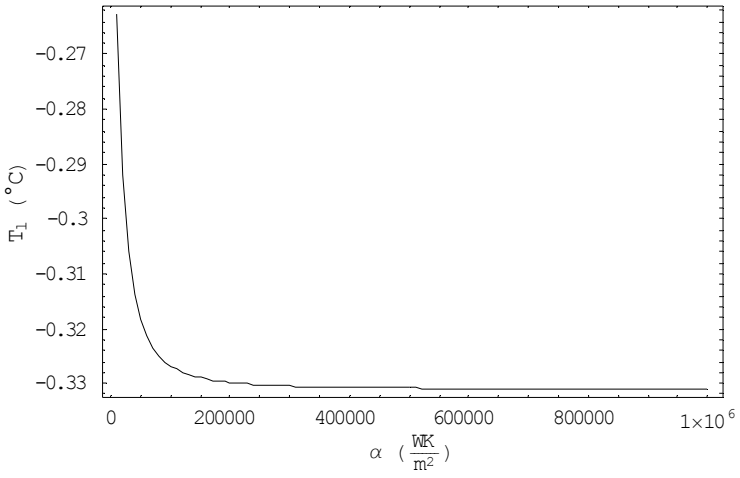

Figure 6.7: Liquid interface temperature versus α

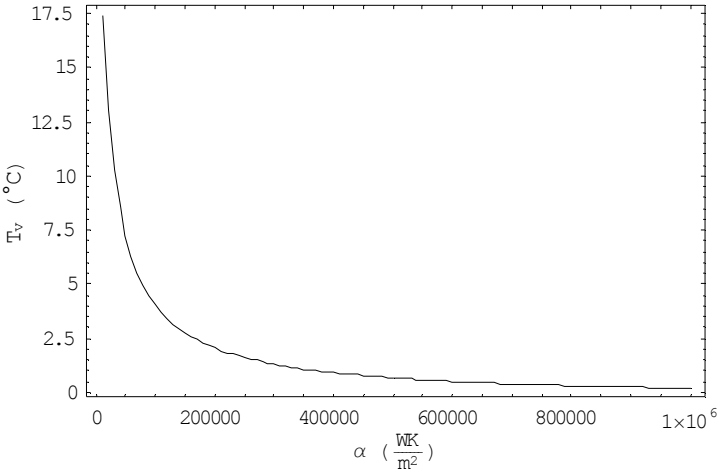

Figure 6.8: Vapor interface temperature versus α

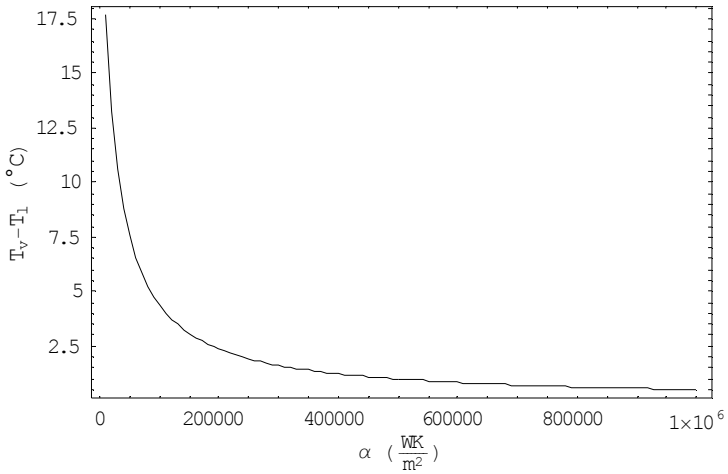

Figure 6.9: Temperature jump versus α

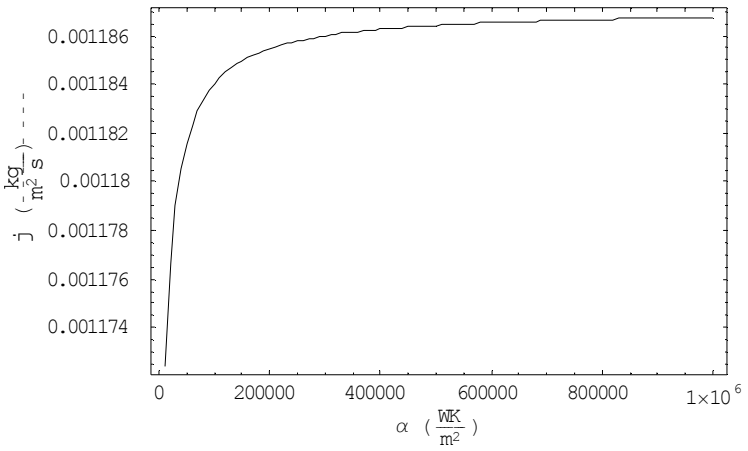

Figure 6.10: Mass flux versus α

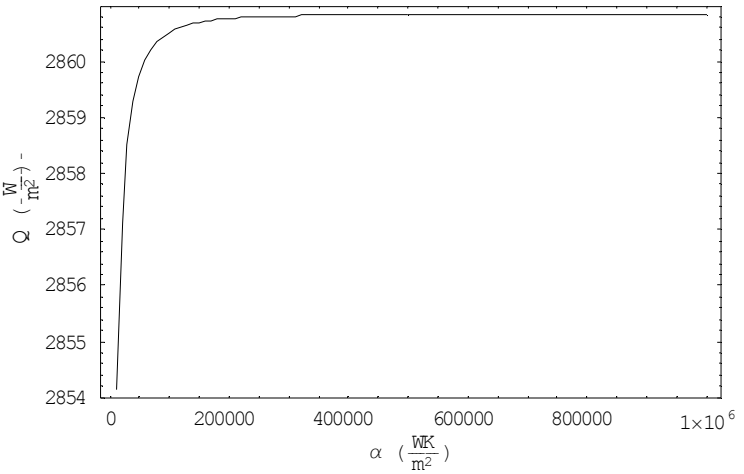

Figure 6.11: Energy Flux versus α

We use Eqn. (2.27) to calculate the entropy production at the interface. We see from Figure 6.12 that the entropy production remains positive. We expect this to be the case since both α, and β_{SRT} are positive.

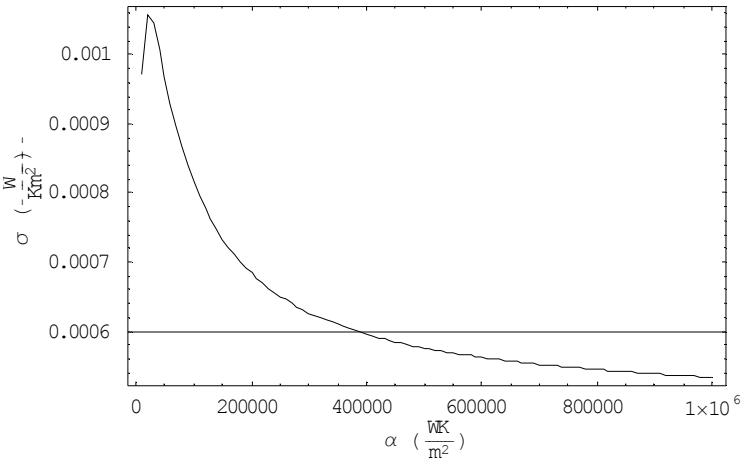

Figure 6.12: Entropy production versus α

We conclude, that the interface temperature jump is not strongly affected by the mass flux expression, but is highly dependant on the IT conductive energy flux expression (3.8). Eqn.

(3.8) predicts the same temperature jump direction $T_v > T_l$ as the measured data, Table 6.1, and with the appropriate choice of α can also predict the correct magnitude.

6.2 Kinetic Theory

We investigate the variation of the condensation coefficient θ_c, the evaporation coefficient θ_e, the accommodation coefficient γ, and the velocity dependant condensation parameters ψ and ω. Each of these coefficients have clearly defined ranges of possible values. Thus there is no need to establish base point values, as we did for irreversible thermodynamics. The energy flux reference point is corrected as per Eqn. (4.82). Again, we use the experimental input parameters from Table 6.1.

6.2.1 Variation of Evaporation and Condensation Coefficients for Specular and Diffuse Reflection

We investigate the effects of the condensation, and evaporation coefficients on the results for specular and diffuse reflection. For this we use the HK, and CE flux expressions with constant condensation and evaporation coefficients, Eqns. (4.22), (4.44), (4.25), and (4.49). As discussed earlier (Chapter 4) if the evaporation and condensation coefficients are constants, they must be equal $\theta_c = \theta_e$, for the equilibrium conditions are to be fulfilled. We set $\theta_c = \theta_e = \theta$, and vary θ between 1 and 0.1. We find an indeterminate result for $\theta = 0$, thus we stop at 0.1. We look at the two extreme cases for the accommodation coefficient, purely specular reflection $\gamma = 1$, and purely diffuse reflection $\gamma = 0$.

The HK and CE models behave similarly. The results for specular and diffuse reflection are also very close, except for T_v and the interface temperature jump. We represent both the HK, and CE models for specular and diffuse reflection with one set of Figures, except for T_v and the interface temperature jump where we show both specular and diffuse cases.

We see from Figure 6.13 that T_l increases as θ approaches zero. When compared with the irreversible thermodynamics and SRT results, and the measured data, Tables 6.2, 6.3, and 6.1, we see very good agreement for $\theta = 1$.

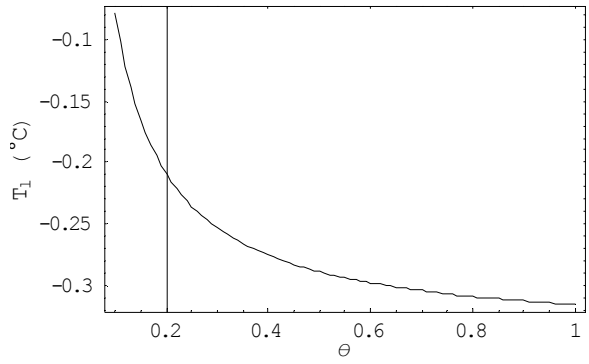

Figure 6.13: Liquid interface temperature versus θ

Comparing Figures 6.14, and 6.15 we see that T_v behaves differently with θ for purely diffuse reflection, than specular reflection. In both cases though, T_v is not near the calculated irreversible thermodynamics and SRT results, or the measured data, Tables 6.2, 6.3, and 6.1.

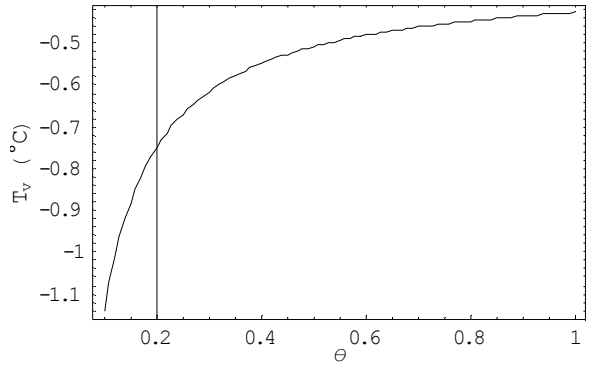

Figure 6.14: Vapor interface temperature versus θ for specular reflection

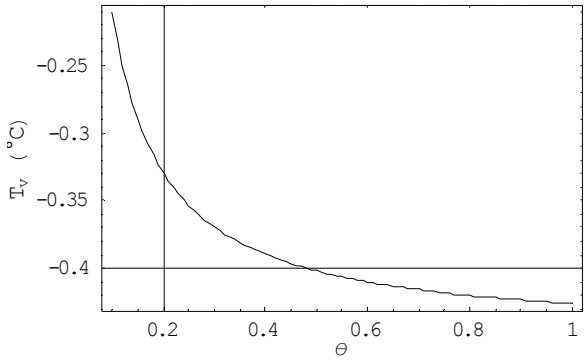

Figure 6.15: Vapor interface temperature versus θ for diffuse reflection

Indeed, we see from Figures 6.16, and 6.17 that for both, pure, specular, and pure diffuse reflection, the temperature jump is negative, $T_l > T_v$, for any choice of θ. This is the opposite direction to what we observed from irreversible thermodynamics, Tables 6.2 and 6.3, and from the measurements, Table 6.1. However it is the same as the temperature jump direction predicted from kinetic theory in the literature [32], [33].

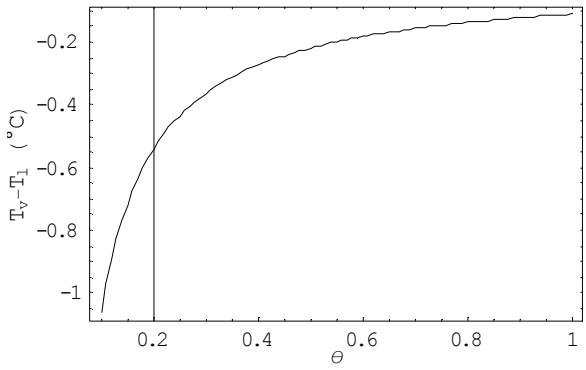

Figure 6.16: Interface temperature jump versus θ for specular reflection

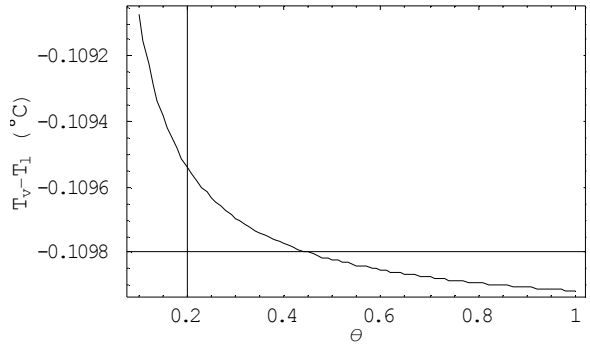

Figure 6.17: Interface temperature jump versus θ for diffuse reflection

For specular reflection, the temperature jump becomes increasingly negative as θ goes to zero. This is likely so, because if no evaporation or condensation mass flux occurs, and the molecules are reflected specularly, then there will be no thermal interaction between the liquid and vapor. For the diffuse case we see the jump approaches zero as θ gets small, because reflected molecules undergo complete thermal interaction with the interface, thus there is temperature equalization between the liquid, and vapor.

We also point out that for $\theta = 1$ the choice of specular or diffuse reflection is irrelevant, since there are no reflected molecules, as seen from Figures 6.14, 6.15, 6.16, and 6.17.

We see from Figures 6.18, and 6.19 that j and Q vary only a small amount for the values of θ considered. Their values are close to the measured fluxes, and those calculated using irreversible thermodynamics and SRT, Tables 6.2, 6.3, and 6.1. However, as θ is reduced, they both approach zero, demonstrating that if no molecules condense or evaporate there should be neither mass nor energy flux. The prior statement is true for pure specular reflection, but since diffusely reflected molecules will interact thermally with the surface, we might expect some energy flux, even if no molecules change phases.

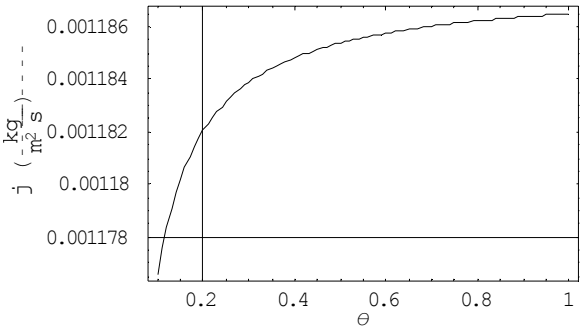

Figure 6.18: Mass flux versus θ

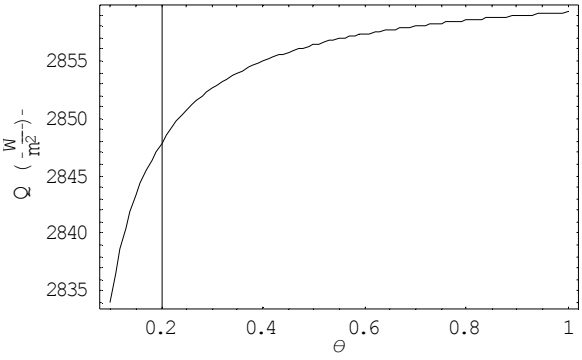

Figure 6.19: Energy flux versus θ

As with irreversible thermodynamics and SRT we use Eqn. (2.27) to calculate the entropy production. We see from Figure 6.20 that the entropy production is positive for specular and diffuse reflection, with any value of θ.

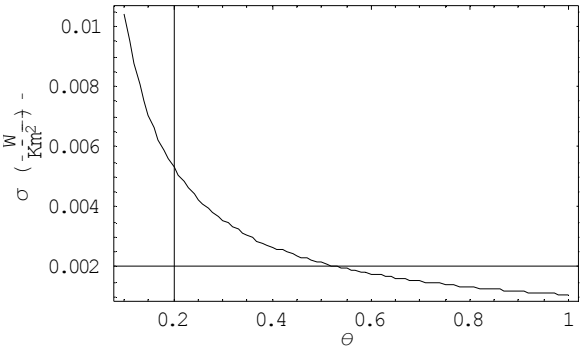

Figure 6.20: Entropy production versus θ

In conclusion we note that the CE and HK expressions give very similar results in the case of constant θ. The resulting fluxes are close to those calculated using irreversible thermodynamics and SRT, and measurements, Tables 6.2, 6.3, and 6.1. We see the liquid interface temperature also has good agreement. However the temperature jump is considerably smaller and in the opposite direction, for any choice of evaporation condensation coefficient, or accommodation coefficient. Importantly, the entropy production is positive.

6.2.2 Velocity and Temperature Dependant Condensation Coefficient Specular and Diffuse Reflection

Now, we use the HK and CE velocity dependant condensation coefficient expressions (HKVEL and CEVEL) for diffuse and specular reflection, Eqns. (4.60), (4.67), (4.71), (4.74), and (4.75). We investigate the effects of the condensation coefficient parameters ψ and ω for both, purely specular and diffuse reflection.

As we did earlier, we use the experimental input parameters from Table 6.1. The range of possible values for ψ, and ω, between 0 and 1 has already been established in Section 4.6. We vary ψ between 0.1 and 1, because as mentioned in the last section, a condensation evaporation coefficient of 0 yields an indeterminate result. ω is varied over its full range, $0-1$. Again we find the HK and CE distributions give similar results; thus they are presented together. The effects of ψ and ω are similar for specular and diffuse reflection. The only differences occur

with the interface temperatures, and the interface temperature jump. The specular and diffuse results are represented together, except for the interface temperatures, and temperature jump where we present both the specular and diffuse cases.

Figures 6.21, and 6.22, show for diffuse reflection, that both, T_l and T_v, are nearly constant except for small ψ, where they both increase for large ω. From Eqn. (4.51),

$$\theta_c = \psi \left[1 - \omega \exp\left(\frac{-mc^2}{2kT_l} \right) \right], \tag{6.1}$$

this implies that the interface temperatures become highly dependant on molecular energy and surface temperature only for a small condensation coefficient θ_c.

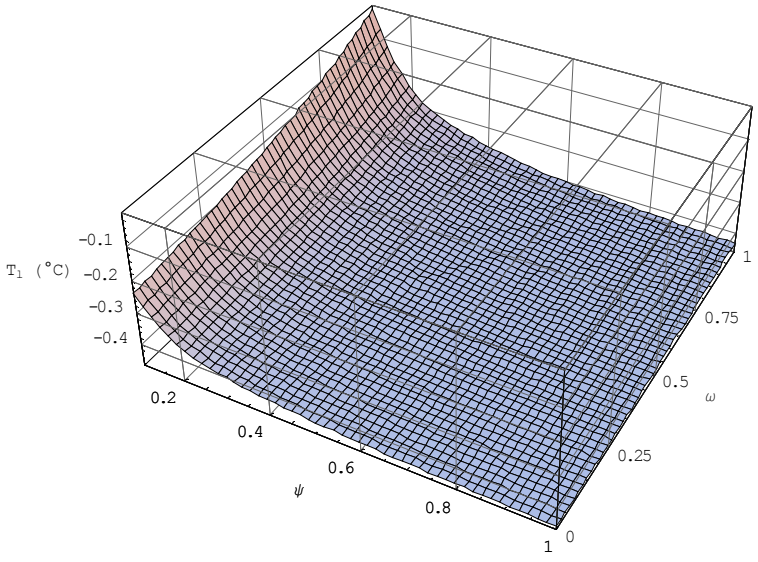

Figure 6.21: Liquid interface temperature versus ψ and ω for diffuse reflection

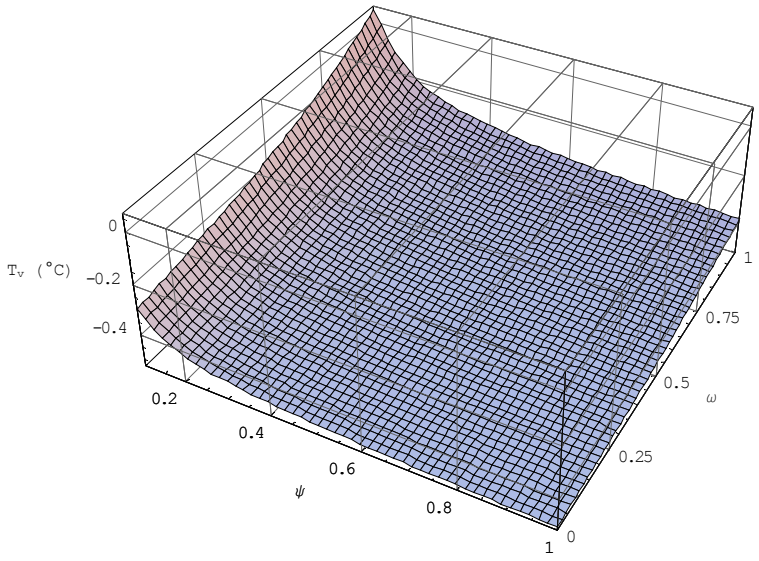

Figure 6.22: Vapor interface temperature versus ψ and ω for diffuse reflection

We see from Figure 6.23, that for diffuse reflection the temperature jump behaves similarly to the interface temperatures, it is maximum for small ψ, and large ω. We also remark that this maximum is positive implying $T_v > T_l$, which is the direction we observed from irreversible thermodynamics and SRT, and from measurements, Tables 6.2, 6.3, and 6.1.

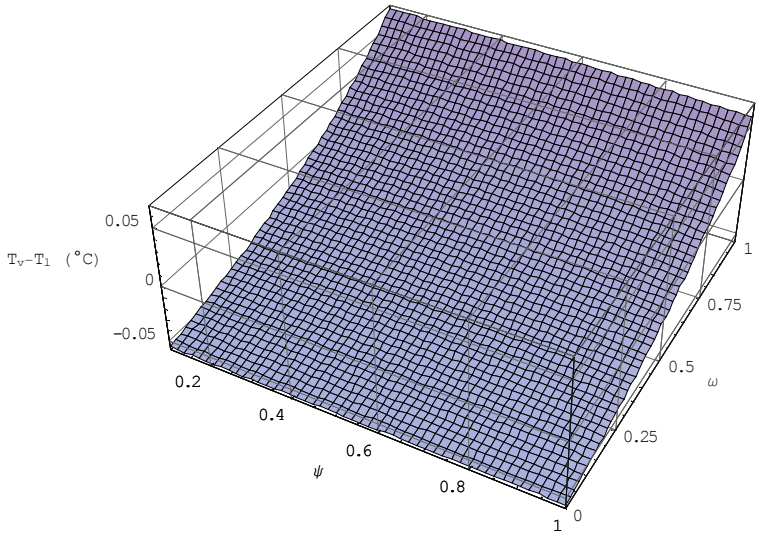

Figure 6.23: Interface temperature jump versus ψ and ω for diffuse reflection

For the purely specular reflecting case the interface temperature and jump results have more pronounced extremes for small ψ, and large ω. To explore these more fully, we extended the range of ψ to between 0.01 and 1. We see from Figures 6.24, and 6.25 that T_l, and T_v can reach over 3 °C, significantly higher than for diffuse reflection, and near the measured T_v value, Table 6.1. We check this by adjusting ψ and ω to match the measured T_v value, the results of which are found in Table 6.4.

ψ	ω	γ	T_l (°C)	T_v (°C)	$j\ \left(\frac{\text{kg}}{\text{m}^2\,\text{s}}\right)$	$Q\ \left(\frac{\text{W}}{\text{m}^2}\right)$
0.0174	1	1	2.01	2.67	1.08×10^{-3}	2612

Table 6.4: HKVEL and CEVEL interface temperatures and fluxes

Note that the T_l value is 2 °C higher than the measured value. We suggest that this might imply the molecules leaving the surface, leave with a higher temperature than the surface.

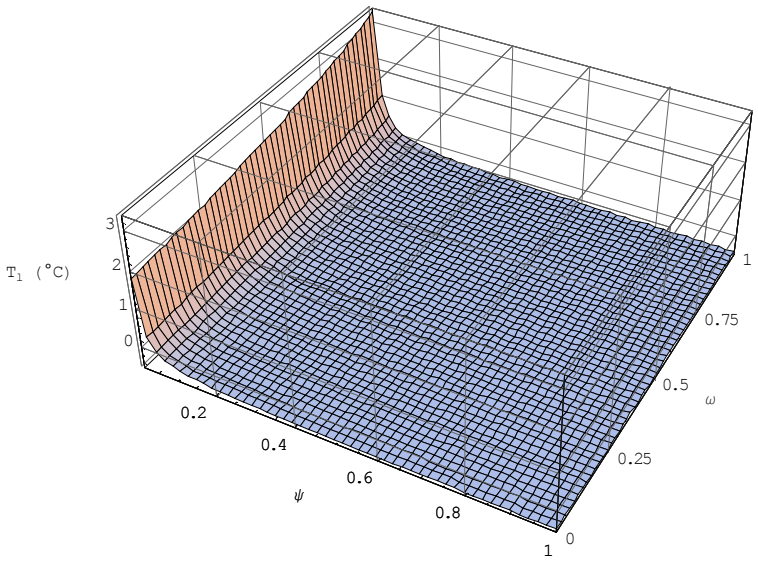

Figure 6.24: Liquid interface temperature versus ψ and ω for specular reflection

We see for specular reflection, Figure 6.26, that the temperature jump is again positive for small ψ, and large ω.

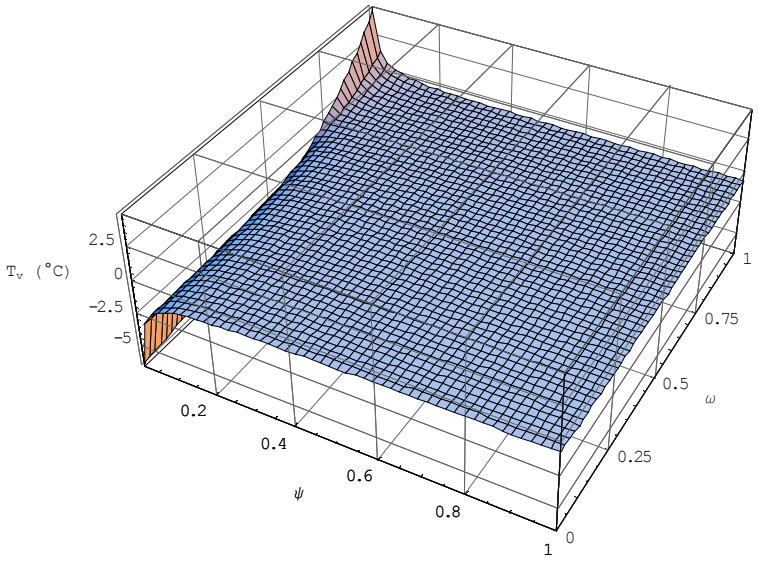

Figure 6.25: Vapor interface temperature versus ψ and ω for specular reflection

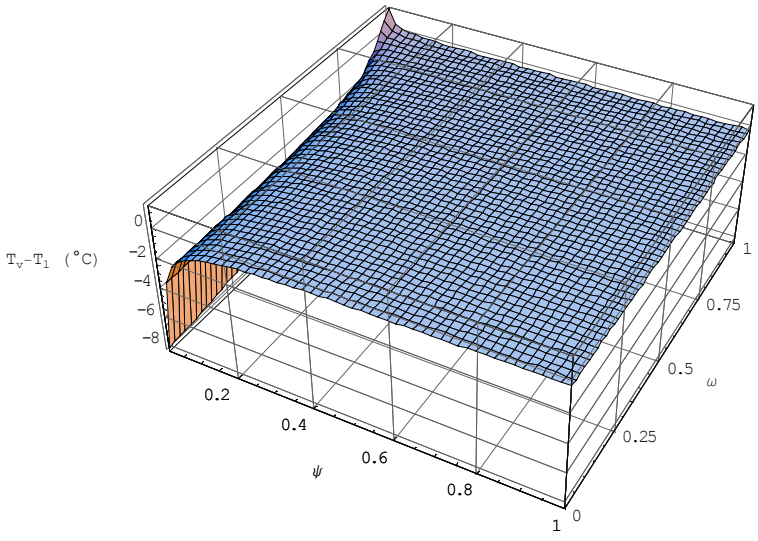

Figure 6.26: Interface temperature jump versus ψ and ω for specular reflection

We see from Figures 6.27, and 6.28 that the mass and energy fluxes behave as they did for the constant condensation evaporation coefficient: they are almost constant for large evaporation and condensation coefficients, and fall as the condensation and evaporation coefficients are made small, and are close to the other model results and measurements, Tables 6.4, 6.2, 6.3, and 6.1. We also remark from the mass and energy flux independence of ω, that the molecular energy c^2, and surface temperature T_l have little influence on the fluxes.

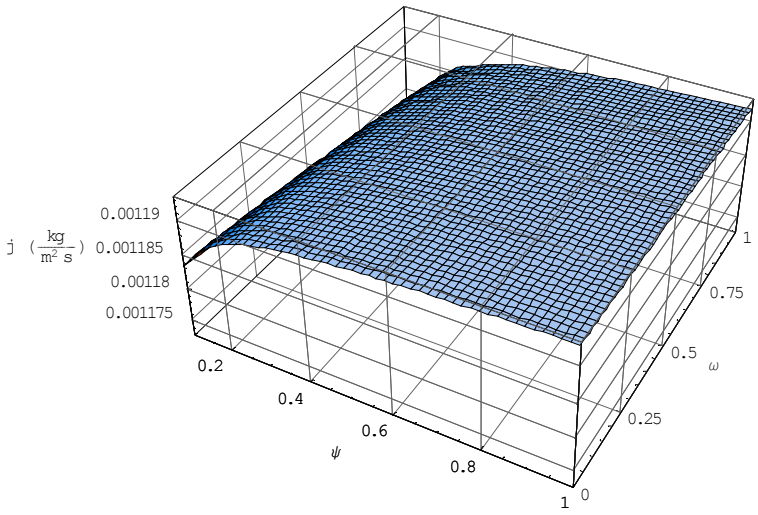

Figure 6.27: Mass flux versus ψ and ω

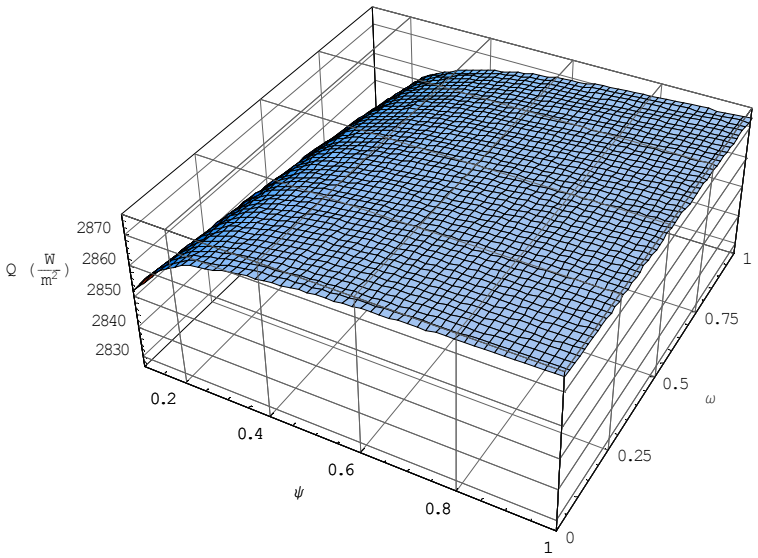

Figure 6.28: Energy flux versus ψ and ω

In Figure 6.29 we see again, that the entropy production, as calculated from Eqn. (2.27) is positive.

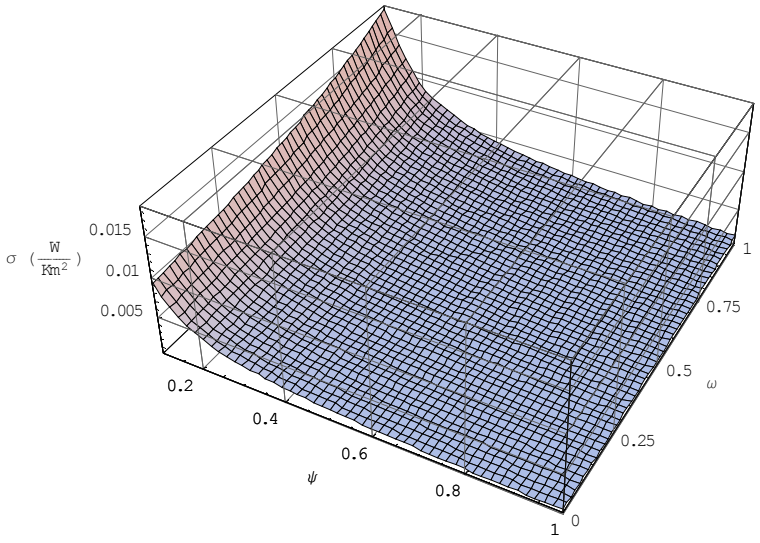

Figure 6.29: Entropy production versus ψ and ω

We conclude that the velocity dependant condensation coefficient (4.51) for small ψ, and large ω alters the kinetic theory flux expressions sufficiently, to predict the same vapor interface temperature, jump direction, and fluxes as found with irreversible thermodynamics, SRT, and measurements, Tables 6.4, 6.2, 6.3, and 6.1.

We also conclude, as we did in the previous section that the HK and CE distributions yield similar results. This implies that the deviation from the Maxwelllian (4.6) in the CE distribution (4.13) has little effect on evaporation phenomena. The details of the interaction between vapor and liquid, which determine θ and γ, however, are of great importance, and influence, since their variation leads to quite distinct results. In particular it must be noted that constant θ can not provide data in agreement with the Ward and Stanga measurements [4].

Chapter 7

Variation of Results with Vapor Pressure

Next, we look at the predicted interface temperatures and fluxes for various vapor pressures. The liquid and vapor boundary temperatures are set equal, $T_{bl} = T_{bv} = T_b$, to eliminate forcing caused by a temperature difference between the boundaries. The system will be in equilibrium when the vapor pressure is equal to the boundary temperature saturation pressure, $p_v = p_{eq} = p_{sat}(T_b)$. The boundary conditions are in Table 7.1.

L_l (m)	L_v (m)	T_b (°C)
1×10^{-3}	1×10^{-3}	25

Table 7.1: Symmetric temperature boundary conditions

The saturation pressure is, $p_{sat}(25\,^\circ\mathrm{C}) = 3.169\,\mathrm{kPa}$ [56]. We vary the vapor pressure around this point, from 1 kPa to 5 kPa.

We consider the IT (3.7)(3.8), the SRT (3.13), the linearized SRT (3.15), the HK (4.8) (4.9) and CE (4.16) (4.20) without condensation and evaporation coefficient, and the HK (4.60) (4.67) and CE (4.71) (4.74) (4.75) with velocity dependant condensation coefficient models (HKVEL, CEVEL). The constant condensation and evaporation coefficient HK (4.22) (4.44) and CE (4.25) (4.49) models are not considered since they predict the wrong sign for the interface temperature jump. Where coefficient values are required, we use those found from the data fitting in the previous chapter, Tables 6.2, 6.3, and 6.4.

Figure 7.1 shows that the liquid interface temperatures of the IT and SRT models, and the HK and CE models vary closely with the vapor pressure saturation temperature, $T_{sat}(p_v)$. The velocity dependant condensation coefficient models have different slopes than the vapor pressure saturation temperature, however they are still close, especially near the equilibrium pressure $p_{sat}(T_b)$.

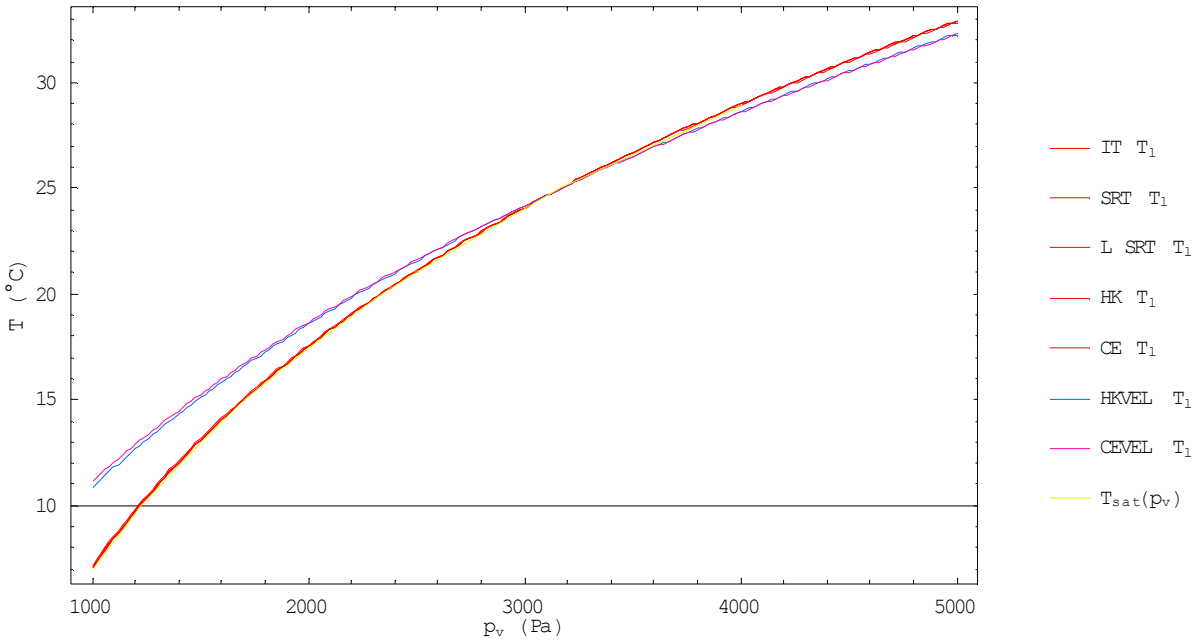

Figure 7.1: Liquid interface temperature and vapor pressure saturation temperature versus vapor pressure

Figure 7.2 facilitates the comparison of vapor interface temperatures with the vapor pressure saturation temperature. They are equal at the equilibrium pressure. The HK and CE models follow the saturation temperature. The IT, SRT, HKVEL, and CEVEL models are above the saturation temperature for pressures less than the equilibrium pressure, and below the saturation temperature for pressures above the equilibrium pressure. As discussed in the introduction, pressures below the equilibrium pressure result in evaporation, while those above cause condensation.

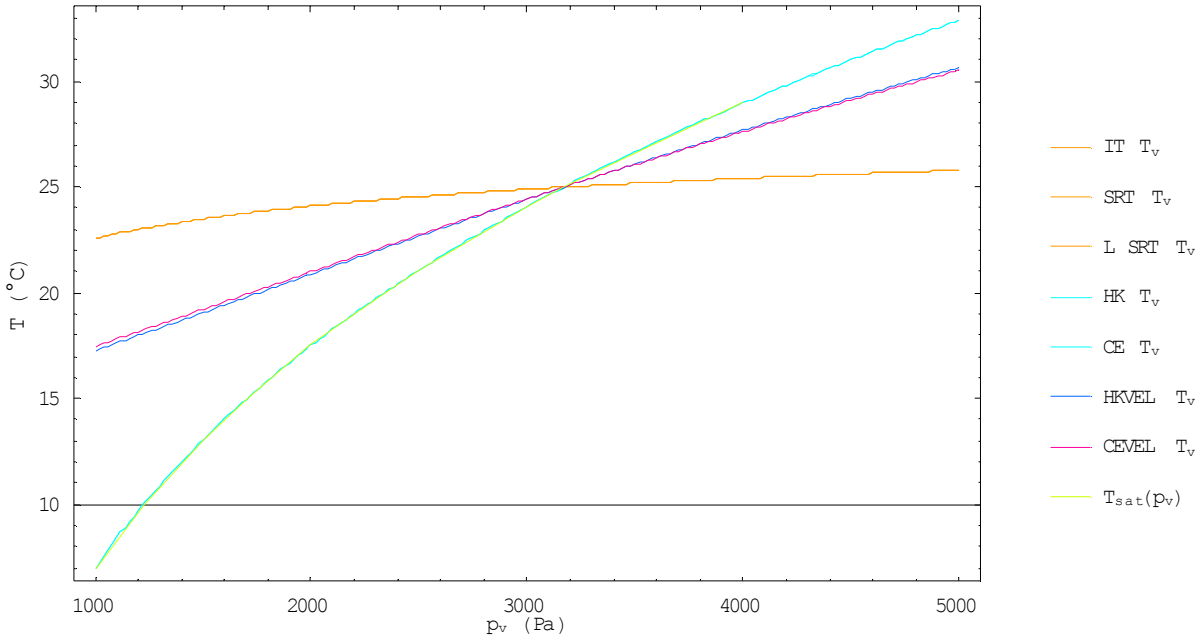

Figure 7.2: Vapor interface temperature and vapor pressure saturation temperature versus vapor pressure

The interface temperature jump, Figure 7.3, shows the HK and CE models predict a negligible jump. The other models predict a positive jump for vapor pressure below the equilibrium pressure (evaporation), and negative jump above the equilibrium pressure (condensation). Of course all models show zero temperature jump at equilibrium.

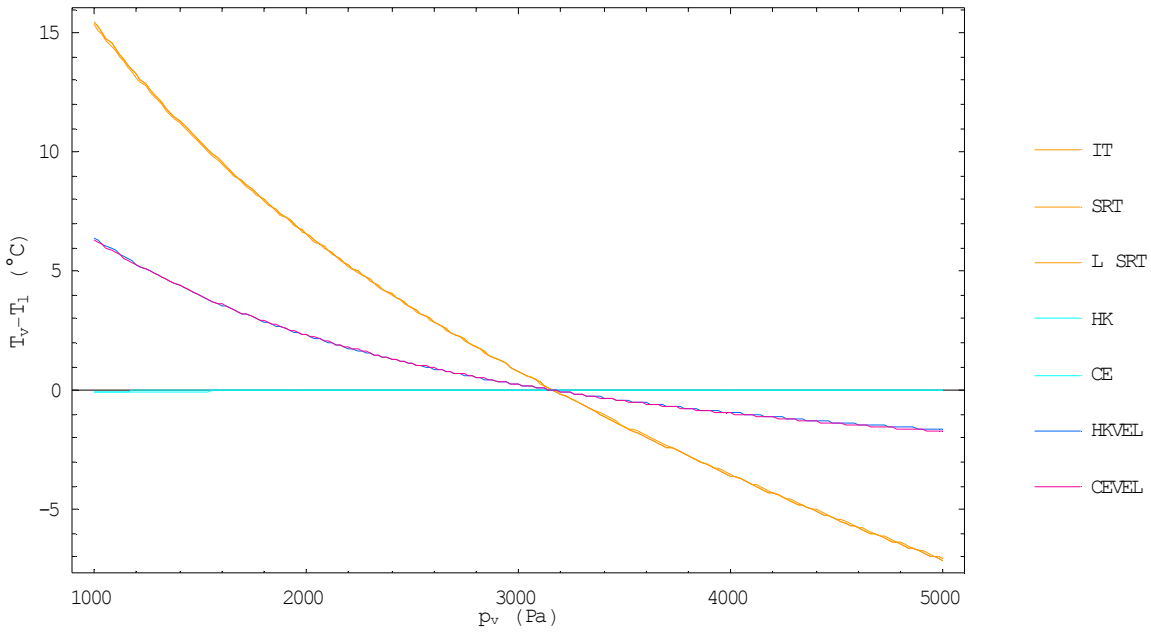

Figure 7.3: Interface temperature jump versus vapor pressure

Figure 7.4 shows the mass flux is positive to the left of equilibrium, zero at equilibrium, and negative to the right Positive mass flux means evaporation, and negative means condensation. Reducing the vapor pressure results in increased evaporation; increasing the vapor pressure increases the condensation. There are three distinct groups of curves. The IT and SRT models, the HK and CE models, and the HKVEL and CEVEL models. Close to the equilibrium point all the models closely agree. Away from equilibrium the IT and SRT, and HKVEL and CEVEL models are still close. The HKVEL and CEVEL predict lower magnitude fluxes than the other models.

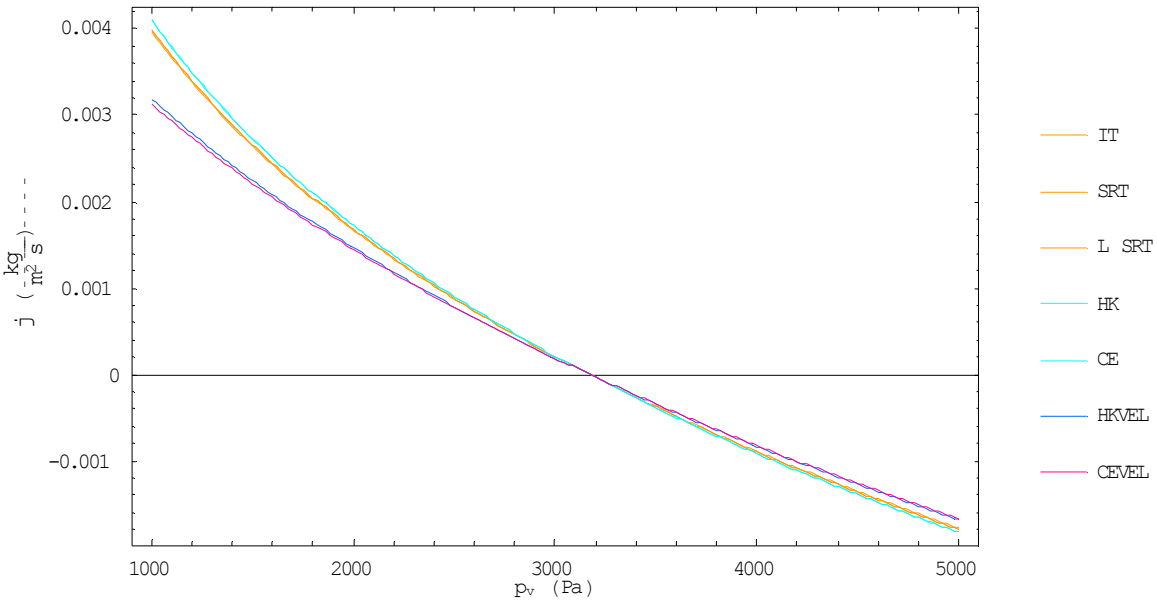

Figure 7.4: Mass flux versus vapor pressure

The energy flux, Figure 7.5, behaves similar to the mass flux. The energy flux increases with reduced vapor pressure, and becomes more negative with increased vapor pressure. As expected, the energy flux is zero at the equilibrium pressure. Again we see the IT, SRT, HK, and CE models are close, while the HKVEL and CEVEL models predict lower fluxes.

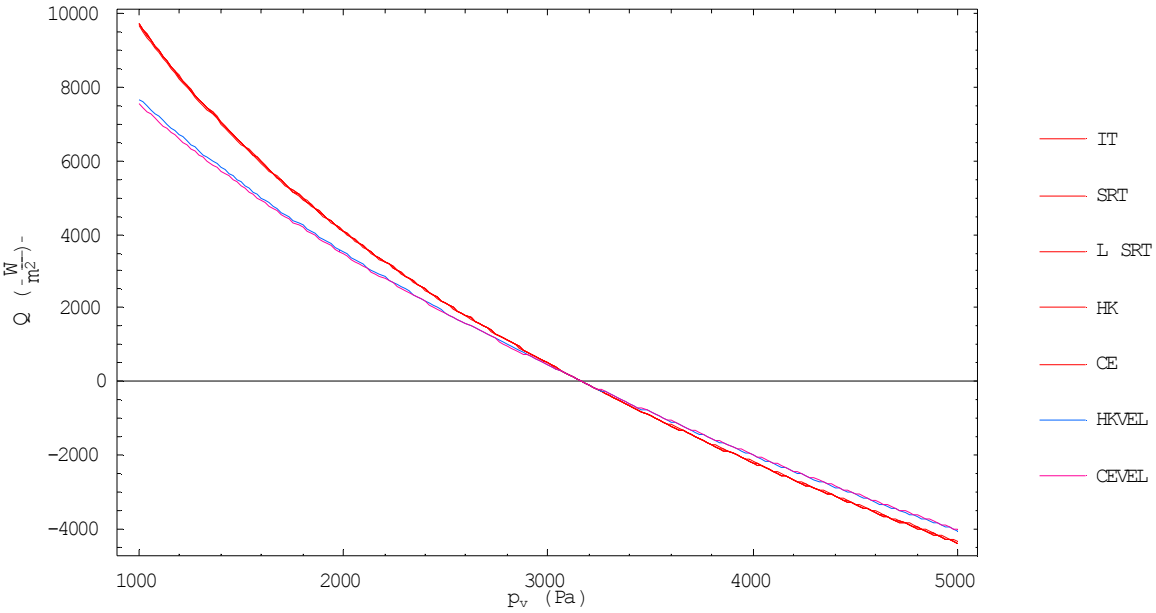

Figure 7.5: Energy flux versus vapor pressure

Figure 7.6 demonstrates that the entropy production is zero at equilibrium, and increases as we move away from equilibrium in both the evaporation and condensation directions. The entropy production is very temperature sensitive, as shown by the large differences in entropy production between models, for small differences in interface temperatures. Importantly for all our models it is positive. Note that only the IT model was constructed to ensure positive entropy production, while the kinetic theory models were constructed independently of entropy production. That they always show positive entropy production helps to validate the theories on which they are based.

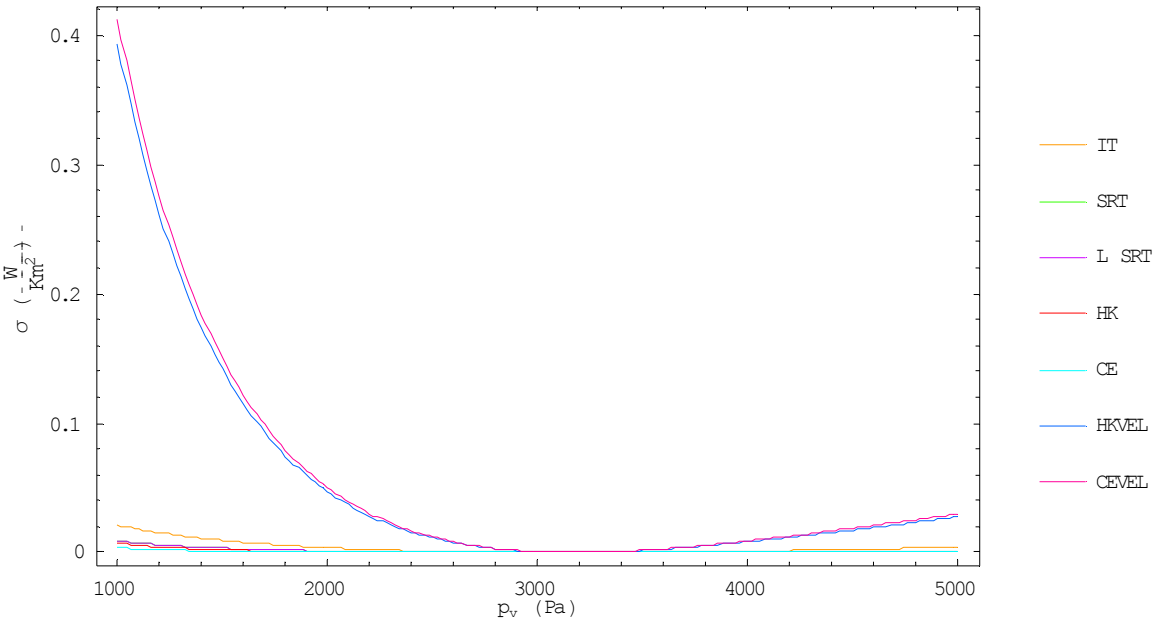

Figure 7.6: Interface entropy production versus vapor pressure

From the previous figures it becomes clear that the interface temperatures, fluxes, and entropy production are strong functions of vapor pressure. Vapor pressures below the boundary temperature saturation pressure $p_v < p_{sat}(T_b)$ lead to evaporation, which coincides with positive interface temperature jump $T_v > T_l$, except for the HK and CE models where the temperature jump is too small to detect. Vapor pressures greater than the boundary temperature saturation pressure $p_v > p_{sat}(T_b)$ cause condensation with a negative temperature jump $T_v < T_l$, except for the HK and CE models where it is again very small .

The IT and SRT models all behave very similarly, suggesting that the exponential form of the SRT expression is not necessary for this case. The HK and CE models are also very close, indicating that using the CE distribution with small vapor velocity does not greatly improve the results found using the Maxwellian distribution with no vapor velocity. The same is true for the HKVEL and CEVEL models.

Finally we emphasize again that the HKVEL and CEVEL models predict the same temperature jump directions as the IT and SRT models, while the conventional HK and CE models fail to do so.

Chapter 8

Liquid and Vapor Temperature Profile Analysis

8.1 Condensation and Evaporation Temperature Profiles

Now we investigate the liquid and vapor temperature profiles. We are interested in the directions of the interface temperature jump, and temperature gradients for the different inputs of vapor pressure p_v, and liquid and vapor boundary temperatures T_{bl} and T_{bv}. The analysis is performed using the SRT (3.13) (3.8), CE (4.16) (4.20), and CEVEL (4.71) (4.74) (4.75) models. We choose these because in the previous chapters, the SRT model closely agrees with the linearized SRT (3.15) and IT (3.7)(3.8) models, the CE model is an excellent fit with the HK model (4.8) (4.9), and the CEVEL model agrees well with the HKVEL model (4.60) (4.67). Where coefficient values are required, we use again those found from the data fitting in the previous Chapters, Tables 6.2, 6.3, and 6.4. We use the symmetric input parameters from Table 8.1.

L_l (m)	L_v (m)	T_b (°C)
1×10^{-3}	1×10^{-3}	25

Table 8.1: Symmetric temperature boundary conditions

We recall that the equilibrium pressure is $p_{sat}\,(25\,^{\circ}\mathrm{C}) = 3.169\,\mathrm{kPa}$ [56]. Evaporation is given by Figure 8.1, where the vapor pressure was set to $p_v = 2.339\,\mathrm{kPa}$, below the equilibrium pressure. Equilibrium, zero temperature jump, and temperature gradient is achieved by setting the vapor pressure equal to the equilibrium pressure, $p_v = p_{sat}\,(25\,^{\circ}\mathrm{C})$ Figure 8.2 shows condensation, achieved by specifying the vapor pressure as greater than the equilibrium pressure, $p_v = 5.628\,\mathrm{kPa}$.

Figure 8.1 shows the direction of the evaporation temperature gradients. The liquid tempera-

ture gradient, on the left, is negative. The vapor temperature gradient on the right is positive. This implies that the conductive heat flux in both phases flows towards the interface. This can be understood by taking into account that energy influx is required to vaporize liquid water.

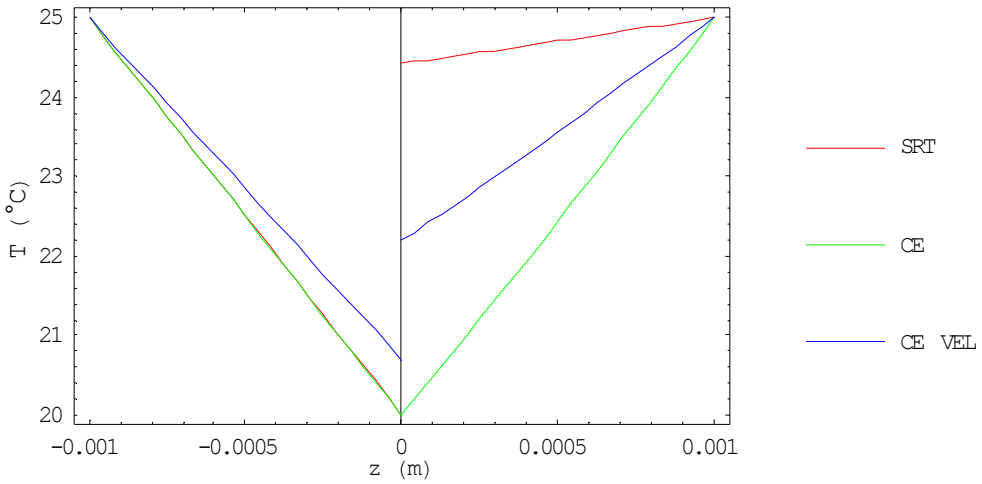

Figure 8.1: Evaporation liquid and vapor temperature profiles

As discussed earlier, the SRT and CE liquid interface temperatures are very close to the saturation temperature of the vapor pressure, $T_{sat}\,(2.339\,\mathrm{kPa}) = 20\,^{\circ}\mathrm{C}$ [56], and the CEVEL liquid interface temperature is above the saturation temperature. The temperature jumps are positive with the vapor interface temperature being greater than the liquid interface temperature $T_v > T_l$, except for the CE model where it is again small.

Figure 8.2 demonstrates the temperature gradients are reversed for condensation. The liquid temperature gradient becomes positive, while the vapor temperature gradient is negative. The conductive heat fluxes are away from the interface, transporting away the energy given off by the condensing liquid.

The SRT and CE model liquid interface temperatures are close to the saturation temperature of the vapor pressure, $T_{sat}\,(5.628\,\mathrm{kPa}) = 35\,^{\circ}\mathrm{C}$ [56]. The temperature jumps are now reversed with the liquid interface temperature greater than that of the vapor, $T_v < T_l$. The CE temperature jump is again near zero.

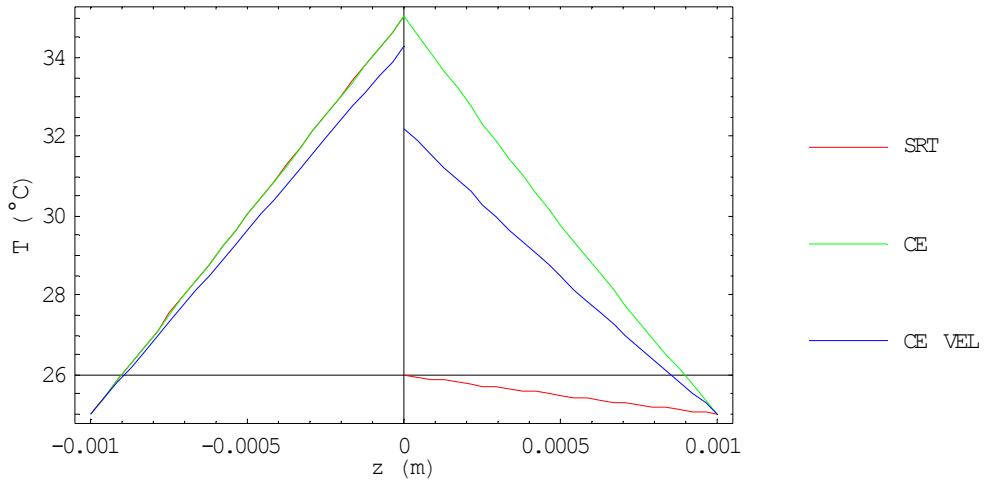

Figure 8.2: Condensation liquid and vapor temperatures verses position

We conclude that for equal boundary temperatures, the SRT, and CEVEL models predict $T_v > T_l$ for evaporation, and $T_v < T_l$ for condensation, whereas the CE model predicts almost no temperature jump. All models show that the liquid and vapor conductive energy fluxes are towards the interface for evaporation, and away from the interface for evaporation.

The evaporative temperature jump ($T_v > T_l$), and gradient (conductive flux towards the interface) directions agree with the Ward, Fang, and Stanga experiments [2], [3], [4] For condensation Ward and Stanga [4] find $T_v > T_l$ which is opposite to what we see in Figure 8.2. Comparing Figures 1.2, and 8.2 we notice that Ward and Stanga 's condensation vapor temperature gradient is in the opposite direction to ours. We suggest the vapor temperature gradient and temperature jump are linked, as pointed out by Kjelstrup et al. [34]. The use of the IT conductive heat flux (3.8) in the SRT model forces this relation; the CEVEL model has no such forcing, yet it behaves similarly to the SRT model. We investigate this further in the following Sections.

The steady state evaporation or condensation, for equal boundary temperatures $T_{bl} = T_{bv} = T_b$, is established based on the relation between the boundary temperature and the vapor pressure saturation temperature. Thus we could have achieved the same variation between evaporation and condensation by increasing or decreasing the liquid and vapor boundary temperature T_b,

relative to a constant vapor pressure.

8.2 Sensitivity to Liquid and Vapor Depth

We investigate the sensitivity of the interface temperatures, and fluxes to variations in the liquid and vapor depths L_l, and L_v. The analysis is performed using the SRT (3.13) (3.8), CE (4.16) (4.20), and CEVEL (4.71) (4.74) (4.75) models. Where coefficient values are required, we use those found from the data fitting in the previous chapter, Tables 6.2, 6.3, and 6.4.

We use the symmetric input parameters from Table 8.2 with a vapor pressure $p_v = 2.339\,\text{kPa}$ as a base point from which we vary L_l, and L_v, from the base value of $1 \times 10^{-3}\,\text{m}$ to $1\,\text{m}$.

L_l (m)	L_v (m)	T_{bl} (°C)	T_{bv} (°C)
1×10^{-3}	1×10^{-3}	25	25

Table 8.2: Symmetric temperature boundary conditions

Tables 8.3, 8.4, and 8.5 give the resulting interface temperatures and fluxes from the three models.

L_l (m)	L_v (m)	T_l (°C)	T_v (°C)	$j\ \left(\frac{\text{kg}}{\text{m}^2\,\text{s}}\right)$	$Q\ \left(\frac{\text{W}}{\text{m}^2}\right)$
1×10^{-3}	1×10^{-3}	20.0	24.4	1.12×10^{-3}	2733
1	1×10^{-3}	20.0	24.4	4.3×10^{-6}	2.702
1×10^{-3}	1	20.0	20.0	1.12×10^{-3}	2736

Table 8.3: SRT interface temperatures and fluxes variation with liquid and vapor depths

L_l (m)	L_v (m)	T_l (°C)	T_v (°C)	$j\ \left(\frac{\text{kg}}{\text{m}^2\,\text{s}}\right)$	$Q\ \left(\frac{\text{W}}{\text{m}^2}\right)$
1×10^{-3}	1×10^{-3}	20.0	20.0	1.15×10^{-3}	2735
1	1×10^{-3}	20.0	20.0	2.96×10^{-5}	2.45
1×10^{-3}	1	20.0	20.0	1.12×10^{-3}	2735

Table 8.4: CE interface temperatures and fluxes variation with liquid and vapor depths

L_l (m)	L_v (m)	T_l (°C)	T_v (°C)	$j\ \left(\frac{\text{kg}}{\text{m}^2\,\text{s}}\right)$	$Q\ \left(\frac{\text{W}}{\text{m}^2}\right)$
1×10^{-3}	1×10^{-3}	20.7	22.2	9.80×10^{-4}	2355
1	1×10^{-3}	20.0	21.9	1.88×10^{-5}	2.55
1×10^{-3}	1	20.6	20.6	9.96×10^{-4}	2360

Table 8.5: CEVEL interface temperatures and fluxes variation with liquid and vapor depths

We see a significant drop in mass and energy flux when L_l is increased, and only small variations in fluxes with increases in L_v. This indicates that the fluxes are more dependant on the liquid thermal conditions, than those of the vapor. The likely reason is that the liquid thermal conductivity is an order of magnitude higher than the vapor thermal conductivity.

The liquid interface temperatures are almost constant near the vapor pressure saturation temperature $T_{sat}\,(2.339\,\text{kPa}) = 20\,^{\circ}\text{C}$ for each model. This supports the claim that the liquid interface temperature is closely related to the vapor pressure saturation temperature. It also suggests that it is independent of the temperature boundaries. To support this claim, we investigate the effects of unequal boundary temperatures in the next section .

8.3 Different Liquid and Vapor Boundary Temperatures

We show that changing the boundary temperatures can alter the direction of the temperature gradients, without necessarily altering the flux directions. The analysis is performed using the SRT (3.13) (3.8), CE (4.16) (4.20), and CEVEL (4.71) (4.74) (4.75) models. Where coefficient values are required, we use those found from the data fitting in the previous chapter, Tables 6.2, 6.3, and 6.4.

We use the symmetric input parameters from Table 8.6 with a vapor pressure $p_v = 2.339\,\text{kPa}$ as a base point from which we vary T_{bl}, and T_{bv}, between $10\,^{\circ}\text{C}$ and $25\,^{\circ}\text{C}$.

L_l (m)	L_v (m)	T_{bl} (°C)	T_{bv} (°C)
1×10^{-3}	1×10^{-3}	25	25

Table 8.6: Symmetric temperature boundary conditions

Table 8.7 gives the models interface temperatures and fluxes, for variation of the boundary temperatures T_{bl} and T_{vl} between 25 °C and 10 °C.

Model	T_{bl} (°C)	T_{bv} (°C)	T_l (°C)	T_v (°C)	$j\ \left(\frac{\text{kg}}{\text{m}^2\,\text{s}}\right)$	$Q\ \left(\frac{\text{W}}{\text{m}^2}\right)$
SRT	25	25	20.0	24.4	1.12×10^{-3}	2733
	20	25	20.0	24.5	1.89×10^{-6}	−3.19
	10	25	20.0	20.0	-2.21×10^{-3}	−5407
	25	20	20.0	20.0	1.12×10^{-3}	2736
	25	10	20.0	11.2	1.12×10^{-3}	2726
CE	25	25	20.0	20.0	1.15×10^{-3}	2735
	20	25	20.0	20.0	2.81×10^{-5}	−1.05
	10	25	20.0	20.0	-2.18×10^{-3}	−5405
	25	20	20.0	20.0	1.12×10^{-3}	2735
	25	10	20.0	20.0	1.07×10^{-3}	2736
CEVEL	25	25	20.7	22.2	9.80×10^{-4}	2355
	20	25	20.0	21.9	1.49×10^{-5}	−6.99
	10	25	18.6	21.4	1.88×10^{-3}	−4638
	25	20	20.7	20.4	9.66×10^{-4}	2361
	25	10	20.7	16.8	9.37×10^{-4}	2373

Table 8.7: Sensitivity of interface conditions to different boundary temperatures

The liquid interface temperatures are nearly constant for variations of the boundary temperatures. This verifies our earlier suggestion that the liquid interface temperature is almost independent of the liquid and vapor boundary conditions. We conclude that the liquid interface temperature is always close to the vapor pressure saturation temperature, and is thus largely determined by the vapor pressure.

We now examine the temperature profiles. First the liquid boundary temperature is perturbed to $T_{bl} = 20\,°\text{C}$, which is the saturation temperature for the prescribed vapor pressure $p_v = 2.339\,\text{kPa}$ [56]. Figure 8.3 shows that is results in a near horizontal liquid temperature

gradient. Table 8.7 shows this results in small mass and energy fluxes. We have almost achieved equilibrium by setting T_{bl} close to the liquid interface temperature, the fluxes are now almost completely due to the vapor temperature gradient. This is a similar effect to what we observed when the liquid boundary temperature was moved far from the interface, Tables 8.3, 8.4, and 8.5. We conclude, as we did before, that the liquid temperature gradient plays a significant role in determining the fluxes. We also suggest this implies that much of the heat supplied for evaporation comes through the liquid.

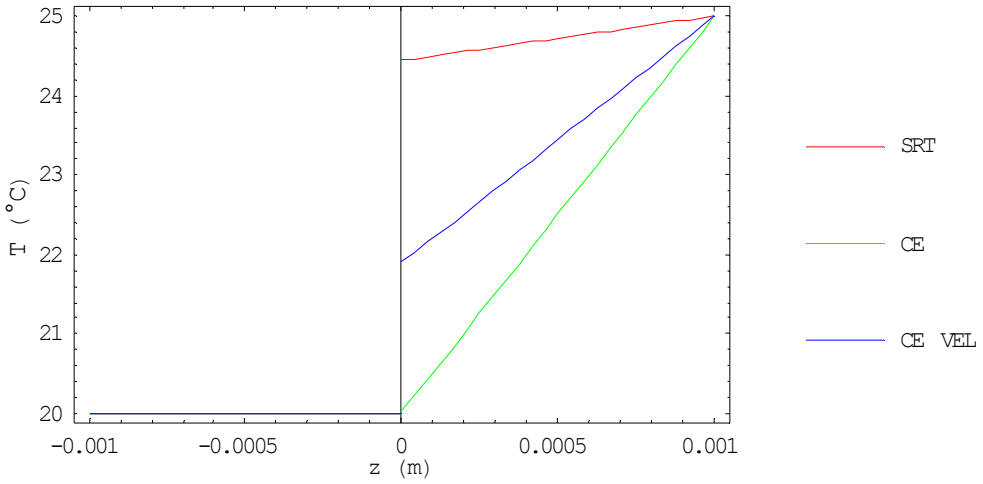

Figure 8.3: Liquid and vapor temperature profiles, $T_{bl} = 20\,^{\circ}\mathrm{C}$, $T_{bv} = 25\,^{\circ}\mathrm{C}$

For $T_{bl} = 10\,^{\circ}\mathrm{C}$ condensation ($j < 0$) is observed. This indicates that the relation between the liquid boundary temperature and the vapor pressure saturation temperature is a strong determination if condensation or evaporation will occur. In Figure 8.4 the liquid temperature gradients are positive; they agree with the direction we saw for condensation with equal boundary temperatures, Figure 8.2. The vapor temperature gradients are forced to be positive because of the vapor boundary temperature. The energy flux becomes negative because the liquid and vapor conductive heat fluxes operate in the same negative direction as the convective heat flux.

In Figure 8.4 the direction of the SRT and CEVEL temperature jumps is positive, $T_v > T_l$, even though we have condensation. This stands in agreeance with Ward and Stanga [4]. The

direction of the SRT temperature jump is due to the IT conductive energy flux, Eqn. (3.8), which can be rearranged with Fourier's law (2.51) to read

$$\frac{dT_v}{dz} = \frac{\alpha}{\kappa_v}\left(\frac{T_v - T_l}{T_l T_v}\right). \tag{8.1}$$

Thus, for positive vapor temperature gradients, the vapor interface temperature must be greater than the liquid interface temperature. The opposite is true for negative gradients. It is significantly more difficult to isolate the temperature gradient in the CEVEL model (4.71), (4.74), (4.75). We suffice by pointing out that until now it agrees with the temperature jump directions predicted by the IT conductive heat flux (3.8); thus it also seems to be dependant on the sign of the vapor temperature gradient.

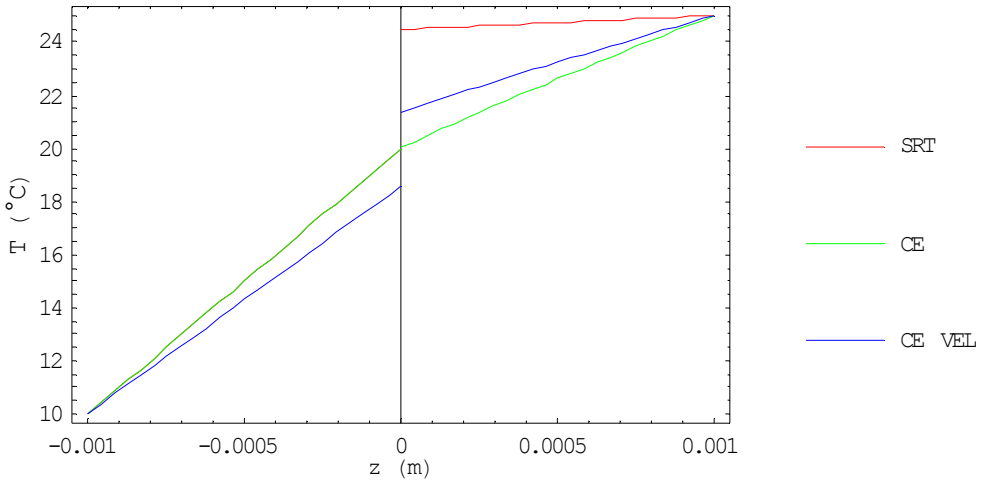

Figure 8.4: Liquid and vapor temperature profiles, $T_{bl} = 10\,^{\circ}\mathrm{C}$, $T_{bv} = 25\,^{\circ}\mathrm{C}$

Next we set the liquid boundary temperature back to 25 °C, and set the vapor boundary temperature to 20 °C, Figure 8.5. Table 8.7 shows this has little effect on the mass and energy fluxes, as we observed earlier with the adjustment of the vapor boundary depth, Tables 8.3, 8.4, and 8.5 This again supports our claim that the liquid temperature gradient has a much greater influence on the fluxes, than that of the vapor.

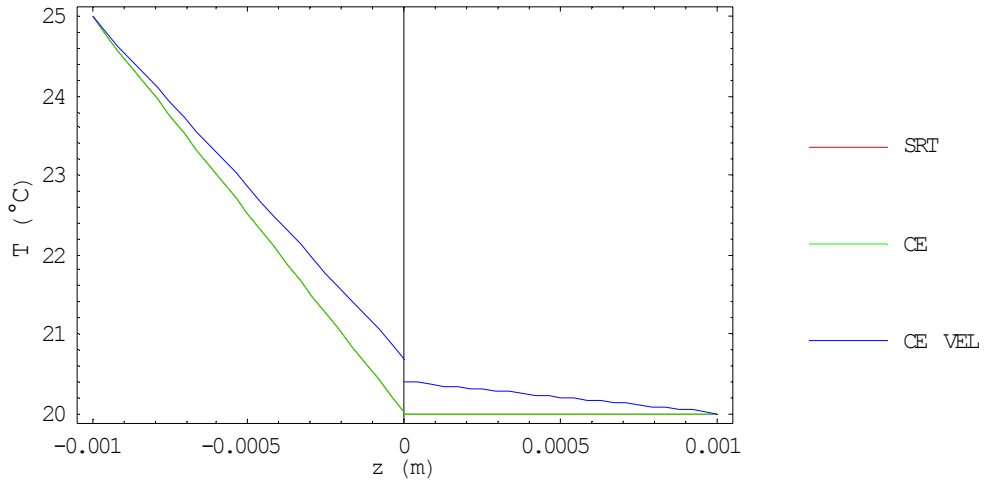

Figure 8.5: Liquid and vapor temperature profiles, $T_{bl} = 25\,^{\circ}\mathrm{C}$, $T_{bv} = 20\,^{\circ}\mathrm{C}$

Figure 8.5 shows the SRT model's near zero temperature jump, caused by the near zero vapor temperature gradient. The temperature gradient and jump of the CEVEL model are reversed from that of the previous figures, even though we still have evaporation. Considering this and the observations we made for condensation in Figure 8.4 we conclude that the CEVEL temperature jump direction, like the IT conductive heat flux (3.8), is also directly dependant on the direction of the vapor temperature gradient.

Figure 8.6 is the result of setting $T_{bv} = 10\,^{\circ}\mathrm{C}$, and maintaining $T_{bl} = 25\,^{\circ}\mathrm{C}$. The vapor temperature profiles are now reversed, but we see from Table 8.7 that evaporation is still predicted, and the mass flux has only decreased slightly from $T_{bv} = 20\,^{\circ}\mathrm{C}$. Reducing T_{bv} lowers the evaporative forcing by increasing the magnitude of the vapor temperature gradient, increasing the conductive flux in vapor away from the interface, thus decreasing the evaporative mass flux. The energy flux increases slightly, since the inverted vapor temperature profile aligns the liquid and vapor conductive energy fluxes with the convective energy flux.

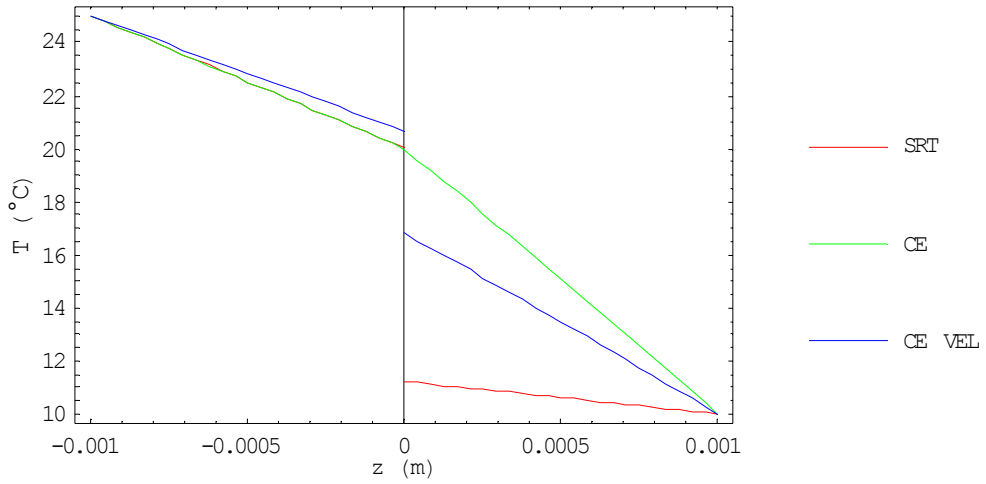

Figure 8.6: Liquid and vapor temperature profiles, $T_{bl} = 25\,^{\circ}\mathrm{C}$, $T_{bv} = 10\,^{\circ}\mathrm{C}$

Figure 8.6 shows the increased negative temperature jump of the SRT, and CEVEL models, which coincides with an increased magnitude of the negative vapor temperature gradient.

Since the direction of the vapor temperature gradient can be in both directions for either condensation or evaporation, we conclude that the relation between the liquid boundary temperature and the vapor pressure saturation temperature is the main factor in the determination of evaporation or condensation. If $T_{bl} > T_{sat}(p_v)$ there is a strong evaporative forcing, if $T_{bl} < T_{sat}(p_v)$ there is a strong condensation forcing. This coincides with the conductive heat flux in the liquid q_l flowing toward the interface, delivering heat for evaporation, and away from the interface removing heat for condensation. The relation of the vapor boundary temperature to the vapor pressure saturation temperature plays a role in the direction of forcing, but does not have the influence of the liquid. $T_{bv} > T_{sat}(p_v)$ causes evaporative forcing, and $T_{bl} < T_{sat}(p_v)$ results in condensation forcing, but if in either case the liquid boundary temperature forcing is in the opposite direction the mass flux will be in the direction of the liquid boundary temperature forcing.

The temperature jumps of the SRT and CEVEL models both behave similarly, showing that $T_v > T_l$ when the vapor conductive heat flux q_v flows toward the interface, and $T_v < T_l$ when q_v flows away from the interface, independent of if there is condensation or evaporation. Also

as the magnitude of q_v is increased the magnitude of the temperature jump increases. Thus we conclude that the temperature jump is independent of the direction of the mass flux, and is directly dependant on the direction and magnitude of q_v.

Chapter 9

Analysis of Assumptions

We check the effects and validity of the assumptions involved in the equation derivations. The sensitivity of models to specific heats and thermal conductivities is investigated, and the assumption of constant vapor pressure is confirmed.

We use the experimental data from Table 6.1 with the SRT (3.13) (3.8), the CE (4.16) (4.20), and the CEVEL (4.71) (4.74) (4.75) models. We use the coefficients found from the earlier data fitting in Tables 6.3, and 6.4.

9.1 Constant Specific Heats of the Vapor and Liquid

In our models we use the kinetic theory monatomic gas specific heat, $c_p = \frac{5}{2}\frac{k}{m} = 1.15\frac{\text{kJ}}{\text{kg K}}$. The water vapor specific heat is $c_p = 1.865\frac{\text{kJ}}{\text{kg K}}$ [56]. Tables 9.1, 9.2, and 9.3 show the SRT, CE, and CEVEL result variation with specific heat. We calculate pure differences for the interface temperatures, and percent differences for the fluxes.

$c_p\ \left(\frac{\text{kJ}}{\text{kg K}}\right)$	T_l (°C)	T_v (°C)	$j\ \left(\frac{\text{kg}}{\text{m}^2\,\text{s}}\right)$	$Q\ \left(\frac{\text{W}}{\text{m}^2}\right)$
1.15	−0.329	2.67	1.19×10^{-3}	2861
1.865	−0.416	1.03	1.20×10^{-3}	2869
38.5%	0.087 °C	1.64 °C	0.985%	0.309%

Table 9.1: SRT model sensitivity to vapor specific heat

$c_p\ \left(\frac{\text{kJ}}{\text{kg K}}\right)$	T_l (°C)	T_v (°C)	$j\ \left(\frac{\text{kg}}{\text{m}^2\,\text{s}}\right)$	$Q\ \left(\frac{\text{W}}{\text{m}^2}\right)$
1.15	−0.330	−0.385	1.19×10^{-3}	2861
1.865	−0.411	−0.659	1.20×10^{-3}	2869
38.5%	0.081 °C	0.274 °C	0.930%	0.287%

Table 9.2: CE model sensitivity to vapor specific heat

$c_p\ \left(\frac{\text{kJ}}{\text{kg K}}\right)$	T_l (°C)	T_v (°C)	$j\ \left(\frac{\text{kg}}{\text{m}^2\,\text{s}}\right)$	$Q\ \left(\frac{\text{W}}{\text{m}^2}\right)$
1.15	2.01	2.67	1.08×10^{-3}	2612
1.865	0.883	−9.76	1.11×10^{-3}	2613
38.5%	1.127 °C	12.43 °C	2.66%	4.11×10^{-2}%

Table 9.3: CEVEL model sensitivity to vapor specific heat

The mass and energy fluxes do not change greatly, less than 1%. In all cases the interface temperatures fall. The change is small for the CE model. The SRT T_v falls by over 1 °C, however the temperature jump direction is unchanged. The SRT vapor interface temperature change with specific heat could be offset by decreasing the conductive energy flux (3.8) phenomenological coefficient α. The most striking change is the CEVEL model, where T_v falls by over 10 °C and T_l falls by over 1 °C, reversing the interface temperature jump direction. Unlike the SRT model this change can not be rectified by adjusting ψ and ω.

We recall that the CEVEL model, like all the kinetic theory models is derived based on the assumption of a monatomic vapor, which requires the specific heat to be $c_p = \frac{5}{2}\frac{k}{m}$. To properly include the true value for the water specific heat into the model, the additional degrees of freedom for the water molecule would need to be accounted for.

The specific heat of liquid water varies between $4.23\frac{\text{kJ}}{\text{kg K}}$ and $4.18\frac{\text{kJ}}{\text{kg K}}$ over a temperature range of 273 K to 298 K [56]. Tables 9.4, 9.5, and 9.6 give the variation in the SRT, CE, and CEVEL model results for the range of liquid specific heat values.

$c_l \left(\frac{\text{kJ}}{\text{kg K}}\right)$	T_l (°C)	T_v (°C)	$j \left(\frac{\text{kg}}{\text{m}^2\,\text{s}}\right)$	$Q \left(\frac{\text{W}}{\text{m}^2}\right)$
4.18	-0.329	2.67	1.19×10^{-3}	2861
4.23	-0.323	2.67	1.18×10^{-3}	2859
1.20%	0.006 °C	0.00 °C	4.65×10^{-2}%	4.64×10^{-2}%

Table 9.4: SRT model sensitivity to liquid specific heat

$c_l \left(\frac{\text{kJ}}{\text{kg K}}\right)$	T_l (°C)	T_v (°C)	$j \left(\frac{\text{kg}}{\text{m}^2\,\text{s}}\right)$	$Q \left(\frac{\text{W}}{\text{m}^2}\right)$
4.18	-0.330	-0.385	1.19×10^{-3}	2861
4.23	-0.324	-0.379	1.19×10^{-3}	2859
1.20%	0.006 °C	0.006 °C	4.65×10^{-2}%	4.64×10^{-2}%

Table 9.5: CE model sensitivity to liquid specific heat

$c_l \left(\frac{\text{kJ}}{\text{kg K}}\right)$	T_l (°C)	T_v (°C)	$j \left(\frac{\text{kg}}{\text{m}^2\,\text{s}}\right)$	$Q \left(\frac{\text{W}}{\text{m}^2}\right)$
4.18	2.01	2.67	1.08×10^{-3}	2612
4.23	2.01	2.67	1.08×10^{-3}	2611
1.20%	0.00 °C	0.00 °C	3.88×10^{-2}%	3.89×10^{-2}%

Table 9.6: CEVEL model sensitivity to liquid specific heat

We conclude, that the use of the monatomic specific heat will not alter the conclusions obtained from the SRT and CE models, however does significantly alter the findings from the CEVEL model. The CEVEL results using the monatomic specific heat are still of great interest, but the model's great sensitivity to specific heat implies that it might require the inclusion of additional degrees of freedom. Here, it must be kept in mind that inclusion of more degrees of freedom will also change the expressions for j, and Q. Nothing definitive on the influence of the inclusion of additional degrees of freedom can be concluded without proper expressions for j, and Q.

The liquid specific heat variation over the specified temperature range has an insignificant effect on the interface temperatures and fluxes.

9.2 Constant Vapor and Liquid Thermal Conductivities

The water vapor thermal conductivity varies between $1.56 \times 10^{-2} \frac{\mathrm{W}}{\mathrm{m\,K}}$ and $1.81 \times 10^{-2} \frac{\mathrm{W}}{\mathrm{m\,K}}$ over a temperature range of 273 K to 298 K [57]. From Tables 9.7, 9.8, and 9.9 the variation in interface temperatures and fluxes with vapor thermal conductivity is small.

$\kappa_v \left(\frac{\mathrm{W}}{\mathrm{m\,K}}\right)$	T_l (°C)	T_v (°C)	$j \left(\frac{\mathrm{kg}}{\mathrm{m^2\,s}}\right)$	$Q \left(\frac{\mathrm{W}}{\mathrm{m^2}}\right)$
1.81×10^{-2}	-0.330	4.36	1.18×10^{-3}	2860
1.56×10^{-2}	-0.328	3.33	1.18×10^{-3}	2860
13.8%	0.002 °C	1.03 °C	1.02×10^{-2}%	7.69×10^{-3}%

Table 9.7: SRT model sensitivity to vapor thermal conductivity

$\kappa_v \left(\frac{\mathrm{W}}{\mathrm{m\,K}}\right)$	T_l (°C)	T_v (°C)	$j \left(\frac{\mathrm{kg}}{\mathrm{m^2\,s}}\right)$	$Q \left(\frac{\mathrm{W}}{\mathrm{m^2}}\right)$
1.81×10^{-2}	-0.330	-0.381	1.19×10^{-3}	2861
1.56×10^{-2}	-0.330	-0.383	1.19×10^{-3}	2861
13.8%	0.000 °C	0.002 °C	0.168%	1.75×10^{-3}%

Table 9.8: CE model sensitivity to vapor thermal conductivity

$\kappa_v \left(\frac{\mathrm{W}}{\mathrm{m\,K}}\right)$	T_l (°C)	T_v (°C)	$j \left(\frac{\mathrm{kg}}{\mathrm{m^2\,s}}\right)$	$Q \left(\frac{\mathrm{W}}{\mathrm{m^2}}\right)$
1.81×10^{-2}	2.01	3.22	1.08×10^{-3}	2611
1.56×10^{-2}	2.01	2.88	1.08×10^{-3}	2612
13.8%	0.00 °C	0.34 °C	6.46×10^{-2}%	8.04×10^{-3}%

Table 9.9: CEVEL model sensitivity to vapor thermal conductivity

The liquid water thermal conductivity varies between $0.555 \frac{\mathrm{W}}{\mathrm{m\,K}}$ and $0.609 \frac{\mathrm{W}}{\mathrm{m\,K}}$ over a temperature range of 273 K to 298 K [57]. Tables 9.10, 9.11, and 9.12 show the model variation with liquid thermal conductivity. The liquid thermal conductivity variation causes insignificant changes in the interface temperatures. The mass and energy fluxes change more significantly than we observed with variation of the other constants. This sensitivity might suggest that a significant portion of the heat supplied to the interface comes from the liquid, due to its higher thermal

conductivity as compared to the vapor. Although the flux percent differences can not be ignored, they are still small enough to not alter our conclusions.

κ_l $\left(\frac{\mathrm{W}}{\mathrm{m\,K}}\right)$	T_l (°C)	T_v (°C)	j $\left(\frac{\mathrm{kg}}{\mathrm{m^2\,s}}\right)$	Q $\left(\frac{\mathrm{W}}{\mathrm{m^2}}\right)$
0.555	−0.329	2.67	1.19×10^{-3}	2861
0.609	−0.328	2.35	1.31×10^{-3}	3167
10.7%	0.001 °C	0.32 °C	10.7%	10.72%

Table 9.10: SRT model sensitivity to liquid thermal conductivity

κ_l $\left(\frac{\mathrm{W}}{\mathrm{m\,K}}\right)$	T_l (°C)	T_v (°C)	j $\left(\frac{\mathrm{kg}}{\mathrm{m^2\,s}}\right)$	Q $\left(\frac{\mathrm{W}}{\mathrm{m^2}}\right)$
0.555	−0.330	−0.385	1.19×10^{-3}	2861
0.609	−0.328	−0.390	1.31×10^{-3}	3167
10.7%	0.002 °C	0.005 °C	10.7%	10.7%

Table 9.11: CE model sensitivity to liquid thermal conductivity

κ_l $\left(\frac{\mathrm{W}}{\mathrm{m\,K}}\right)$	T_l (°C)	T_v (°C)	j $\left(\frac{\mathrm{kg}}{\mathrm{m^2\,s}}\right)$	Q $\left(\frac{\mathrm{W}}{\mathrm{m^2}}\right)$
0.555	2.01	2.67	1.08×10^{-3}	2612
0.609	2.22	2.75	1.19×10^{-3}	2867
10.7%	0.21 °C	0.08 °C	3.37%	9.76%

Table 9.12: CEVEL model sensitivity to liquid thermal conductivity

In conclusion, the vapor thermal conductivity has little effect on the model results, while the liquid thermal conductivity has no measurable effect on the interface temperatures, but does modestly affect the fluxes, indicating the significance of the liquid conductive heat flux for evaporation and condensation. These variations are still not significant enough to alter any of our findings.

9.3 Constant Vapor Pressure

We assume the pressure is uniform throughout the vapor. We now use the one-dimensional mass (2.2) and momentum balances (2.12), with the ideal gas law to show that this assumption is valid.

We start with the mass balance (2.2),

$$\frac{\partial \rho_v v_z}{\partial z} = 0,$$

and rearrange it to read

$$\frac{\partial v_z}{\partial z} = -v_z \frac{\partial \ln \rho_v}{\partial z}. \tag{9.1}$$

We now rewrite the ideal gas law

$$\rho_v = \frac{p_v}{R T_v(z)} \tag{9.2}$$

as

$$\ln \rho_v = \ln p_v - \ln T_v(z) - \ln R. \tag{9.3}$$

Substituting Eqn. (9.3) into Eqn. (9.1), and recalling that $j = \rho_v v_z$ we find

$$\frac{\partial v_z}{\partial z} = -\frac{j}{\rho_v}\left(\frac{\partial \ln p_v}{\partial z} - \frac{\partial \ln T_v(z)}{\partial z}\right). \tag{9.4}$$

The one-dimensional momentum balance gives us

$$\frac{\partial p_v}{\partial z} = \rho_v g - j\frac{\partial v_z}{\partial z}. \tag{9.5}$$

Inserting Eqn. (9.4) and rearranging results in

$$\frac{\partial p_v}{\partial z} = \frac{\rho_v g - \frac{j^2}{\rho_v}\frac{1}{T_v(z)}\frac{\partial T_v}{\partial z}}{1 - \frac{j^2}{\rho_v p_v}}. \tag{9.6}$$

We now calculate the pressure gradient from Eqn. (9.6), using the SRT and CE model results. The vapor pressure used in the experimental data, Table 6.1, is $p_v = 593\,\mathrm{Pa}$, which we take as the vapor pressure at the interface. The models give us the vapor interface temperatures, and

interface temperature gradients. We calculate the vapor density using the ideal gas law with the prescribed interface vapor pressure, and calculated interface temperature. The resulting interface pressure gradients are: from the SRT model $\frac{\partial p_v}{\partial z} = 4.52 \times 10^{-2} \frac{\mathrm{Pa}}{\mathrm{m}}$, and the CE model $\frac{\partial p_v}{\partial z} = 4.56 \times 10^{-2} \frac{\mathrm{Pa}}{\mathrm{m}}$. We also calculated the gradients at the vapor temperature boundary $z = L_{bv}$, and found for the SRT model $\frac{\partial p_v}{\partial z} = 3.92 \times 10^{-2} \frac{\mathrm{Pa}}{\mathrm{m}}$, and the CE model $\frac{\partial p_v}{\partial z} = 3.88 \times 10^{-2} \frac{\mathrm{Pa}}{\mathrm{m}}$. The depth of the vapor from Table 6.1 is $L_{bv} = 18.6 \times 10^{-3}\,\mathrm{m}$, this corresponds to a maximum pressure change of the order of $10^{-4}\,\mathrm{Pa}$. We conclude that it is very accurate to assume a constant vapor pressure for our system.

Chapter 10

Spherical Geometry

Up until now we have considered a planar geometry, see Figure 1.3. This is a simplification of the Ward, Fang, and Stanga experiments [2], [3], [4]. We now investigate the effects of interface surface shape. Ward, Fang, and Stanga [2], [3], [4] suggest that their experimental interface can be modelled as hemisphere, see Figure 1.1. In keeping with our simple one-dimensional approach we suggest that the hemispherical shape can be approximated using a spherical interface, with one-dimensional radial fluxes, jumps, and gradients.

10.1 Spherical Model Geometry

The problem is redefined with spherical geometry, see Figure 10.1.

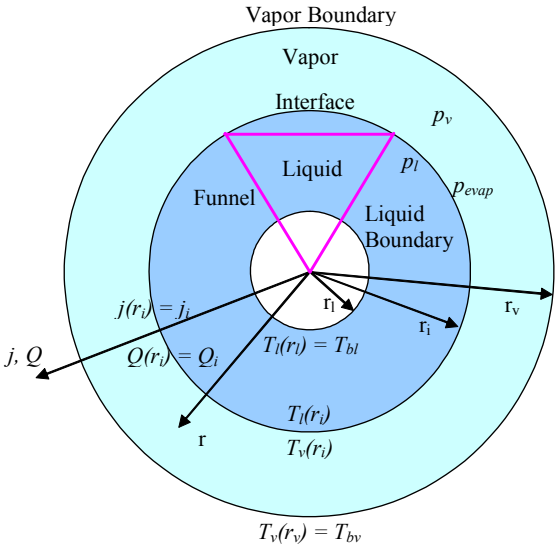

Figure 10.1: Spherical model geometry

The liquid temperature boundary at radius r_l is the inner most ring. The middle ring is the liquid vapor interface, at r_i and the outermost ring is the vapor temperature boundary, at r_v. We use the same notation as before for the boundary temperatures so that the liquid boundary temperature is T_{bl}, and the vapor boundary temperature is T_{bv}. The liquid and vapor interface temperatures are $T_l(r_i)$, and $T_v(r_i)$ respectively. We designate the interface mass flux and energy fluxes as j_i, and Q_i. The radial fluxes, and gradients are defined as positive for the outward direction. We again note, that the pressure of the evaporating molecules leaving the surface is p_{evap}.

In Figure 10.1 we have drawn in the funnel from the Ward, Fang, and Stanga experimental apparatus, Figure 1.1.

10.2 Spherical Liquid and Vapor Temperature Profiles

We assume only one-dimensional radial fluxes, gradients, and jumps.

The differential balance of mass in spherical coordinates is

$$\frac{1}{r^2}\frac{d}{dr}\left(r^2 j_r\right) = 0 \tag{10.1}$$

Applying the interface boundary condition $j_r(r_i) = j_i$ the radial mass flux is

$$j_r(r) = \frac{j_i r_i^2}{r^2}. \tag{10.2}$$

The differential balance of energy in spherical coordinates reads

$$\frac{1}{r^2}\frac{d}{dr}\left(j_r h + q_r\right) = 0. \tag{10.3}$$

We recall the definition of total energy flux, as the combination of the convective, and conductive energy fluxes,

$$Q_r = j_r h + q_r. \tag{10.4}$$

Eqn. (10.3) with the spherical energy flux becomes

$$\frac{1}{r^2}\frac{d}{dr}\left(r^2 Q_r\right) = 0, \tag{10.5}$$

which like the mass flux, can be solved using the interface condition $Q_r\left(r_i\right) = Q_i$ to be

$$Q_r\left(r\right) = \frac{Q_i r_i^2}{r^2}. \tag{10.6}$$

We expand Eqn. (10.3) by inserting the constant specific heat vapor enthalpy (2.37) and Fourier's law (2.51), and find

$$c_p j_r \frac{dT_v}{dr} - \frac{1}{r^2}\frac{d}{dr}\left(r^2 \kappa_v \frac{dT_v}{dr}\right) = 0. \tag{10.7}$$

We substitute for the radial mass flux using Eqn. (10.2), and get

$$\frac{d^2 T_v}{dr^2} + \left(\frac{2}{r} - \frac{j_i r_i^2 c_p}{r^2 \kappa_v}\right)\frac{dT_v}{dr} = 0. \tag{10.8}$$

To solve the differential equation the function $f\left(r\right) = \frac{dT_v}{dr}$ is introduced, and we find

$$f\left(r\right) = \frac{dT_v}{dr} = \frac{A}{r^2}\exp\left(\frac{-j_i r_i^2 c_p}{r\kappa_v}\right). \tag{10.9}$$

Integrating again gives us the vapor radial temperature profile,

$$T_v\left(r\right) = \frac{A\kappa_v}{j_i r_i^2 c_p}\exp\left(\frac{-j_i r_i^2 c_p}{r\kappa_v}\right) + B, \tag{10.10}$$

where A and B are constants of integration.

The vapor boundary temperature

$$T_v\left(r_v\right) = T_{bv} \tag{10.11}$$

is one boundary condition. The second boundary condition is found by substituting the radial energy flux (10.4), with Fourier's law (2.51), and the radial mass flux (10.2), into Eqn. (10.6),

and solving for the radial temperature gradient at the vapor boundary $r = r_v$,

$$\frac{dT_r}{dr}(r_v) = \frac{\frac{j_i r_i^2}{r_v^2}\left(c_p\left(T_{bv} - T_o\right) + \Delta h_o\right) - \frac{Q_i r_i^2}{r_v^2}}{\kappa_v}. \tag{10.12}$$

Applying the boundary conditions we find

$$A = \frac{j_i r_i^2 c_p}{\kappa_v}\left(T_{bv} - T_{cv}\right)\exp\left(\frac{-j_i r_i^2 c_p}{\kappa_v r_v}\right), \tag{10.13}$$

and

$$B = T_{bv} - \left(T_{bv} - \frac{Q_i}{j_i c_p} + T_o - \frac{\Delta h_o}{c_p}\right)\exp\left(\frac{-j_i r_i^2 c_p}{\kappa_v r_v}\right). \tag{10.14}$$

Simplifying the integration constants, and substituting them into Eqn. (10.10) yields the spherical vapor temperature distribution,

$$T_v(r) = T_{cv} + \left(T_{bv} - T_{cv}\right)\exp\left(\frac{r - r_v}{r r_v a_v}\right), \tag{10.15}$$

with similar temperature constants to the planar case,

$$T_{cv} = \frac{Q_i}{j_i c_p} + T_o - \frac{\Delta h_o}{c_p}, \qquad a_v = \frac{\kappa_v}{j_i r_i^2 c_p}. \tag{10.16}$$

The procedure for deriving the spherical liquid temperature profile is identical, resulting in

$$T_l(r) = T_{cl} + \left(T_{bl} - T_{cl}\right)\exp\left(\frac{r - r_l}{r r_l a_l}\right), \tag{10.17}$$

with constants of

$$T_{cl} = \frac{Q_i}{j_i c_l} + T_o, \quad a_l = \frac{\kappa_l}{j_i r_i^2 c_l}. \tag{10.18}$$

10.3 Spherical Results

The interface mass and energy flux expressions, and the saturation pressure expression remain the same for spherical coordinates. The change is in the temperature profile expressions; the

planar expressions: Eqns. (2.59), (2.60), (2.53), and (2.54), are replaced by spherical expressions, Eqns. (10.17), (10.15), (10.18), and (10.16).

For the simulations we use the input parameters from the experimental data in Table 6.1. The boundary temperatures are the same, but their depths must be converted to the spherical geometry The vapor boundary radius r_v is interface radius r_i plus the vapor depth, L_v. The interface radius is assumed to be equal to the radius of curvature R_o. The liquid boundary radius, r_l is the liquid depth L_l subtracted from the interface radius. The radius values are given below in Table 10.1. The radius of curvature is from Ward and Stanga 's experiment E1 [4].

Conversion	Radius (m)
$r_i = R_o$	6.088×10^{-3}
$r_v = r_i + L_v$	24.68×10^{-3}
$r_l = r_i - L_l$	1.118×10^{-3}

Table 10.1: Conversions from planar to radial, Ward et al. experiment E1

We use three models which are representative of their respective groups, the SRT (3.13) (3.8), CE (4.16) (4.20), and CEVEL (4.71) (4.74) (4.75) models, with coefficient values from Tables 6.3, and 6.4. We use the coefficient choices from the planar interface models since we wish to observe the changes in the interface conditions between spherical and planar interface geometries.

10.3.1 Interface Conditions

Table 10.2 gives the resulting spherical interface conditions.

Model	T_l (°C)	T_v (°C)	$j\ \left(\frac{\text{kg}}{\text{m}^2\,\text{s}}\right)$	$Q\ \left(\frac{\text{W}}{\text{m}^2}\right)$
SRT	-0.287	15.3	2.28×10^{-4}	524
CE	-0.342	-0.293	2.48×10^{-4}	524
CEVEL	0.192	8.21	2.33×10^{-4}	514

Table 10.2: Spherical interface conditions

For comparison the results for the planar interface are repeated in Table 10.3.

Model	T_l (°C)	T_v (°C)	$j\ \left(\frac{\text{kg}}{\text{m}^2\,\text{s}}\right)$	$Q\ \left(\frac{\text{W}}{\text{m}^2}\right)$
SRT	-0.329	2.67	1.18×10^{-3}	2861
CE	-0.330	-0.385	1.19×10^{-3}	2861
CEVEL	2.01	2.67	1.08×10^{-3}	2612

Table 10.3: Planar interface conditions

In the spherical geometry, mass and energy fluxes are an order of magnitude smaller than in the planar case. We also note the spherical mass flux is an order of magnitude smaller than the measured value in Table 6.1.

The liquid interface temperatures change only slightly between the planar and spherical geometries, see Tables 10.2, and 10.3. The vapor interface temperatures of the SRT, and CEVEL models are larger for spherical coordinates, because of their dependence on the vapor conductive heat flux, while the CE vapor interface temperature is almost unchanged.

The results further solidify our conclusions that the liquid interface temperature is largely dependant on the vapor pressure, by suggesting that it is almost independent of geometry, in addition to its independence from temperature boundary conditions. For the vapor interface temperature, we see from the SRT and CEVEL models that it is highly geometry dependant.

The CE model vapor interface temperature is largely independent of geometry, since it closely follows the vapor pressure saturation temperature.

10.3.2 Temperature Profiles

Figure 10.2 shows the spherical temperature profiles of the three models. The interface is at $r = 6.088 \times 10^{-3}$ m.

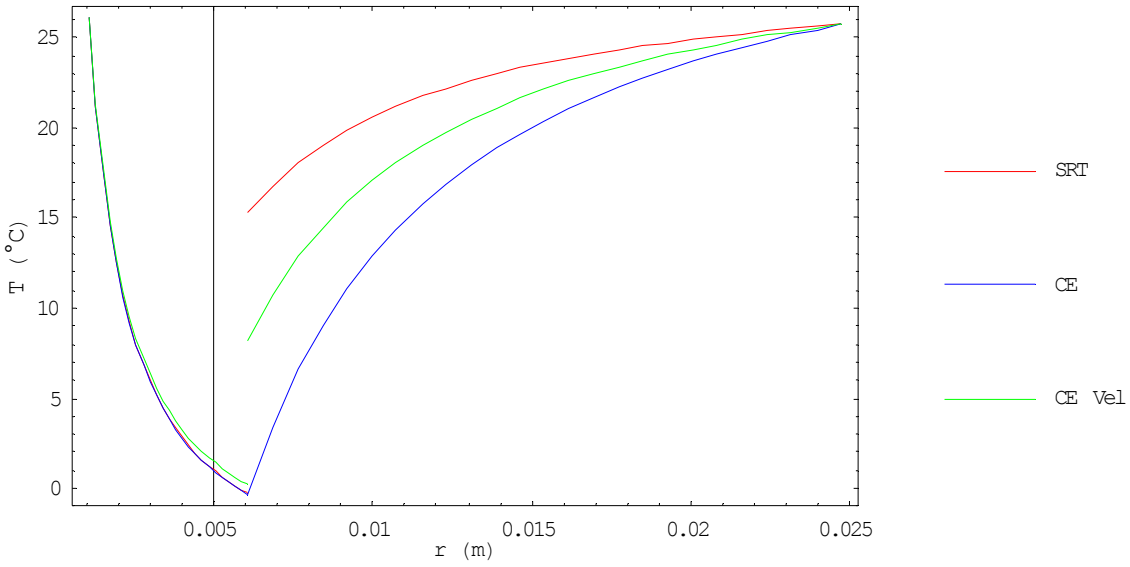

Figure 10.2: Spherical liquid and vapor temperature profiles

We compare Figure 10.2, and the planar temperature profiles, Figure 10.3.

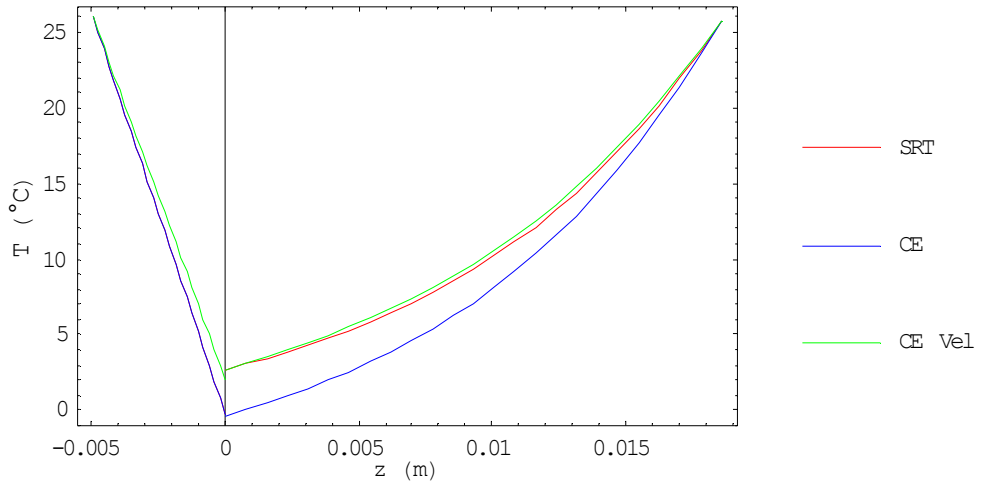

Figure 10.3: Planar liquid and vapor temperature profiles

We see that the spherical and planar temperature profiles are very different. In the liquid, the planar profile is close to linear, while the spherical is exponential. The vapor profiles are also different: we see the planar temperature gradient increases as we move deeper into the vapor, while the spherical gradient levels off. Interestingly, if we compare these results to the sample of Ward and Stanga 's results Figure 1.2, we see for evaporation that the planar liquid profile together with the spherical vapor profile are the best matches to the measured results.

Chapter 11

Additional Factors

We now address three supplemental factors which we have yet to mention, that arise from the Ward, Fang, and Stanga publications [2], [3], [4]: the effects of liquid water near the super cooled region, surface tension, and an observed isothermal zone in the liquid.

11.1 Properties of Super Cooled Liquid Water

The Ward and Stanga [4] experiments involve liquid water near $0\,^{\circ}\mathrm{C}$. Although their experiments do not go below $-1\,^{\circ}\mathrm{C}$, they still border on the super cooled liquid water region. We briefly discuss the variation of specific heat and thermal conductivity in this region.

The liquid water specific heat measured between $-10\,^{\circ}\mathrm{C}$ and $0\,^{\circ}\mathrm{C}$ varies from $4.3\frac{\mathrm{kJ}}{\mathrm{kg\,K}}$ to $4.2\frac{\mathrm{kJ}}{\mathrm{kg\,K}}$ [60]. Tables 9.4 and 9.5 show that there is a negligible effect on the results for variations between $4.23\frac{\mathrm{kJ}}{\mathrm{kg\,K}}$ and $4.18\frac{\mathrm{kJ}}{\mathrm{kg\,K}}$. We conclude the super cooled liquid water specific heat variation will have little effect on the model results.

We have already presented the liquid water thermal conductivity for $-3\,^{\circ}\mathrm{C}$, as $0.555\frac{\mathrm{W}}{\mathrm{m\,K}}$ [57]. Measurements report for a temperature range of $-10\,^{\circ}\mathrm{C}$ to $0\,^{\circ}\mathrm{C}$ the thermal conductivity moves from $0.5\frac{\mathrm{W}}{\mathrm{m\,K}}$, to $0.55\frac{\mathrm{W}}{\mathrm{m\,K}}$ [61]. We have already investigated the variation between $0.55\frac{\mathrm{W}}{\mathrm{m\,K}}$, to $0.609\frac{\mathrm{W}}{\mathrm{m\,K}}$, and found that the mass and energy fluxes change by about 10%, with negligible effect on the interface temperatures, see Tables 9.10, and 9.11. This would imply that in the extreme case ($-10\,^{\circ}\mathrm{C}$) we could expect up to a 20% error in the fluxes due to the liquid thermal conductivity. However, the Ward and Stanga experiments [4] do not go below $-1\,^{\circ}\mathrm{C}$, and thus we can expect errors due to the liquid thermal conductivity to be near or below 10%, which will not alter the conclusions drawn from the model results.

11.2 Surface Tension Effects

Surface tension will create an equilibrium pressure difference across a free surface such as liquid vapor interface. For a curved liquid surface surrounded by vapor, as shown in Figure 11.1, the equilibrium pressure difference due to surface tension is [62]

$$p_l - p_v = \frac{2\eta}{r_c}. \tag{11.1}$$

Here p_l is the pressure in the liquid, η is the surface tension coefficient, and r_c is the radius of surface curvature.

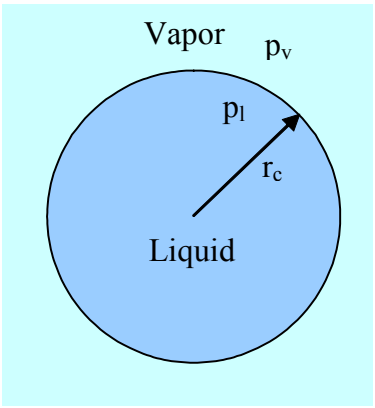

Figure 11.1: Curved surface, surface tension diagram

By Eqn. (11.1) a planar surface with infinite radius of curvature has no contribution of surface tension to pressure difference across the interface. The spherical model however, will have surface tension contributions.

11.2.1 Surface Tension Adjusted Saturation Pressure

The addition of surface tension affects the equilibrium condition. We re-derive the saturation pressure accounting for surface tension.

From Eqn. (11.1) the equilibrium liquid pressure is given by

$$p_l = p_v + \frac{2\eta}{r_c}. \tag{11.2}$$

In equilibrium the liquid and vapor temperatures are equal, $T_l = T_v = T$, and the vapor pressure is equal to the saturation pressure at temperature T, $p_v = p'_{sat}(T)$. From Eqn. (11.2) the liquid equilibrium pressure follows as

$$p_l = p'_{sat}(T) + \frac{2\eta}{r_c}. \tag{11.3}$$

The liquid and vapor Gibbs free energies must be equal for equilibrium across the liquid vapor interface,

$$g_l(T, p_l) = g_v(T, p_v). \tag{11.4}$$

We need an expression for the liquid Gibbs free energy at the interface in terms of $p'_{sat}(T)$. Performing a Taylor series expansion about η we find

$$g_l(T, p_l) = g_l\left(T, p_v + \frac{2\eta}{r_c}\right) = g_l(T, p_v) + \frac{\partial g_l}{\partial p}(T, p_v)\frac{2\eta}{r_c} + \frac{1}{2}\frac{\partial^2 g_l}{\partial p^2}(T, p_v)\left(\frac{2\eta}{r_c}\right)^2. \tag{11.5}$$

By definition

$$\left(\frac{\partial g_l}{\partial p}\right)_T = \upsilon, \tag{11.6}$$

which leads to

$$\left(\frac{\partial^2 g_l}{\partial p^2}\right)_T = \left(\frac{\partial \upsilon}{\partial p}\right)_T = 0 \tag{11.7}$$

because we assume that the liquid is incompressible. Here υ is the specific volume. Eqn. (11.5) then becomes

$$g_l(T, p_l) = g_l(T, p_v) + \frac{2\eta}{r_c}\upsilon. \tag{11.8}$$

Substituting this into Eqn. (11.4), the equilibrium condition becomes

$$g_l\left[T, p'_{sat}(T)\right] + \frac{2\eta}{r_c}\upsilon = g_v\left(T, p'_{sat}(T)\right). \tag{11.9}$$

We now insert the constant specific heat enthalpies and entropies, Eqns. (2.35), (2.37), (2.39), and (2.42) to obtain

$$\begin{aligned} & c_l(T-T_o) - T\left(s_l^o + c_l \ln\left(\frac{T}{T_o}\right)\right) + \frac{2\eta}{r_c}\upsilon \\ = \;& c_p(T-T_o) + \Delta h_o - T\left(s_v^o + c_p \ln\left(\frac{T}{T_o}\right) - R\ln\left(\frac{p'_{sat}(T)}{p_o}\right)\right). \end{aligned} \tag{11.10}$$

We follow the same procedure used for the derivation of saturation pressure $p_{sat}(T)$ without surface tension Eqn. (2.49) and find

$$p'_{sat}(T) = p_o \exp\left(\frac{c_l - c_p}{R}\left(1 - \frac{T_o}{T} - \ln\left(\frac{T}{T_o}\right)\right) + \frac{\Delta h_o}{R}\left(\frac{1}{T_o} - \frac{1}{T}\right) + \frac{2\eta}{r_c}\frac{\upsilon}{RT}\right), \tag{11.11}$$

or in terms of $p_{sat}(T)$, the saturation pressure for the flat interface,

$$p'_{sat}(T) = p_{sat}(T) \exp\left(\frac{2\eta}{r_c}\frac{\upsilon}{RT}\right). \tag{11.12}$$

This is the same expression as found by Young [33].

11.2.2 Analysis of $p'_{sat}(T)$

The surface tension coefficient for water is $\eta = 72.7 \times 10^{-3} \frac{\mathrm{J}}{\mathrm{m}^2}$ [62].

To estimate the size of the correction due to surface tension, the liquid water specific volume is taken as $\upsilon = 10^{-3} \frac{\mathrm{m}^3}{\mathrm{kg}}$, the temperature as $T = 273\,\mathrm{K}$, and the radius of curvature as $r_c = 1\,\mathrm{mm}$ (same order of magnitude as the Ward and Stanga experiments [4]). The saturation pressure correction factor of Eqn. (11.12) is $\frac{2\eta}{r_c}\frac{\upsilon}{RT} = 1.15 \times 10^{-6}$, the exponential of this is unity to 6 decimal places. In other words we do not expect the surface tension to affect the saturation pressure for a radius of curvature of the order of 1 mm. Using the same temperature and specific volume we find that $r_c \leq 1.16 \times 10^{-4}\,\mathrm{mm}$ must be true before $p'_{sat}(T)$ will be more than 1% greater than $p_{sat}(T)$.

To incorporate the surface tension correction into the models, the liquid Gibbs free energy must

be made to include the surface tension correction,

$$g_l' = g_l + \frac{2\eta}{r_c}\upsilon. \tag{11.13}$$

The spherical liquid temperature profile constant, Eqn. (10.18), becomes

$$T_{cl} = \frac{Q_i}{j_i c_l} + T_o - \frac{2\eta}{c_l r_c}\upsilon. \tag{11.14}$$

The SRT mass flux, Eqn. (3.13) reads

$$j = k\left(\begin{array}{c} \exp\left(\frac{g_l+\frac{2\eta}{r_c}\upsilon}{RT_l} - \frac{g_v}{RT_v} + \frac{h_v}{R}\left(\frac{1}{T_v}-\frac{1}{T_l}\right)\right) \\ -\exp\left(\frac{-\left(g_l+\frac{2\eta}{r_c}\upsilon\right)}{RT_l} + \frac{g_v}{RT_v} - \frac{h_v}{R}\left(\frac{1}{T_v}-\frac{1}{T_l}\right)\right) \end{array}\right). \tag{11.15}$$

We use Eqn. (11.12) in the place of the saturation pressure. The SRT (3.13) (3.8), CE (4.16) (4.20), and CEVEL (4.71) (4.74) (4.75) models were run with the experimental data, Table 6.1, with coefficients from Tables 6.3, and 6.4. We found negligible change in the results with the addition of surface tension. We conclude that the surface tension does not play a significant role for our situation.

11.3 Constant Liquid Temperature Zone

Ward and Stanga [4] observe a small isothermal zone in the liquid, adjacent to the interface during their evaporation and condensation experiments, which they suggest could be due to surface tension driven Marangoni-Benard convection, or energy partitioning during the phase change process. However they are unable to conclude that either process is responsible. In any case, our simple models do not allow for either of these phenomena, and thus do not predict a liquid isothermal zone. None the less, we wish to investigate the effect the isothermal zone might have on the results, and introduce a forced liquid constant temperature zone adjacent to the interface into our models, and observe its effect on the interface conditions and fluxes.

11.3.1 Planar Interface

The liquid is separated into two zones, the constant temperature zone of thickness L_c, and the non-isothermal zone of thickness $L_l - L_c$. By definition the temperature gradient, and thus the conductive flux, in the isothermal zone must be zero, $q_l = 0$. From Eqn. (2.24) we see this implies only convective energy flux due to the mass flux in the isothermal zone,

$$Q = jh_l\left(T_l\right) \tag{11.16}$$

at the liquid interface temperature T_l. We recall from our discussion of the balance laws that the mass and energy fluxes, j and Q are constants. Outside of the isothermal zone the conductive flux must be included in the energy flux (2.24), leading to

$$Q = jh_l\left(T_l\right) + q_l. \tag{11.17}$$

For Eqns. (11.16), and (11.17) to agree, assuming the bulk liquid properties still apply in the isothermal zone and the liquid enthalpy is only a function of temperature, there must be a temperature jump across the boundary between the two liquid zones, which Ward and Stanga [4] do not observe, or the temperature gradient there must be zero, which can not be true based on our previous analysis without the isothermal zone, see Figure 10.3. In Figure 10.3 the liquid temperature gradient is almost linear, a fact that Ward and Stanga also point out [4], suggesting that it can not be zero near the interface. We conclude that Eqns. (11.16), and (11.17) do not agree, and thus the assumption of only convective heat flux due to the mass flux in the isothermal zone can not be valid.

We instead use the energy flux at the boundary between the two liquid temperature zones to describe the energy flux through the isothermal zone to the interface, see Figure 11.2.

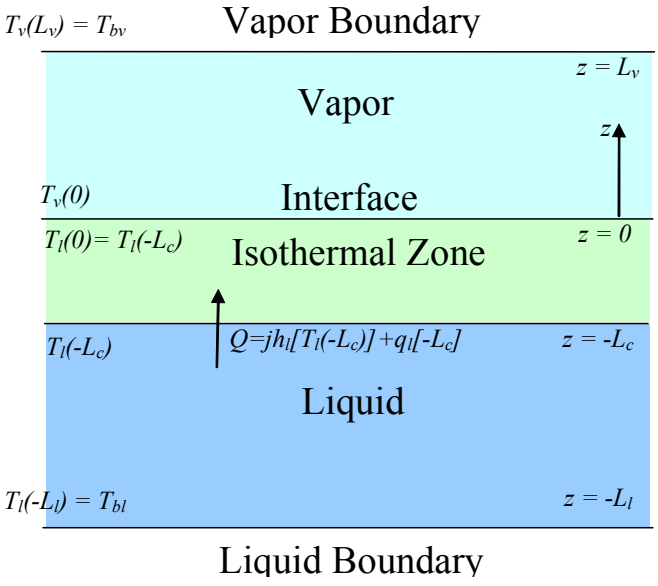

Figure 11.2: Isothermal zone, planar geometry

At the boundary between the two liquid zones the energy flux is

$$Q = jh_l\left[T_l\left(-L_c\right)\right] + q_l\left[-L_c\right], \tag{11.18}$$

where the conductive energy flux is $q_l\left(-L_c\right) = -\kappa_l \frac{dT_l}{dz}\left(-L_c\right)$. In the isothermal zone, from our constant specific heat assumption (2.35) we know that $h_l\left(-L_c\right) = h_l\left(0\right)$. Continuous temperature across the liquid zone boundary is assumed. The conductive energy flux is assumed to be completely transferred through the isothermal zone via an alternate form of energy transport, such as Marangoni-Benard convection. This is necessary to satisfy the balances of mass and energy, which force constant mass and energy fluxes. The liquid interface temperature in the liquid interface temperature profile (2.59) will now be evaluated at $z = -L_c$, instead of $z = 0$, which was done for the non-isothermal case.

We compare the model results with and without the isothermal zone. Again, we apply the conditions from Ward and Stanga 's experiment E1 [4], Table 6.1, where the measured isothermal zone thickness is $L_c = 0.34 \times 10^{-3}$ m using the SRT (3.13) (3.8), CE (4.16) (4.20), and CEVEL

(4.71) (4.74) (4.75) models, with coefficients from Tables 6.3, and 6.4. Table 11.1 presents the results.

Model	Iso. Temp. Zone	T_l (°C)	T_v (°C)	$j\ \left(\frac{\text{kg}}{\text{m}^2\,\text{s}}\right)$	$Q\ \left(\frac{\text{W}}{\text{m}^2}\right)$
SRT	No	-0.329	2.67	1.18×10^{-3}	2861
	Yes	-0.328	2.45	1.27×10^{-3}	3071
CE	No	-0.330	-0.385	1.19×10^{-3}	2861
	Yes	-0.329	-0.389	1.27×10^{-3}	3071
CE VEL	No	2.01	2.67	1.08×10^{-3}	2612
	Yes	2.16	2.73	1.15×10^{-3}	2787

Table 11.1: Planar non-isothermal and isothermal liquid zone results comparison

Table 11.1 indicates the mass and energy fluxes increase with the addition of the liquid isothermal zone, but the interface temperatures are nearly constant. The increase in mass and energy flux is likely due to the interface temperature being evaluated for a slightly larger liquid temperature gradient, at distance L_c from the interface, than would be the case if it was evaluated at the interface.

11.3.2 Spherical Interface

We apply the same procedure and implement a constant liquid temperature zone with the spherical temperature profile, see Table 11.2.

Model	Iso. Temp. Zone	T_l (°C)	T_v (°C)	$j\ \left(\frac{\text{kg}}{\text{m}^2\,\text{s}}\right)$	$Q\ \left(\frac{\text{W}}{\text{m}^2}\right)$
SRT	No	-0.287	15.3	2.27×10^{-4}	524
	Yes	-0.287	15.3	2.31×10^{-4}	531
CE	No	-0.342	-0.293	2.48×10^{-4}	524
	Yes	-0.342	-0.293	2.51×10^{-4}	531
CE VEL	No	0.192	8.21	2.33×10^{-4}	514
	Yes	0.199	8.21	2.36×10^{-4}	521

Table 11.2: Spherical non-isothermal and isothermal liquid zone results comparison

As in the planar case the fluxes all increase slightly with the addition of the liquid constant temperature zone, but the interface temperatures are nearly unchanged.

Chapter 12

Model Comparison with Experimental Data

In the previous chapters we have discussed the irreversible thermodynamics, SRT, and kinetic theory flux expressions. We have examined factors that influence the interface temperatures, interface temperature jump, temperature profiles, evaporation or condensation mass flux, and the energy flux. We now compare our model predictions to the Ward and Stanga measurements from their evaporation experiments E1, E2, E3, and E4, and condensation experiments C1, C2, C3, and C4 [59].

12.1 Evaporation Experiments

Figure 12.1 shows the measured temperature distribution of evaporation experiment E1 [59]. As we mentioned in the Chapter 10, the curvature of the vapor temperature profile appears similar to that of the spherical evaporation case, see Figure 10.2, but is opposite to that of the planar temperature profile, Figure 10.3.

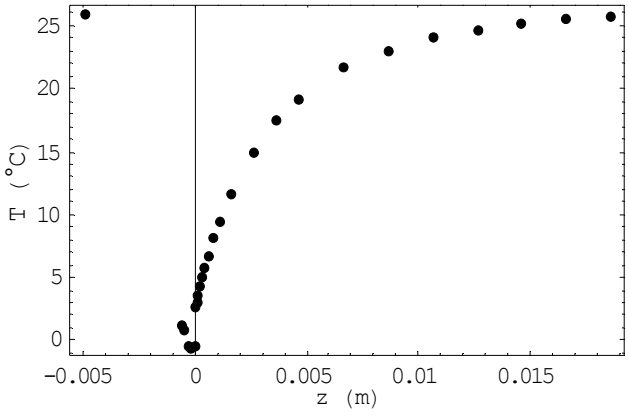

Figure 12.1: Measured evaporation temperature profile, experiment E1

The mass flux in the planar geometry was close to the measured value, while the mass flux was an order of magnitude too small in the spherical geometry, see Tables 10.3, and 10.2. Since we also observed that the liquid conditions affect the fluxes more significantly than the vapor, we suggest to use a planar temperature distribution in the liquid to more closely predict the measured mass flux. This would also yield a near linear liquid temperature gradient, as Ward and Stanga suggest is the case [4].

If the funnel of the experimental apparatus (Figure 12.2 [4]) which holds the liquid water is well insulated, we could expect the absolute energy flux through any cross section to be constant, which is a property of our radial mass (10.2) and energy fluxes (10.6). However the outside wall of the funnel in the Ward, Fang, and Stanga apparatus is exposed to the vapor in the evaporation chamber. This suggests that there will be heat transfer through the walls of the funnel between the liquid inside the funnel, and the vapor outside, in the case of evaporation adding heat to the liquid, thus enhancing the evaporative fluxes. We suggest this heat transfer could be a reason why Ward and Stanga do not observe a spherical temperature profile in the liquid, and their measured fluxes are higher than those calculated using our spherical model.

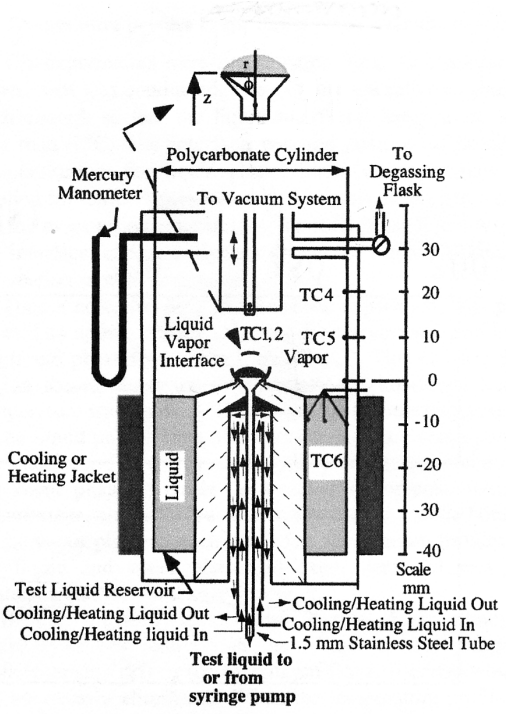

Figure 12.2: Ward et al. evaporation condensation apparatus

The addition of the constant temperature zone, although it slightly increases the fluxes, will not greatly alter the results. It is included in the simulations mainly to allow for better comparison of the modelled temperature profiles with measurements.

We mentioned earlier that Ward and Stanga suggest that the liquid temperature gradient is constant [4]. Figure 12.1 demonstrates that the liquid temperature measurements are concentrated near the interface, with only one measurement at the liquid boundary. We suggest that further measurement points in the liquid region are necessary to confirm the constant liquid temperature gradient. We will show that the measured liquid temperature points can be fit using both spherical and planar liquid temperature profiles.

With the afore mentioned considerations, we present the evaporation results using the constant liquid temperature zone, and the spherical vapor temperature distribution, with planar and spherical liquid temperature distributions. The SRT (3.13) (3.8), CE (4.16) (4.20), and CEVEL (4.71) (4.74) (4.75) models are employed. We re-adjust the phenomenological conductive energy

flux coefficient α, the velocity dependant condensation coefficient parameters ψ and ω, and the accommodation coefficient γ to fit the vapor interface temperature of experiment E1 for each of the temperature profile combinations. We then use this set of coefficients for modelling the remainder of the experiments.

Table 12.1 gives the model input data, and boundary conditions for the Ward and Stanga evaporation experiments [4], [59].

Experiment	p_v (Pa)	T_{bl} (°C)	L_l (mm)	T_{bv} (°C)	L_v (mm)	R_o (mm)	L_c (mm)
E1	593	26.06	4.97	25.7	18.59	6.088	0.34
E2	639	19.23	4.95	25.88	18.67	6.20	0.38
E3	616	12.52	4.90	25.08	18.70	6.506	0.35
E4	629	7.06	4.96	25.76	18.66	6.143	0.61

Table 12.1: Ward et al. evaporation experimental data

From Table 12.1 the vapor pressures used for the evaporation experiments are all very close, near 600 Pa, which corresponds to a saturation temperature $T_{sat}\,(p_v)$ of approximately 0 °C [56]. From our earlier observations we expect that the liquid interface temperature will be very close to the vapor pressure saturation temperature, thus we expect $T_l \approx 0\,^{\circ}\mathrm{C}$ for all the evaporation experiments.

We have already seen that the evaporative and condensation forcing is strongly related to the relation between $T_{sat}\,(p_v)$, and the liquid boundary temperature T_{bl}. For $T_{bl} > T_{sat}\,(p_v)$ there is forcing in the evaporation direction, and for $T_{bl} < T_{sat}\,(p_v)$ there is forcing in the condensation direction. We have already mentioned that p_v does not change greatly between the evaporation experiments. We see from Table 12.1 that $T_{bl} > T_{sat}\,(p_v)$ for all the evaporation experiments, and that it is decreased through the experiments. Thus we expect that experiment E1 will have the highest evaporation rate, while experiment E4 will have the lowest.

The coefficient values which yield results close to the experiment E1 data for the various geometry choices are given in Table 12.2.

Geometry	$\alpha\ \left(\frac{\mathrm{W\,K}}{\mathrm{m}^2}\right)$	ψ	ω	γ
Planar liquid and spherical vapor	1.37×10^6	5.78×10^{-2}	1	1
Spherical liquid and spherical vapor	1.68×10^6	6.38×10^{-2}	1	1

Table 12.2: Coefficient values, experiment E1

We see from Table 12.2, and the planar interface data Tables 6.3 and 6.4, that the coefficient values do change slightly for the different geometries, this is due to the influence of energy flux on the vapor interface temperature. We recall that α gives the ratio between the conductive heat flux in the vapor at the interface to the interface temperature jump, Eqn. (3.8), ψ is a measure of how many incident molecules hitting the interface condense, and ω sets the dependence of the condensation coefficient on the molecular energy and surface temperature, Eqn. (4.51).

It is necessary to choose a common coordinate system, if we are to combine the planar liquid temperature profile with the spherical vapor profile. We wish to write everything in terms of coordinate z since $z = 0$ at the interface is easily identifiable. Comparing the planar and spherical model geometries, Figures 1.3 and 10.1, we have at the interface,

$$z = 0, \text{ and } r = r_i = R_o, \tag{12.1}$$

telling us that

$$z = r - r_i. \tag{12.2}$$

where R_o is the interface radius of curvature. We also know from Table 10.1 that the boundary conditions are related by

$$r_v = r_i + L_v, \text{ and } r_l = r_i - L_l. \tag{12.3}$$

12.1.1 Experiment E1

The experiment E1 parameters are given by Table 12.1, while the coefficients which we use are in Table 12.2.

Table 12.3 shows the measured interface conditions (top line), the predictions from the three models for the different temperature profile geometries, and the difference between the models and experiments (°C for temperatures, and % for the mass flux).

Model	T_l (°C)	T_v (°C)	$j\ \left(\frac{\text{kg}}{\text{m}^2\,\text{s}}\right)$	Coefficient(s)
Measured	-0.4	2.6	1.017×10^{-3}	-
SRT Planar Liquid,	-0.328	2.67	1.29×10^{-3}	$\alpha = 1.37 \times 10^6$
Spherical Vapor	$0.072°C$	$0.07°C$	27.0%	$\left(\frac{\text{W K}}{\text{m}^2}\right)$
SRT Spherical Liquid,	-0.338	2.67	2.47×10^{-4}	$\alpha = 1.68 \times 10^6$
Spherical Vapor	$0.062°C$	$0.07°C$	75.7%	$\left(\frac{\text{W K}}{\text{m}^2}\right)$
CE Planar Liquid,	-0.329	-0.346	1.30×10^{-3}	-
Spherical Vapor	$0.071°C$	$2.95°C$	27.4%	-
CE Spherical Liquid,	-0.293	-0.342	2.51×10^{-4}	-
Spherical Vapor	$0.107°C$	$2.94°C$	75.3%	-
CEVEL Planar Liquid	0.505	2.67	1.25×10^{-3}	$\psi = 5.78 \times 10^{-2}$
Spherical Vapor	$0.105°C$	$0.07°C$	23.1%	$\omega = 1,\ \gamma = 1$
CEVEL Spherical Liquid,	-0.188	2.67	2.46×10^{-4}	$\psi = 6.38 \times 10^{-2}$
Spherical Vapor	$0.212°C$	$0.07°C$	75.8%	$\omega = 1,\ \gamma = 1$

Table 12.3: Experiment E1 interface temperatures and mass fluxes

We see from Table 12.3 that the mass fluxes using the planar liquid temperature profile and spherical vapor profile are significantly closer to the measured mass flux, than the purely spherical cases.

The SRT and CEVEL models correctly predict the direction of the interface temperature jump, $T_v > T_l$, while the CE model predicts the opposite jump direction. As expected, the vapor interface temperature predictions of the SRT and CEVEL models are very close to the measured vapor interface temperature, due to the choices of their coefficients, while the CE vapor interface temperature is very far from the experimental value. The SRT and CE models predict the liquid interface temperature more closely than the CEVEL model, which predicts a higher liquid

interface temperature. It follows that the SRT temperature jump is very near the measured result, but the CEVEL is less because of its higher liquid interface temperature.

Figure 12.3 represents the three models with a planar liquid temperature distribution, and spherical vapor temperature distribution. The vapor and liquid temperature distributions of the three models are similar. The curvature of the model vapor temperature profiles agrees with that of the measured profile. The liquid temperature profile is linear which fits well with the limited liquid data points. It also agrees with Ward and Stanga 's statement that the liquid temperature gradient is constant [4].

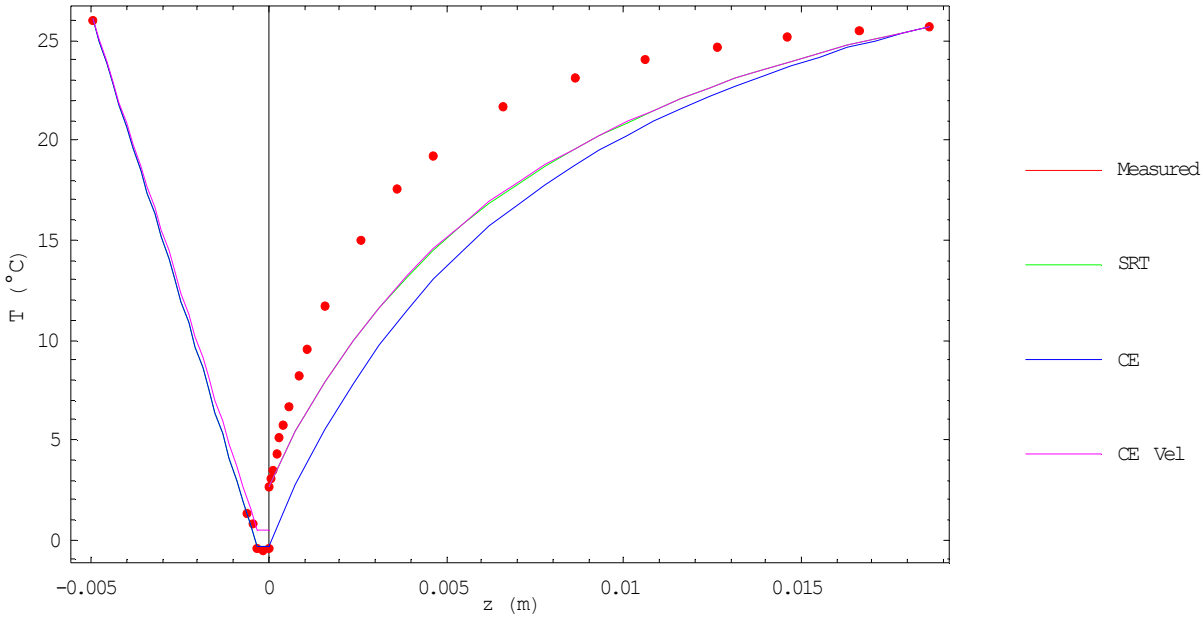

Figure 12.3: Planar liquid and spherical vapor temperature profiles, experiment E1

Figure 12.4 uses the spherical liquid and vapor temperature profiles. The vapor temperature profiles are similar to Figure 12.3. The liquid temperature profiles no longer have a constant gradient. Although this liquid temperature profile does not fit the data as well as the planar liquid temperature profile, it could still be representative depending on the location of additional measured data points in the liquid.

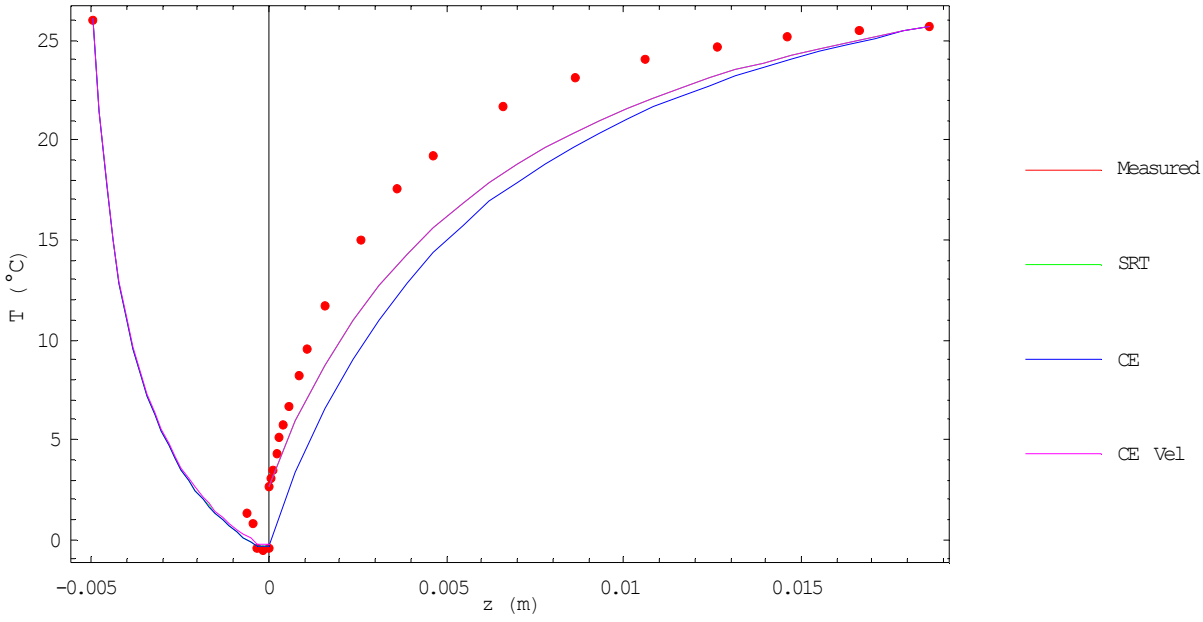

Figure 12.4: Spherical liquid and vapor temperature profiles, experiment E1

12.1.2 Experiments E2-E4

In the subsequent evaporation experiments the mass flux is reduced by reducing the liquid boundary temperature T_{bl}, and thus the evaporative forcing; refer to Table 12.1, where the experimental input parameters are given. We reuse the coefficients from experiment E1, Table 12.2 to study how the various models describe the experiments.

Tables 12.4, 12.5, and 12.6 compare the model results, with the experimental measurements, while Figures 12.5, 12.6, 12.7, 12.8, 12.9, and 12.10 give the planar liquid, and spherical vapor, and spherical liquid and vapor temperature profiles.

Model	T_l (°C)	T_v (°C)	$j\ \left(\frac{\text{kg}}{\text{m}^2\,\text{s}}\right)$	Coefficient(s)
Measured	-0.1	2.8	7.97×10^{-4}	-
SRT Planar Liquid,	0.690	3.76	9.21×10^{-4}	$\alpha = 1.37 \times 10^6$
Spherical Vapor	$0.790°C$	$0.96°C$	15.5%	$\left(\frac{\text{W K}}{\text{m}^2}\right)$
SRT Spherical Liquid,	0.683	3.59	1.96×10^{-4}	$\alpha = 1.68 \times 10^6$
Spherical Vapor	$0.683°C$	$0.79°C$	75.3%	$\left(\frac{\text{W K}}{\text{m}^2}\right)$
CE Planar Liquid,	0.688	0.692	9.25×10^{-4}	-
Spherical Vapor	$0.788°C$	$2.11°C$	16.1%	-
CE Spherical Liquid,	0.680	0.726	2.00×10^{-4}	-
Spherical Vapor	$0.780°C$	$2.07°C$	74.9%	-
CEVEL Planar Liquid,	1.25	3.47	8.94×10^{-4}	$\psi = 5.78 \times 10^{-2}$
Spherical Vapor	$1.35°C$	$0.67°C$	12.2%	$\omega = 1$, $\gamma = 1$
CEVEL Spherical Liquid,	0.795	3.39	1.95×10^{-4}	$\psi = 6.38 \times 10^{-2}$
Spherical Vapor	$0.895°C$	$0.59°C$	75.5%	$\omega = 1$, $\gamma = 1$

Table 12.4: Experiment E2 interface temperatures and mass fluxes (coefficients from experiment E1)

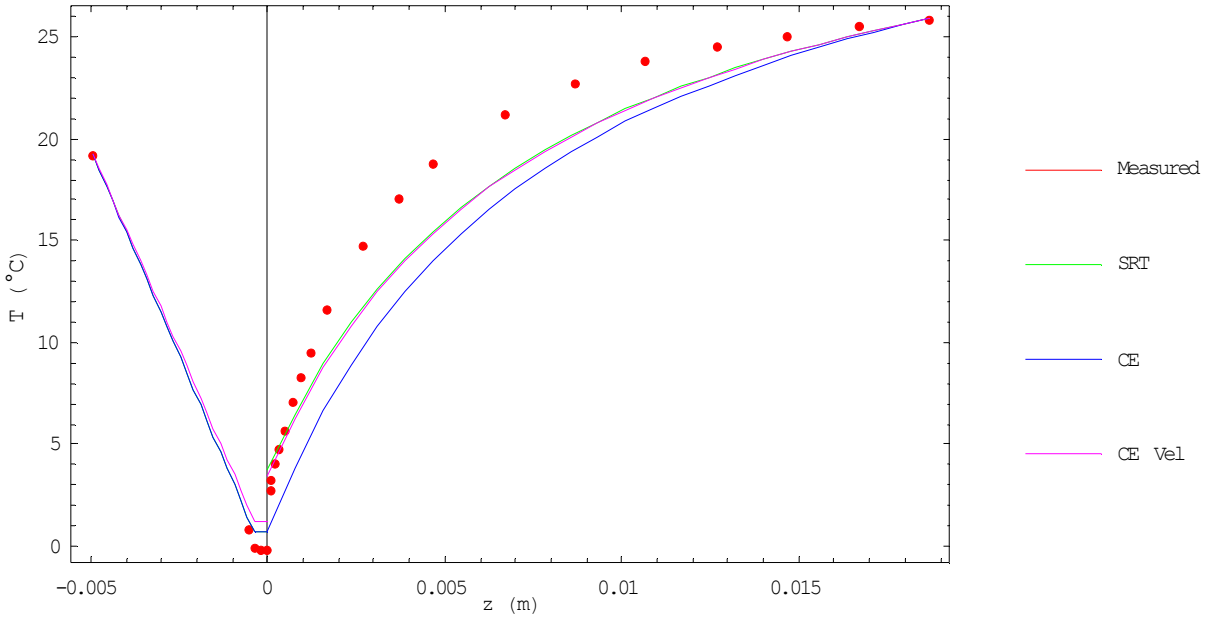

Figure 12.5: Planar liquid and spherical vapor temperature profiles, experiment E2

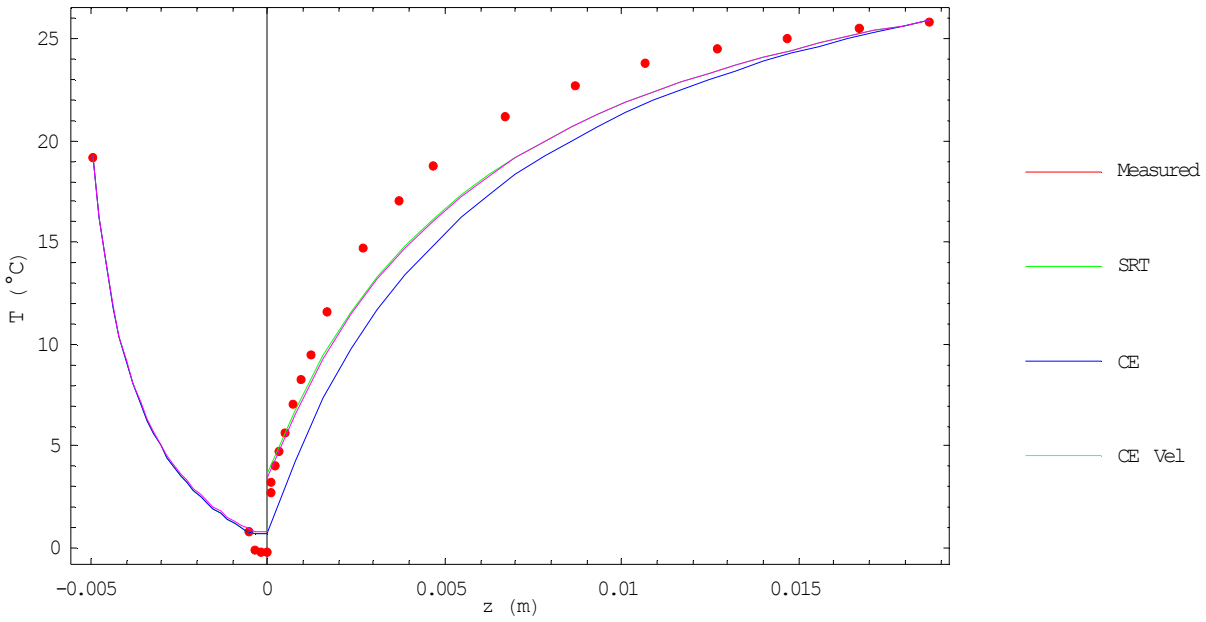

Figure 12.6: Spherical liquid and vapor temperature profiles, experiment E2

Model	T_l (°C)	T_v (°C)	$j\ \left(\frac{\text{kg}}{\text{m}^2\,\text{s}}\right)$	Coefficient(s)
Measured	-0.2	2.4	5.95×10^{-4}	-
SRT Planar Liquid,	0.185	3.26	6.19×10^{-4}	$\alpha = 1.37 \times 10^6$
Spherical Vapor	$0.385°C$	$0.86°C$	4.08%	$\left(\frac{\text{W K}}{\text{m}^2}\right)$
SRT Spherical Liquid,	0.180	2.97	1.64×10^{-4}	$\alpha = 1.68 \times 10^6$
Spherical Vapor	$0.380°C$	$0.57°C$	72.4%	$\left(\frac{\text{W K}}{\text{m}^2}\right)$
CE Planar Liquid,	0.182	0.201	6.23×10^{-4}	-
Spherical Vapor	$0.382°C$	$2.20°C$	4.78%	-
CE Spherical Liquid,	0.177	0.223	1.68×10^{-4}	-
Spherical Vapor	$0.377°C$	$2.20°C$	71.8%	-
CEVEL Planar Liquid,	0.576	3.00	6.01×10^{-4}	$\psi = 5.78 \times 10^{-2}$
Spherical Vapor	$0.776°C$	$0.60°C$	1.00%	$\omega = 1$, $\gamma = 1$
CEVEL Spherical Liquid,	0.276	2.87	1.63×10^{-4}	$\psi = 6.38 \times 10^{-2}$
Spherical Vapor	$0.476°C$	$0.47°C$	72.5%	$\omega = 1$, $\gamma = 1$

Table 12.5: Experiment E3 interface temperatures and mass fluxes (coefficients from experiment E1)

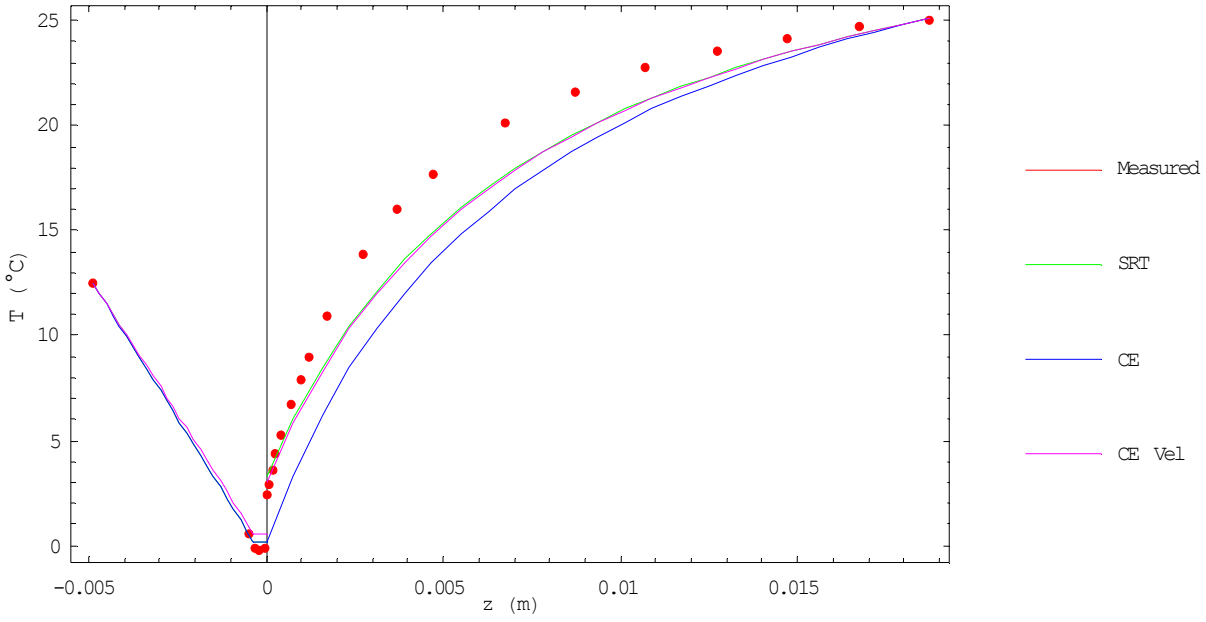

Figure 12.7: Planar liquid and spherical vapor temperature profiles, experiment E3

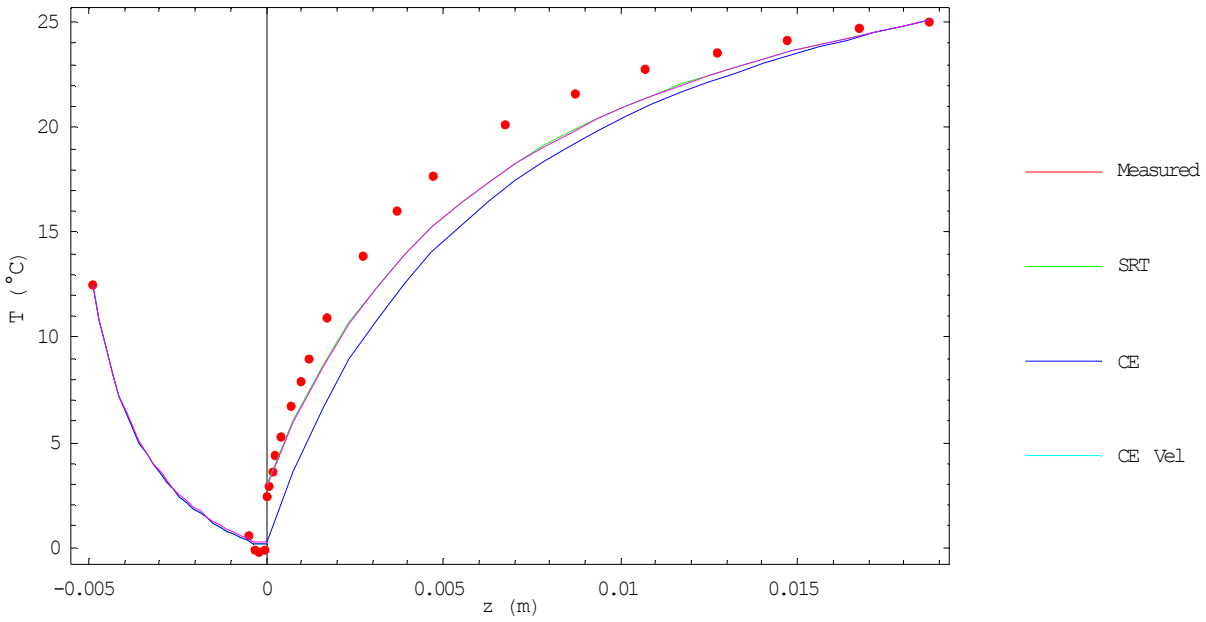

Figure 12.8: Spherical liquid and vapor temperature profiles, experiment E3

Model	T_l (°C)	T_v ($^\circ C$)	j $\left(\frac{\text{kg}}{\text{m}^2\,\text{s}}\right)$	Coefficient(s)
Measured	-0.1	2.5	4.19×10^{-4}	-
SRT Planar Liquid,	0.468	3.32	3.57×10^{-4}	$\alpha = 1.37 \times 10^6$
Spherical Vapor	$0.568^\circ C$	$0.82^\circ C$	14.7%	$\left(\frac{\text{W K}}{\text{m}^2}\right)$
SRT Spherical Liquid,	0.466	3.46	8.41×10^{-5}	$\alpha = 1.68 \times 10^6$
Spherical Vapor	$0.566^\circ C$	$0.96^\circ C$	79.9%	$\left(\frac{\text{W K}}{\text{m}^2}\right)$
CE Planar Liquid,	0.466	0.503	3.61×10^{-4}	-
Spherical Vapor	$0.566^\circ C$	$2.00^\circ C$	13.8%	-
CE Spherical Liquid,	0.462	0.516	8.78×10^{-5}	-
Spherical Vapor	$0.562^\circ C$	$1.98^\circ C$	79.0%	-
CEVEL Planar Liquid,	0.691	3.46	3.46×10^{-4}	$\psi = 5.78 \times 10^{-2}$
Spherical Vapor	$0.791^\circ C$	$0.96^\circ C$	17.4%	$\omega = 1$, $\gamma = 1$
CEVEL Spherical Liquid,	0.514	3.28	8.39×10^{-5}	$\psi = 6.38 \times 10^{-2}$
Spherical Vapor	$0.614^\circ C$	$0.78^\circ C$	80.0%	$\omega = 1$, $\gamma = 1$

Table 12.6: Experiment E4 interface temperatures and mass fluxes (coefficients from experiment E1)

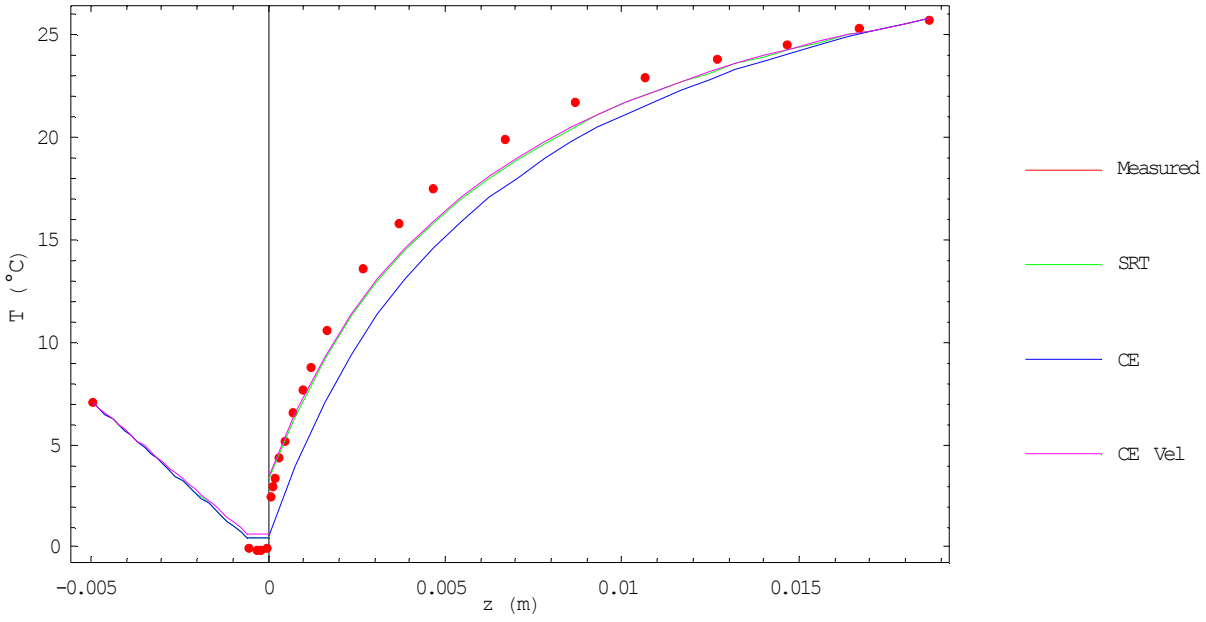

Figure 12.9: Planar liquid and spherical vapor temperature profiles, experiment E4

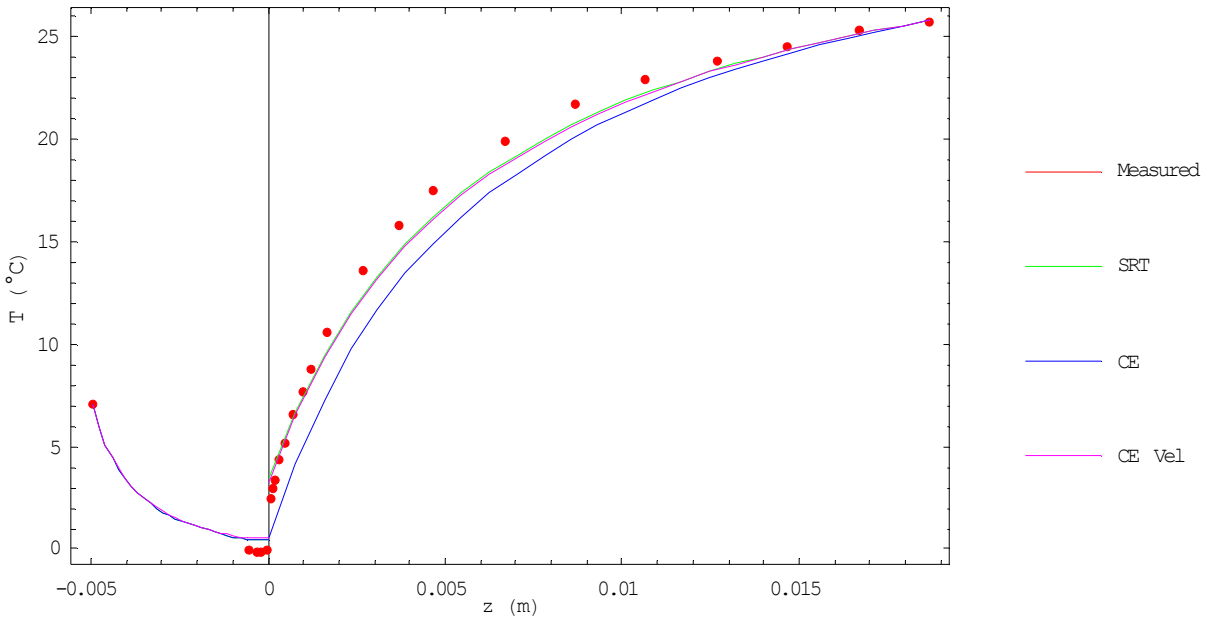

Figure 12.10: Spherical liquid and vapor temperature profiles, experiment E4

We see for each plot with a planar liquid temperature profile, Figures 12.3, 12.5, 12.7, and 12.9, that the liquid temperature gradient is near constant, where as for each plot using a spherical liquid temperature profile, Figures 12.4, 12.6, 12.8, and 12.10, the liquid temperature profile is exponential. If Ward and Stanga [4] are correct that the liquid temperature profile is indeed linear, then this would imply that there must by a planar temperature profile in the liquid. However we note, because of the lack of data points in the vapor, the spherical liquid temperature profiles can still fit with the data points, see Figures 12.4, 12.6, 12.8, and 12.10.

From Tables 12.3, 12.4, 12.5, and 12.6 we observe that the mass fluxes predicted by the models with the planar liquid temperature profile yield significantly closer results to the measured values, than the models with spherical liquid temperature profiles. This also suggests the possibility of a planar liquid temperature profile. However heat transfer through the funnel walls could be affecting the experimental results.

The measured liquid interface temperatures are as predicted, almost constant from experiment to experiment since the vapor pressure is not changed greatly. The liquid interface temperatures are close to the vapor pressure saturation temperature, except for the CEVEL model which slightly overpredicts the liquid interface temperature. The SRT, and CEVEL vapor interface temperature predictions are the most accurate for experiment E1, since their coefficients are optimized for that data set. However, for all experiments the vapor interface temperature of these models is closer to the measured value than the CE model. The SRT and CEVEL models also agree with the sign of the interface temperature jump for all evaporation experiments, $T_v > T_l$. The CE model greatly under predicts the temperature jump, however contrary to our earlier findings it does predict the correct jump direction $T_v > T_l$ for all the evaporation experiments except experiment E1.

Experiments E1 through E4 have shown the behavior of the models with variations in the liquid boundary temperature, it would now be useful to test the models for different vapor pressures. This what is done in the next section, where condensation is considered.

12.2 Condensation Experiments

We maintain the coefficient values established from experiment E1, see Table 12.2. The condensation experiments are modelled using the same geometrical temperature distribution choices as for the evaporation, a planar liquid with spherical vapor profile, and a spherical liquid and vapor profile.

We do not present the spherical liquid temperature distribution case for experiment C2. There the interface radius of curvature R_o is less than the liquid depth L_l. In our models we assume the interface radius of curvature is equal to the interface radius, r_i. By our definition of the liquid boundary radius, Table 10.1, $r_l = r_i - L_l$ implying the liquid boundary radius would be negative which is not physical.

The condensation experimental data is given in Table 12.7 [4], [59].

Experiment	p_v (Pa)	T_{bl} (°C)	L_l (mm)	T_{bv} (°C)	L_v (mm)	R_o (mm)	L_c (mm)
C1	3181	0.00	4.81	30.81	18.78	7.119	0.22
C2	2161	0.07	5.37	24.3	18.33	4.545	0.37
C3	1463	−0.02	4.87	19.65	18.73	6.690	0.19
C4	959	−0.10	5.06	17.75	18.60	5.628	0.25

Table 12.7: Ward et al. condensation experimental data

Unlike the evaporation experiments, the condensation experiments were varied by adjusting the vapor pressure p_v, and holding the liquid boundary temperature T_{bl} nearly constant. From our earlier discussion we expect the liquid interface temperature T_l to vary closely with the vapor pressure saturation temperature $T_{sat}\,(p_v)$, and thus expect T_l to decrease with the decreased p_v from experiments C1 to C4. We have seen that $T_{bl} < T_{sat}\,(p_v)$ causes a condensation forcing. Experiment C4 will have the lowest saturation temperature, and thus the lowest condensation flux.

Tables 12.8-12.11 compare the model results with the measured data. Figures 12.11-12.17 give the planar liquid with spherical vapor, and spherical liquid and vapor temperature profiles.

Model	T_l (°C)	T_v (°C)	j $\left(\frac{\text{kg}}{\text{m}^2\,\text{s}}\right)$	Coefficient(s)
Measured	25.6	26.0	-3.15×10^{-4}	-
SRT Planar Liquid,	25.1	26.1	-1.19×10^{-3}	$\alpha = 1.37 \times 10^6$
Spherical Vapor	$0.5°C$	$0.1°C$	279%	$\left(\frac{\text{W K}}{\text{m}^2}\right)$
SRT Spherical Liquid,	25.1	25.8	-3.72×10^{-4}	$\alpha = 1.68 \times 10^6$
Spherical Vapor	$0.5°C$	$0.2°C$	18.1%	$\left(\frac{\text{W K}}{\text{m}^2}\right)$
CE Planar Liquid,	25.1	25.1	-1.19×10^{-3}	-
Spherical Vapor	$0.5°C$	$0.9°C$	279%	-
CE Spherical Liquid,	25.1	25.1	-3.71×10^{-4}	-
Spherical Vapor	$0.5°C$	$0.9°C$	17.9%	-
CEVEL Planar Liquid,	24.9	25.1	-1.18×10^{-3}	$\psi = 5.78 \times 10^{-2}$
Spherical Vapor	$0.7°C$	$0.9°C$	276%	$\omega = 1$, $\gamma = 1$
CEVEL Spherical Liquid,	25.0	25.2	-3.71×10^{-4}	$\psi = 6.38 \times 10^{-2}$
Spherical Vapor	$0.6°C$	$0.8°C$	17.6%	$\omega = 1$, $\gamma = 1$

Table 12.8: Condensation experiment C1 interface temperatures and mass fuxes (coefficients from experiment E1)

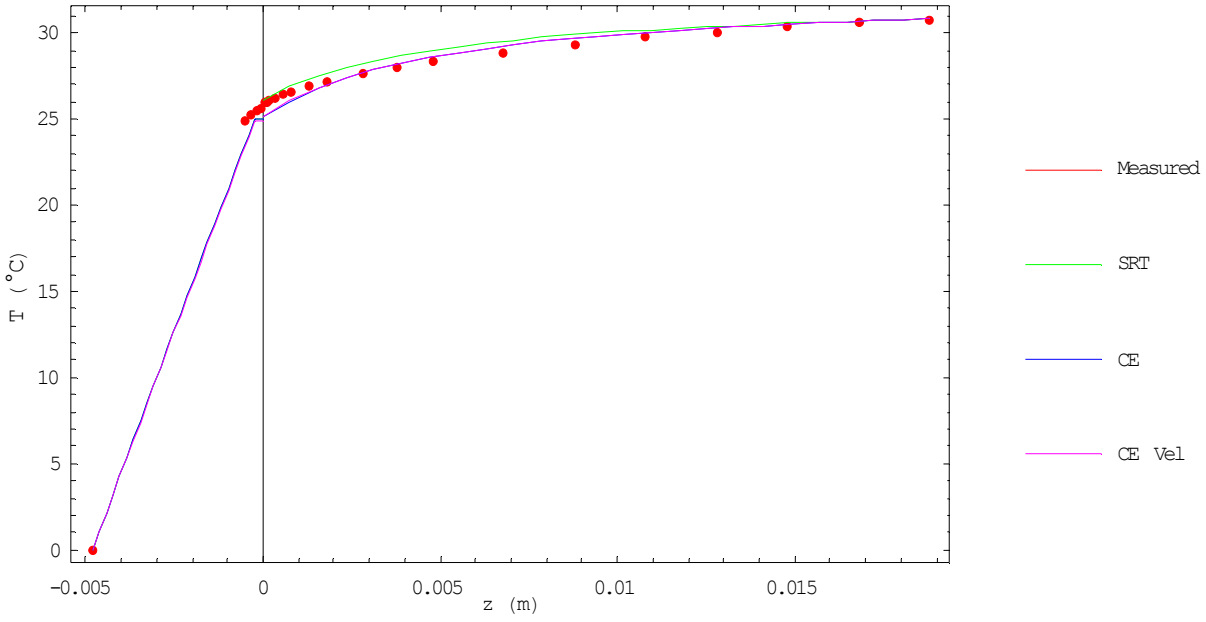

Figure 12.11: Planar liquid and spherical vapor temperature profiles, experiment C1

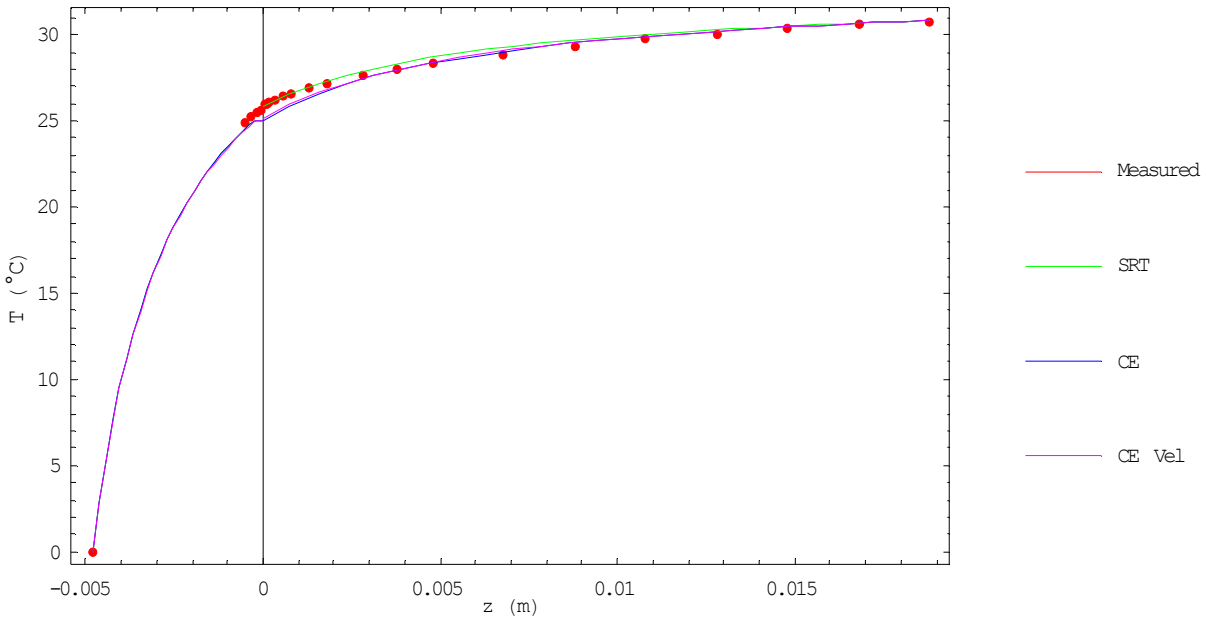

Figure 12.12: Spherical liquid and vapor temperature profiles, experiment C1

Model	T_l (°C)	T_v (°C)	$j\ \left(\frac{\text{kg}}{\text{m}^2\,\text{s}}\right)$	Coefficient(s)
Measured	19.1	19.4	-1.77×10^{-4}	-
SRT Planar Liquid,	18.7	19.9	-8.12×10^{-4}	$\alpha = 1.37 \times 10^6$
Spherical Vapor	$0.4°C$	$0.5°C$	359%	$\left(\frac{\text{W K}}{\text{m}^2}\right)$
CE Planar Liquid,	18.7	18.7	-8.10×10^{-4}	-
Spherical Vapor	$0.4°C$	$0.7°C$	358%	-
CEVEL Planar Liquid,	18.5	18.9	-8.02×10^{-4}	$\psi = 5.78 \times 10^{-2}$
Spherical Vapor	$0.6°C$	$0.5°C$	353%	$\omega = 1,\ \gamma = 1$

Table 12.9: Condensation experiment C2 interface temperatures and mass fuxes (coefficients from experiment E1)

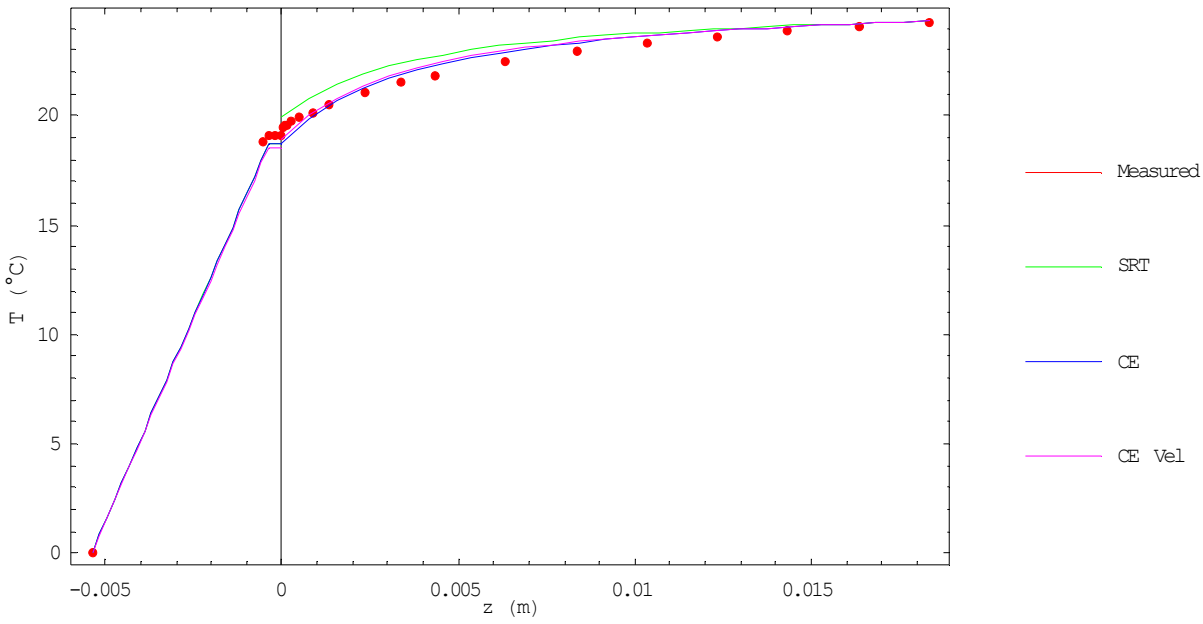

Figure 12.13: Planar liquid and spherical vapor temperature profiles, experiment C2

Model	T_l (°C)	T_v (°C)	j $\left(\frac{\text{kg}}{\text{m}^2\,\text{s}}\right)$	Coefficient(s)
Measured	12.6	13.0	-1.50×10^{-4}	-
SRT Planar Liquid,	12.6	13.8	-5.86×10^{-4}	$\alpha = 1.37 \times 10^6$
Spherical Vapor	$0.0°C$	$0.8°C$	290%	$\left(\frac{\text{W K}}{\text{m}^2}\right)$
SRT Spherical Liquid,	12.6	13.5	-1.48×10^{-4}	$\alpha = 1.68 \times 10^6$
Spherical Vapor	$0.0°C$	$0.5°C$	1.33%	$\left(\frac{\text{W K}}{\text{m}^2}\right)$
CE Planar Liquid,	12.6	12.7	-5.85×10^{-4}	-
Spherical Vapor	$0.0°C$	$0.3°C$	290%	-
CE Spherical Liquid,	12.6	12.7	-1.49×10^{-4}	-
Spherical Vapor	$0.0°C$	$0.3°C$	0.828%	-
CEVEL Planar Liquid,	12.5	13.0	-5.76×10^{-4}	$\psi = 5.78 \times 10^{-2}$
Spherical Vapor	$0.1°C$	$0.0°C$	284%	$\omega = 1$, $\gamma = 1$
CEVEL Spherical Liquid,	12.6	13.0	-1.48×10^{-4}	$\psi = 6.38 \times 10^{-2}$
Spherical Vapor	$0.1°C$	$0.0°C$	0.941%	$\omega = 1$, $\gamma = 1$

Table 12.10: Condensation experiment C3 interface temperatures and mass fluxes (coefficients from experiment E1)

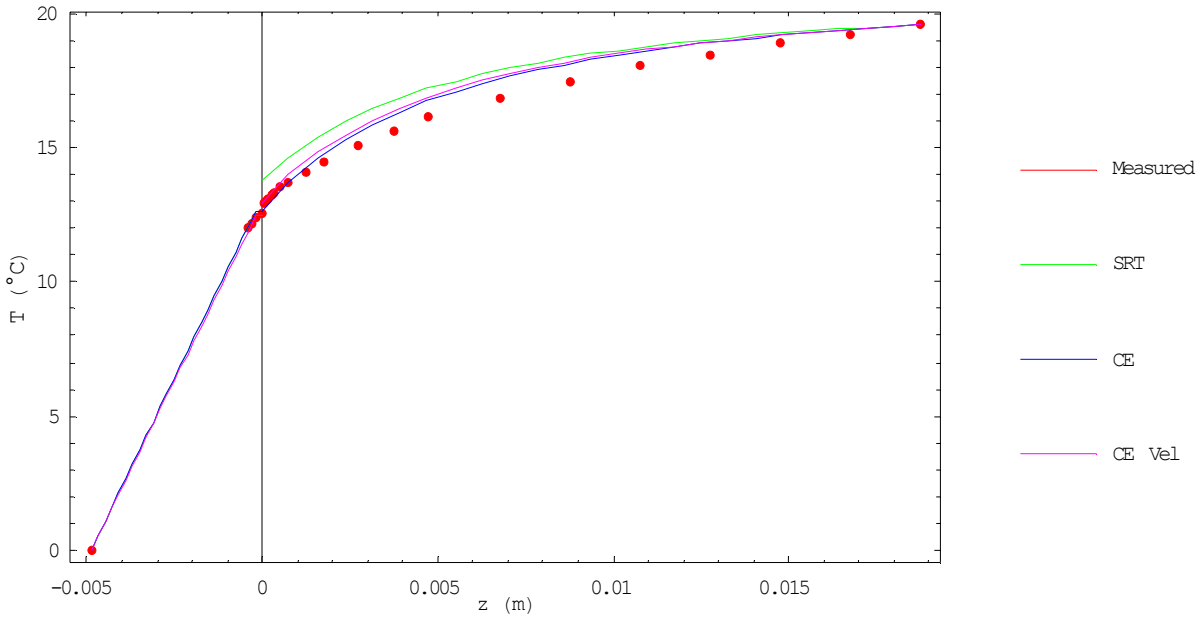

Figure 12.14: Planar liquid and spherical vapor temperature profiles, experiment C3

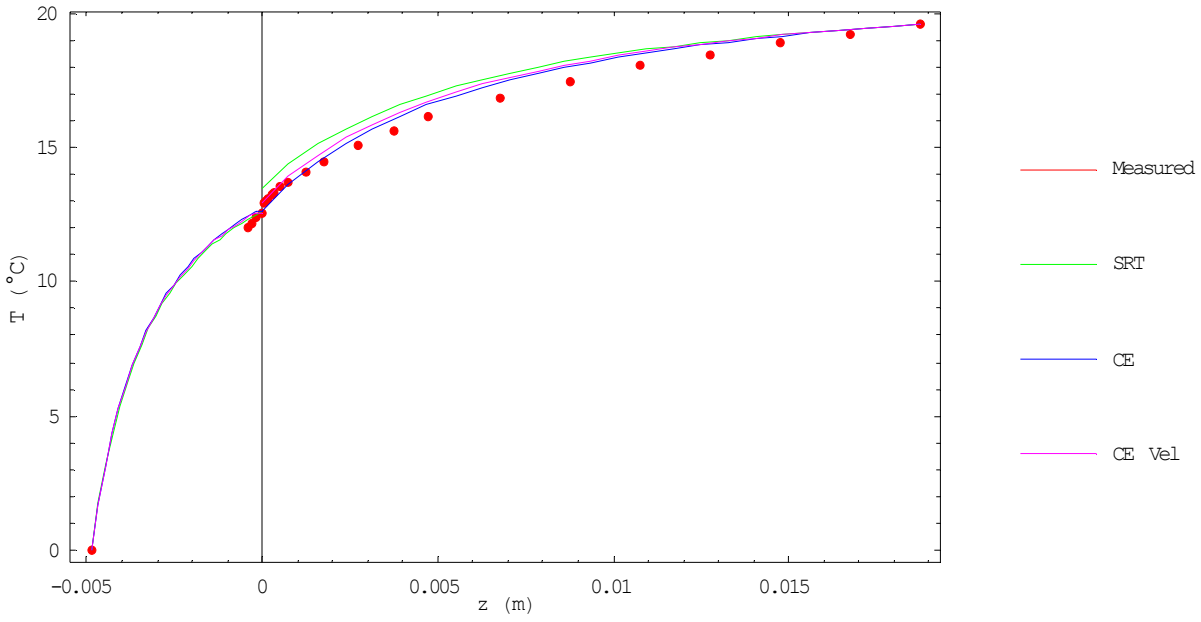

Figure 12.15: Spherical liquid and vapor temperature profiles, experiment C3

Model	T_l (°C)	T_v (°C)	j $\left(\frac{\text{kg}}{\text{m}^2\,\text{s}}\right)$	Coefficient(s)
Measured	6.9	7.5	-4.0×10^{-5}	-
SRT Planar Liquid,	6.40	8.25	-2.82×10^{-4}	$\alpha = 1.37 \times 10^6$
Spherical Vapor	$0.50°C$	$0.75°C$	606%	$\left(\frac{\text{W K}}{\text{m}^2}\right)$
SRT Spherical Liquid,	6.40	7.90	-1.57×10^{-5}	$\alpha = 1.68 \times 10^6$
Spherical Vapor	$0.50°C$	$0.40°C$	60.6%	$\left(\frac{\text{W K}}{\text{m}^2}\right)$
CE Planar Liquid,	6.39	6.42	-2.80×10^{-4}	-
Spherical Vapor	$0.51°C$	$1.08°C$	600%	-
CE Spherical Liquid,	6.40	6.42	-1.38×10^{-5}	-
Spherical Vapor	$0.50°C$	$1.08°C$	65.4%	-
CEVEL Planar Liquid,	6.27	7.41	-2.75×10^{-4}	$\psi = 5.78 \times 10^{-2}$
Spherical Vapor	$0.63°C$	$0.09°C$	589%	$\omega = 1$, $\gamma = 1$
CEVEL Spherical Liquid,	6.39	7.33	-1.50×10^{-5}	$\psi = 6.38 \times 10^{-2}$
Spherical Vapor	$0.51°C$	$0.17°C$	62.5%	$\omega = 1$, $\gamma = 1$

Table 12.11: Condensation experiment C4 interface temperatures and mass fluxes (coefficients from experiment E1)

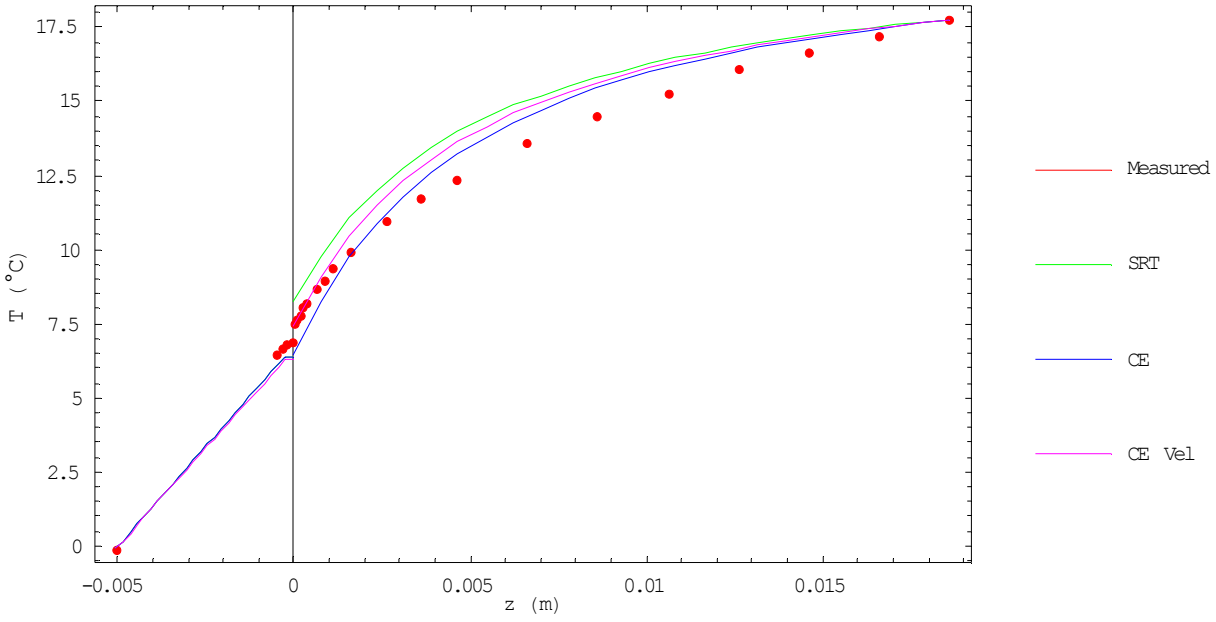

Figure 12.16: Planar liquid and spherical vapor temperature profiles, experiment C4

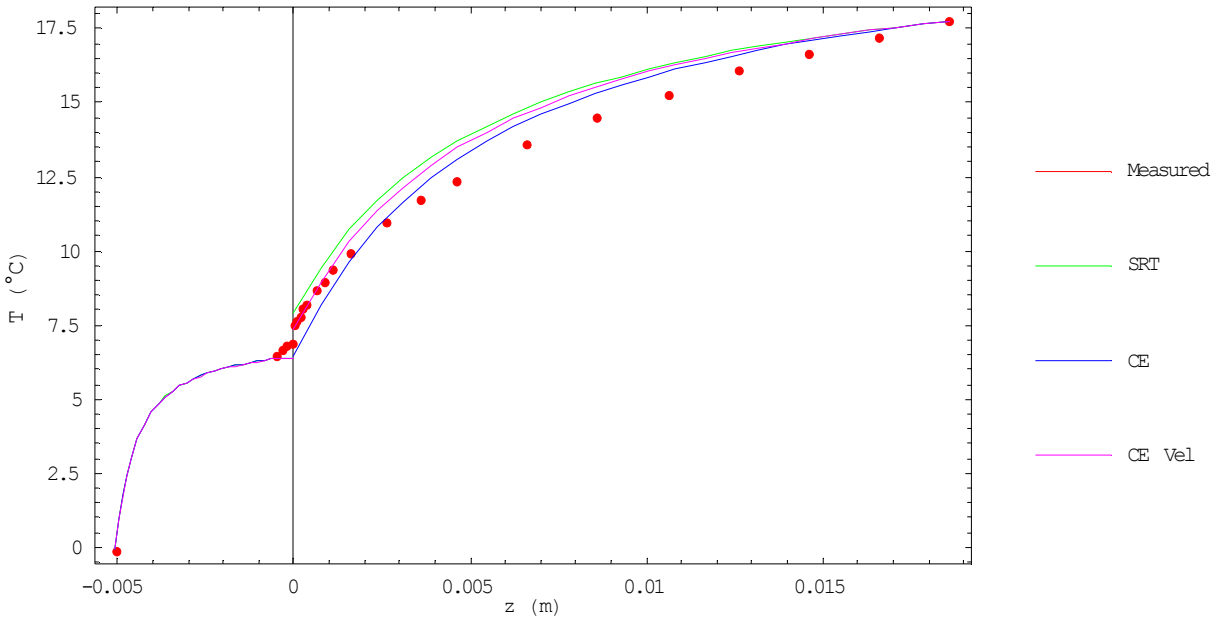

Figure 12.17: Spherical liquid and vapor temperature profiles, experiment C4

Again we see for each plot with a planar liquid temperature profile, Figures 12.11, 12.13, 12.14,

and 12.16, that the liquid temperature gradient is near constant, whereas for each plot using a spherical liquid temperature profile, Figures 12.12, 12.15, and 12.17, the liquid temperature profile is exponential. If Ward and Stanga [4] are correct that the liquid temperature profile is indeed linear, we see for condensation as well, that there must by a planar temperature profile in the liquid. However we note, because of the lack of data points in the vapor the spherical liquid temperature profiles can still fit with the data points, see Figures 12.12, 12.15, and 12.17.

From Tables 12.8-12.11 we observe that the mass fluxes predicted by the models with the spherical liquid temperature profile are significantly closer to the measured values, than the models with the planar liquid temperature profiles. This could indicate less heat leakage through the funnel walls than for evaporation.

For both, the evaporation and condensation cases, the models with the planar liquid temperature profile have greater mass fluxes (Approximately on order of magnitude higher) than the models with the spherical liquid temperature profile.

We see the liquid interface temperatures follow the vapor pressure saturation temperature, as we saw for evaporation. As we suggested, the condensation mass flux decreases as the vapor pressure is dropped. As for evaporation the SRT and CEVEL models reasonably predict the condensation vapor interface temperature, and temperature jump magnitude and direction $T_v > T_l$ relative to the measured data. The CE model as we saw with the evaporation experiments predicts a smaller temperature jump, but the correct direction $T_v > T_l$ for condensation experiments C3 and C4. In experiments C1 and C2 it predicts zero jump.

Chapter 13

Conclusions

The purpose of this work was to demonstrate the usability of irreversible thermodynamics and kinetic theory in describing the steady state evaporation and condensation of pure fluids, to analyze the statistical rate theory approach, and to investigate the physical phenomena involved in non-equilibrium phase change.

We developed simple one-dimensional planar and spherical models for slow evaporation and condensation based on the Ward, Fang, and Stanga [2], [3], [4] experiments. We considered pure liquid water evaporation and condensation to, and from its own vapor. We assumed the water vapor to be an ideal gas of uniform pressure, the liquid water as incompressible, constant liquid and vapor specific heat, and the thermal conductivities to be constant. Using the balances of mass, energy, and entropy, we developed expressions for the liquid and vapor temperature profiles, and the liquid surface saturation pressure. To achieve the complete solution, we required expressions for the mass and energy fluxes across the interface, which we found using irreversible thermodynamics, kinetic theory, and SRT. The equations were then solved to yield the mass and energy fluxes, and the liquid and vapor temperature profiles.

The results, and their variation with model parameters for irreversible thermodynamics, kinetic theory, and SRT were presented and compared between models, as well as with the Ward and Stanga measured data [4]. We now draw conclusions regarding the irreversible thermodynamics, kinetic theory, and SRT approaches, and some physical factors involved in steady state evaporation and condensation.

13.1 Irreversible Thermodynamics

The irreversible thermodynamics phenomenological mass and vapor conductive energy fluxes are given by Eqns. (3.7), and (3.8). This form neglects cross-over terms, and thus has only two phenomenological coefficients, for the mass flux β , and for the conductive heat flux α, which must both be positive to ensure positive entropy production.

The liquid interface temperature T_l is largely independent of either coefficient, the mass flux is slightly affected by the value of β, while α has a significant effect on the vapor interface temperature T_v, and thus the interface temperature jump $\Delta T = T_v - T_l$. The magnitude of ΔT increases as α decreases.

In all the IT model simulations we observed that T_l was nearly equal to the vapor pressure saturation temperature $T_{sat}\,(p_v)$, which agrees with the Ward and Stanga measurements [4].

The IT conductive energy flux equation (3.8) relates the direction and magnitude of the interface temperature jump to the conductive energy flux in the vapor. If the vapor conductive heat flux flows toward the interface (temperature gradient sloping down toward the surface,$\frac{dT_v}{dz} > 0$) we find $T_v > T_l$, while if it flows away from the interface (temperature gradient sloping down away from the surface $\frac{dT_v}{dz} < 0$) then $T_v < T_l$. This is true for evaporation and condensation, and agrees with the evaporation and condensation temperature jumps found by Ward, Fang, and Stanga [2], [3], [4]. Looking back to our discussion of parallel surface inverted temperature profiles, Figure 1.8, we see it agrees with the non-inverted configuration, however can not predict the inverted profile. By Eqn. (3.8) the inverted profile would reverse the temperature gradient, thereby reversing the direction of the jump, which clearly can not happen. As suggested by Kjelstrup et al. [34] for irreversible thermodynamics to predict the inverted temperature profile, cross-over terms are required.

We conclude that irreversible thermodynamics can be used to our model steady state evaporation and condensation, with the appropriate phenomenological coefficient choices. Although cross-over terms do not appear to be necessary, if the parallel surface inverted temperature profile is a real physical possibility, then they must be included in the irreversible thermodynamics phenomenological expressions.

13.2 Statistical Rate Theory

The statistical rate theory exponential (3.13), and linearized (3.15) mass flux results are identical, and match well with the measured data [4] and irreversible thermodynamics predictions.

The SRT mass flux (3.13) is an exponential expression of the IT phenomenological mass flux (3.7). In fact, the linearized SRT expression (3.15) can be written in the same form as the IT mass flux, Eqn. (3.16). This, and the fact that the SRT and IT expressions yield the same results, leads us to conclude that the exponential SRT expression (3.13) is not necessary.

The factor k_s in front of the SRT expressions (3.13) (3.15) is the kinetic theory HK mass flux (4.8). This implies the assumption of unity condensation and evaporation coefficients, implying that all molecules hitting the surface, will condense, while all those which leave the surface are evaporating. In light of the MD simulation results [44] this assumption seems in doubt.

SRT does not provide an energy flux expression. In our SRT models we substituted with the IT conductive energy flux (3.8). Since the vapor interface temperature, and temperature jump are highly dependant on the energy flux expression, this caused the SRT vapor interface temperature, and temperature jump predictions to exactly follow those of irreversible thermodynamics, and thus agree well the measurements. From this it is clear that SRT does not predict the temperature jump, as Ward and Stanga [4] suggest.

As with the IT model, we found $T_l \approx T_{sat}(p_v)$ for the SRT simulations. Also of note, the entropy production for the SRT, IT combined model is positive.

We conclude that SRT accurately predicts steady state condensation and evaporation fluxes, and agrees with the measured temperature jumps, but does not predict them. An SRT energy flux expression is necessary to complete the SRT theory. However linear laws are sufficient to describe the mass and energy fluxes, suggesting that the SRT exponential analysis may not be necessary.

13.3 Hertz-Knudsen, and Chapman-Enskog

In our kinetic theory analysis the water is approximated as a monatomic vapor. Although this is not true for water molecules, we find that our kinetic theory models yield reasonable results relative to measurements, and the other models.

Two different mass and energy flux pairs were considered, the Hertz-Knudsen (4.22) (4.44), developed with equilibrium Maxwellian distributions, and the Chapman-Enskog (4.25) (4.49), based on the quasi-equilibrium CE vapor distribution. In all cases, both sets of expressions yielded identical results, leading us to conclude that the HK and CE models are very close for slow evaporation and condensation.

The predicted mass and energy fluxes match well with the other models, and the experimental mass flux [4].

The HK and CE models show $T_l \approx T_{sat}\left(p_v\right)$ as we observed with irreversible thermodynamics, SRT, and the Ward and Stanga measurements [4]. However the predicted vapor interface temperatures do not coincide with those of the other models and experimental values. Instead the HK and CE models predict small temperature jumps, which at times are in the opposite direction. Adjustment of the condensation, evaporation, or accommodation coefficients does not correct the jump.

The condensation and evaporation coefficients must be equal in equilibrium, and thus, if they are considered as constants, they must also be equal outside of equilibrium.

Although these models were not derived to ensure positive entropy production, as was the IT model, we find that the entropy production is always positive.

We conclude the HK and CE expressions accurately model our steady state evaporation and condensation, but they cannot predict the vapor interface temperature, and temperature jump.

13.4 Hertz-Knudsen and Chapman-Enskog with the Velocity and Temperature Dependant Condensation Coefficient

We introduced the velocity dependent condensation coefficient (4.51) into the kinetic theory expressions assuming equal condensation and evaporation coefficients. Again, we have two sets of mass and energy flux equations, one set based on a Maxwellian vapor distribution HKVEL (4.60) (4.67), and the other with a CE distribution CEVEL (4.71) (4.74) (4.75). Once again we observe that the two models yield nearly identical results.

The HKVEL (4.60) (4.67) and CEVEL (4.75) flux expressions are written in terms of temperature dependant coefficients, $\eta\left(T,T_l\right)$, and $\varphi\left(T,T_l\right)$. The coefficient for the mass flux (4.59) is different from that of the energy flux (4.66).

The velocity dependent condensation coefficient (4.51) is dependant on two parameters, ψ the measure of how many molecules condense, and ω which gives the dependence of the condensation coefficient on the molecular velocity, and liquid interface temperature. We found for $\psi \approx 5\times10^{-2}$, and $\omega = 1$ with purely specular reflection (accommodation coefficient $\gamma = 1$) that the HKVEL and CEVEL models predict a vapor interface temperature close to the measured values [4], and that of the SRT and IT models. This implies that approximately 5% of molecules hitting the interface condense, and their probability of condensing is highly dependant on the molecular velocity and interface temperature. We remark that these findings are contrary to the findings of Tsuruta et al. [44]. They report from MD simulations for Argon that $0.971 \leq \psi \leq 0.685$, $0.086 \leq \omega \leq 0.554$, and that most molecules reflect diffusely. We see from Figure 6.22 that in our models the Tsuruta parameters do not come near the measured vapor interface temperatures [4].

We also observe that the HKVEL and CEVEL models predict the same temperature jump directions as the IT conductive energy flux (3.8). This suggests the HKVEL and CEVEL model vapor interface temperature is dependant on the direction of the vapor temperature gradient as is for the IT and SRT models.

The HKVEL and CEVEL model interface temperature, and jump results must be considered as tentative, since we observed significantly different interface temperature results when the water

vapor specific heat was used in place of the monatomic molecule specific heat. We suggest the limitation of the HKVEL, and CEVEL models to monatomic molecules with only translational degrees of freedom is one possible explanation. Further research in this area is necessary to implement additional degrees of freedom into the HKVEL and CEVEL models, which will likely change their form.

The HKVEL, and CEVEL models with $\psi \approx 5 \times 10^{-2}$, $\omega = 1$, and $\gamma = 1$ predict mass and energy fluxes near the values of the Ward and Stanga experiments [4] and the other models. They also predict the $T_l \approx T_{sat}(p_v)$, except for evaporation they predict a higher liquid interface temperature. We suggest this could imply that the molecules leaving the interface could be at a higher temperature than the surface temperature.

We observe that the HKVEL and CEVEL models both have positive entropy production.

We then say that, when the monatomic specific heat is used, the HKVEL and CEVEL models accurately model our steady state evaporation and condensation, and show that kinetic theory can predict the same vapor interface temperature, and temperature jump direction as that observed by Ward and Stanga [4], which is not achieved by the simpler HK and CE models. Only the use of the more complicated velocity and temperature dependant condensation coefficient allows us to obtain these results. However accurate interface temperature results are not observed where the water vapor specific heat is employed, thus these results must not be considered as conclusive.

13.5 Steady State Evaporation and Condensation

We now mention common factors affecting condensation and evaporation from the models, and the experimental results [4].

Irreversible thermodynamics, SRT, and kinetic theory all predict similar mass and energy fluxes, This is a particularly interesting result, considering that each is derived from a different theory. This suggests that each can be used to predict evaporation and condensation fluxes.

In all our model simulations, and the experimental results, we see the liquid interface temperature is very close to the vapor pressure saturation temperature $T_l \approx T_{sat}(p_v)$.

Evaporation is forced by conductive heat flux flowing toward the interface, which implies that in the liquid $T_{bl} > T_{sat}(p_v)$, and in the vapor $T_{bv} > T_{sat}(p_v)$. Conversely, condensation is forced by conductive heat flux away from the interface, which is true for $T_{bl} < T_{sat}(p_v)$ in the liquid, and $T_{bv} < T_{sat}(p_v)$ in the vapor. The conductive heat flux in the liquid plays a much more significant role in delivering, or removing energy at the interface since the liquid thermal conductivity is an order of magnitude higher than that of the vapor. This causes the direction of the mass flux to be highly dependent on the direction of forcing in the liquid, if $T_{bl} > T_{sat}(p_v)$ there is a net evaporation, and if $T_{bl} < T_{sat}(p_v)$ there is condensation, regardless of the direction of the vapor temperature gradient.

The direction of the interface temperature jump seems to be dependant on the direction of the conductive heat flux in the vapor, and not the net mass flux direction (evaporation or condensation), $T_v > T_l$ for vapor conductive heat flux toward the interface , and $T_v < T_l$ for vapor conductive heat flux away from the interface. Since the direction of the vapor conductive heat flux does not establish if there is a net evaporation or condensation, then it can be in either direction for condensation or evaporation. Ward, Fang, and Stanga [2], [3], [4] from their experiments say that for condensation and evaporation $T_v > T_l$, however in all their evaporation and condensation experiments the conductive heat flux is toward the interface, forcing $T_v > T_l$ to be true. This hypothesis also agrees with the non-inverted parallel surface temperature jump, but is not true for the inverted case. More experimental results are required if this is to be confirmed.

13.6 Recommendations and Future Work

More experiments are required to confirm our hypothesis that the interface temperature jump is dependant on the conductive heat flux in the vapor. As well MD simulations, modeled after the experimental apparatus would be useful to establish the velocity dependant condensation coefficient parameter values, and further investigate how molecules reflect.

The inclusion of additional degrees of freedom in the HKVEL and CEVEL models should be considered; this could make them valid for use with the water vapor specific heat, instead of only with the monatomic molecule specific heat. As well the simple kinetic theory HK and CE models could also be modified to include additional degrees of freedom.

The inclusion of cross-over terms in the IT mass and energy flux expressions should be investigated.

A SRT energy flux expression to complete the SRT model would allow us to fully evaluate the SRT theory.

Our study of planar and spherical geometry revealed a marked dependence of the mass and energy flux on the geometry of the apparatus. In order to fully validate the models, a 3-D CFD simulation of the experiments would be useful.

References

[1] R. W. Schrage. *A Theoretical Study of Interphase Mass Transfer*. Columbia University Press, New York (1953).

[2] G. Fang and C. A. Ward. 'Temperature measured close to the interface of an evaporating liquid.' *Physical Review E* **59**(1), 417–428 (1999).

[3] G. Fang and C. Ward. 'Examination of the statistical rate theory expression for liquid evaporation rates.' *Physical Review E* **59**(1), 441–453 (1999).

[4] C. Ward and D. Stanga. 'Interfacial conditions during evaporation or condensation of water.' *Physical Review E* **64**, 051509 (2001).

[5] C. Ward and G. Fang. 'Expression for predicting liquid evaporation flux: Statistical rate theory approach.' *Physical Review E* **59**(1), 429–440 (1999).

[6] S. Harris. *An Introduction to the Theory of the Boltzmann Equation*. Holt, Rinehart, and Winston, Inc., New York (1971).

[7] P. C. Riedi. *Thermal Physics An Introduction to Thermodynamics, Statistical Mechanics, and Kinetic Theory*. Oxford University Press, New York, second edition (1988).

[8] C. Cercignani. *Rarefied Gas Dynamics From Basic Concepts to Actual Calculations*. Cambridge University Press (2000).

[9] F. W. Sears and G. L. Salinger. *Thermodynamics, Kinetic Theory, and Statistical Thermodynamics*. Addison-Wesley Publishing Company Inc., Philippines, 3rd edition (1975).

[10] C. Cercignani. 'Strong evaporation of a polyatomic gas.' *Rarefied Gas Dynamics* **74**(1), 305–320 (1981).

[11] C. Cercignani, W. Fiszdon, and A. Frezzotti. 'The paradox of the inverted temperature profiles between an evaporating and a condensing surface.' *Physics of Fluids* **28**(11), 3237–3240 (1985).

[12] T. Soga. 'A kinetic theory analysis of evaporation and condensation of a diatomic gas.' *Physics of Fluids* **28**(5), 1280–1285 (1985).

[13] H. Hertz. 'Ueber die verdunstung der flussigkeiten, insbesondere des quecksilbers, im luftleeren raume.' *Annalen der Physik und Chemie* **17**, 177–200 (1882).

[14] M. Knudsen. 'Die maximale verdampfunggeschwindigkeit des quecksilbers.' *Annalen der Physik und Chemie* **47**, 697–708 (1915).

[15] I. Eames, N. Marr, and H. Sabir. 'The evaporation coefficient of water: A review.' *International Journal of Heat and Mass Transfer* **40**(12), 2963–2973 (1997).

[16] R. Marek and J. Straub. 'Analysis of the evaporation coefficient and the condensation coefficient of water.' *Int. J. Heat and Mass Transfer* **44**, 39–53 (2001).

[17] J. Barrett and C. Clement. 'Kinetic evaporation and condensation rates and their coefficients.' *Journal of Colloid and Interface Science* **150**(2), 352–364 (1992).

[18] T. Ytrehus. 'Theory and experiments on gas kinetics in evaporation.' *Rarefied Gas Dynamics* **51**(2), 1197–1212 (1977).

[19] D. Labuntsov. 'An analysis of intensive evaporation and condensation.' *High Temperature (English Translation)* **5**, 579–647 (1967).

[20] Y. Sone. *Kinetic Theory and Fluid Dynamics*. Birkhauser, Boston (2000).

[21] A. K. Rebrov. 'Nonequilibrium processes at evaporating and condensing surfaces.' *AIP Conference Proceedings* **585**(1), 557–564 (2001).

[22] R. Meland and T. Ytrehus. 'Evaporation and condensation kundsen layers for nonunity condensation coefficient.' *Physics of Fluids* **15**(5), 1348–1350 (2003).

[23] S. R. de Groot and P. Mazur. *Non-Equilibrium Thermodynamics*. Dover Publications, Inc., New York (1984).

[24] D. Bedeaux. 'Nonequilibrium thermodynamics and statistical physics of surfaces.' *Advances in Chemical Physics* **64**, 47–109 (1986).

[25] L. Onsager. 'Reciprocal relations in irreversible processes i.' *Physical Review* **37**, 405–426 (1931).

[26] L. Onsager. 'Reciprocal relations in irreversible processes II.' *Physical Review* **38**, 2265–2279 (1931).

[27] D. Bedeaux, L. J. F. Hermans, and T. Ytrehus. 'Slow evaporation and condensation.' *Physica A* **169**, 263–280 (1990).

[28] D. Bedeaux and S. Kjelstrup. 'Transfer coefficients for evaporation.' *Physica A* **270**, 413–426 (1999).

[29] C. Ward. 'Liquid-vapor phase change rates and interfacial entropy production.' *Journal of Non-Equilibrium Thermodynamics* **27**(3), 289–303 (2002).

[30] J. W. Cipolla, H. Lang, and S. K. Loyalka. 'Kinetic theory of condensation and evaporation II.' *The Journal of Chemical Physics* **61**(1), 69–77 (1974).

[31] Y. Sone and Y. Onishi. 'Kinetic theory of evaporation and condensation.' *Journal of the Physical Society of Japan* **35**, 1773–1776 (1973).

[32] Y. Sone and Y. Onishi. 'Kinetic theory of evaporation and condensation-hydrodynamic equation and slip boundary condition.' *Journal of Physical Society of Japan* **44**(6), 1981–1994 (1978).

[33] J. B. Young. 'The condensation and evaporation of liquid droplets in a pure vapour at arbitrary knudsen number.' *International Journal of Heat and Mass Transfer* **34**(7), 1649–1661 (1991).

[34] S. Kjelstrup, T. Tsuruta, and D. Bedeaux. 'The inverted temperature profile accross a Vapor/Liquid surface analyzed by molecular computer simulations.' *Journal of Colloid and Interface Science* **256**, 451–461 (2002).

[35] K. Wylie and R. S. Brodkey. 'Transport phenomena at the liquid-vapor interface of mercury using a radioactive tracer.' *Progress in Heat and Mass Transfer* **6**, 195–206 (1972).

[36] Y. P. Pao. 'Application of kinetic theory to the problem of evaporation and condensation.' *The Physics of Fluids* **14**(2), 306–312 (1971).

[37] Y. P. Pao. 'Temperature and density jumps in the kinetic theory of gases and vapors.' *The Physics of Fluids* **14**(7), 1340–1346 (1971).

[38] L. Koffman, M. Plesset, and L. Lees. 'Theory of evaporation and condensation.' *Physics of Fluids* **27**(4), 876–880 (1984).

[39] R. Meland and T. Ytrehus. 'Dependence of the inverted temperature gradient phenomenon on the condensation coefficient.' *Physics of Fluids* **16**(3), 836–838 (2004).

[40] P. N. Shankar and M. Deshpande. 'On the temperature distribution in liquid-vapor phase change between plane liquid surfaces.' *Physics of Fluids A* **2**(6), 1030–1038 (1990).

[41] R. Meland, A. Frezzotti, T. Ytrehus, and B. Hafskjold. 'Nonequilibrium molecular-dynamics simulation of net evaporation and net condensation, and evaluation of the gas-kinetic boundary condition at the interphase.' *Physics of Fluids* **16**(3), 223–243 (2004).

[42] K. Yasuoka and M. Matsumoto. 'Evaporation and condensation at a liquid surface i. argon.' *Journal of Chemical Physics* **101**(9), 7904–7911 (1994).

[43] M. Matsumoto. 'Molecular dynamics of fluid phase change.' *Fluid Phase Equilibria* **144**, 307–314 (1998).

[44] T. Tsuruta, H. Tanaka, and T. Masuoka. 'Condensation/evaporation coefficient and velocity distributions at liquid-vapor interface.' *International Journal of Heat and Mass Transfer* **42**, 4107–4116 (1999).

[45] R. Meland and T. Ytrehus. 'Boundary condition at a gas-liquid interphase.' *AIP Conference Proceedings* **585**(1), 583–587 (2001).

[46] T. Tsuruta and G. Nagayama. 'DSMC analysis of interface mass transfer in Evaporation/Condensation based molecular dynamics study.' *Thermal Science and Engineering* **10**(1), 9–15 (2002).

[47] G. Nagayama and T. Tsuruta. 'A general expression for the condensation coefficient based on transition state theory and molecular dynamics simulation.' *Journal of Chemical Physics* **118**(3), 1392–1399 (2003).

[48] A. Rosjorde, D. W. Fossmo, D. Bedeaux, S. Kjelstrup, and B. Hafskjold. 'Nonequilibrium molecular dynamics simulations of steady state heat and mass transport in condensation i. local equilibrium.' *Journal of colloid and Interface Science* **232**, 178–185 (2000).

[49] A. Rosjorde, S. Kjelstrup, D. Bedeaux, and B. Hafskjold. 'Nonequilibrium molecular dynamics simulations of steady-state heat and mass transport in condensation. II. transfer coefficients.' *Journal of Colloid and Interface Science* **240**, 355–364 (2001).

[50] A. Frezzotti, P. Grosfils, and S. Toxvaerd. 'Evidence of an inverted temperature gradient during evaporation condensation of a lennard-jones fluid.' *Physics of Fluids* **15**(10), 2837–2842 (2003).

[51] D. Bedeaux, E. Johannessen, and A. Rosjorde. 'The nonequilbrium van der waals square gradient model (i). the model and its numerical solution.' *Physica A* **330**, 329–353 (2003).

[52] E. Johannessen and D. Bedeaux. 'The nonequilbrium van der waals square gradient model (II). local equilibrium of the gibbs surface.' *Physica A* **330**, 354–372 (2003).

[53] E. Johannessen and D. Bedeaux. 'The nonequilbrium van der waals square gradient model (III). heat and mass transfer coefficients.' *Physica A* **336**, 252–270 (2004).

[54] D. Bedeaux, S. Kjelstrup, and J. M. Rubi. 'Nonequilibrium translational effects in evaporation and condensation.' *Journal of Chemical Physics* **119**(17), 9163–9170 (2003).

[55] B. Bird, W. E. Stewart, and E. N. Lightfoot. *Transport Phenomena*. Wiley, New York (1960).

[56] Y. A. Cengel and M. A. Boles. *Thermodynamics An Engineering Approach*. McGraw Hill, 4th edition (2002).

[57] W. Robert C and M. J. Astle, editors. *Handbook of Chemistry and Physics*. CRC Press Inc., West Palm Beach, Florida, 59th edition (1978).

[58] S. Wolfram. *The Mathematica Book*. Wolfram Media/Cambridge University Press, 4th edition (1999).

[59] C. Ward. 'Temperature profile data points.' (2001). Email Communication, October 2003.

[60] E. Tombari, C. Ferrari, and G. Salvetti. 'Heat capacity anomaly in a large sampe of supercooled water.' *Chemical Physics Letters* **300**, 749–751 (1999).

[61] O. Benchikh, D. Fournier, and A. Boccara. 'Photothermal measurement of the thermal conductivity of supercooled water.' *Journal Physique* **46**, 727–731 (1985).

[62] M. Kaufman. *Principles of Thermodynamics*. Marcel Dekker Inc., New York (2002).